X-Ray Absorption Spectroscopy of Fe Complexes on Surfaces: Electronic Interactions and Tailoring of the Magnetic Coupling

Im Fachbereich Physik
der Freien Universität Berlin
eingereichte Dissertation von

Matthias Bernien

Mai 2009

1st referee:	Prof. Dr. Wolfgang Kuch Freie Universität Berlin
2nd referee:	Prof. Dr. Martin Weinelt Max-Born-Institut
3rd referee:	Prof. Dr. Hans-Peter Steinrück Friedrich-Alexander-Universität Erlangen-Nürnberg
Submission of thesis:	29th of May 2009
Day of disputation:	28th of October 2009

ABSTRACT

Within this thesis, two classes of transition metal complexes are studied on surfaces. Firstly, monomolecular layers of Fe(II) spin-crossover (SCO) complexes, prepared by *in-situ* sublimation onto Au(111) substrates and by self-assembly on Au(111)/mica, are investigated by means of X-ray absorption spectroscopy (XAS). For a multilayer of $Fe(phen)_2(NCS)_2$ and phenanthroline molecules on Au(111), a partly reversible SCO transition is demonstrated. It is found that the transition is suppressed if the $Fe(phen)_2(NCS)_2$ molecules are in direct contact with the Au(111) surface, possibly due to a chemical reaction of their ligands with the gold substrate. The intact deposition of $Fe(bp)_2$ is demonstrated, being relatively unperturbed even when in direct contact with the Au(111) surface. The self-assembly of $Fe(bppmc)_2$, which results in a monomolecular layer with both linker groups bound to the gold surface, is demonstrated by S $2p$ X-ray photoelectron spectroscopy. In both cases a high-spin state of the Fe centers is observed, implying that the strength of the ligand field would need to be increased to realize an SCO transition of the molecules on the surface.

The second class of transition metal complexes are quasi-planar Fe and Co octaethylporphyrin (OEP) molecules. Their magnetic properties on non-magnetic and ferromagnetic (FM) surfaces are analyzed in the submonolayer regime by X-ray magnetic circular dichroism (XMCD). The angle-dependent electronic structure at the metal center of Fe and Co OEP molecules on non-magnetic Cu(100) and oxygen-covered O/Cu(100) substrates, is determined by means of XAS. Measurements of the magnetic properties are carried out in a magnetic field of $B = 5$ T at $T = 8$ K. For Fe OEP on O/Cu, a very strong magnetic anisotropy is found, owing to the interaction with the oxygen and resulting in a factor of five between the in- and out-of-plane XMCD signal. The magnetism of Co OEP on O/Cu(100)

is dominated by the contributions of the d_{z^2} orbital. This results in a characteristic angular dependence of the XMCD signal, due to the anisotropy of the spin-density.

By means of XMCD measurements it is shown that the magnetic moment of the Fe centers of Fe OEP molecules can be aligned at room temperature if they are deposited onto FM Ni and Co substrates. A simple theoretical model is utilized to determine the magnetic coupling energies from temperature-dependent measurements of the Fe and substrate magnetizations. A much stronger coupling is found for Fe OEP on Co than on Ni substrates. Tailoring of the magnetic coupling is achieved by placing atomic oxygen between the molecules and the FM Ni and Co substrates. For the first time, an antiferromagnetic coupling of Fe porphyrin molecules to FM substrates is realized here, as evidenced by the opposite sign of the Fe and substrate XMCD signals.

KURZFASSUNG

Im Rahmen dieser Arbeit werden zwei Klassen von Übergangsmetallkomplexen auf Oberflächen untersucht. Als erstes werden die Eigenschaften von Fe(II)-Spin-Crossover-Komplexen (Fe(II)-SCO-Komplexen), präpariert durch *in-situ* Sublimation und selbstorganisierte Abscheidung als molekulare Einzellagen auf Au(111)-Substraten, mit Hilfe von Röntgenabsorptionsspektroskopie (XAS) analysiert. Für eine Mehrfachlage aus $Fe(phen)_2(NCS)_2$ und Phenanthrolin-Molekülen auf Au(111) wird ein teilweise reversibler SCO-Übergang nachgewiesen. Sind die $Fe(phen)_2(NCS)_2$-Moleküle in direktem Kontakt mit der Au(111)-Oberfläche, ist der Übergang vermutlich auf Grund einer chemischen Reaktion ihrer Liganden mit dem Gold-Substrat unterdrückt. Es wird gezeigt, dass sich $Fe(bp)_2$-Moleküle intakt auf Au(111) aufdampfen lassen und weitgehend ungestört adsorbieren. Das selbstorganisierte Abscheiden von $Fe(bppmc)_2$, bei dem beide Linkergruppen an die Goldoberfläche gebunden sind, wird an Hand von S $2p$ Röntgen-Photoelektronenspektroskopie demonstriert. In beiden Fällen wird ein High-Spin-Zustand der Fe-Zentren beobachtet, was impliziert, dass die Stärke des Ligandenfeldes erhöht werden muss, um einen SCO-Übergang der Moleküle auf der Oberfläche realisieren zu können.

Die zweite Klasse von Übergangsmetallkomplexen ist durch quasiplanare Fe- und Co-Octaethylporphyrin-Moleküle (Co-OEP-Moleküle) gegeben. Ihre magnetischen Eigenschaften werden im Bereich unterhalb einer Einzellage auf nicht-magnetischen und ferromagnetischen (FM) Oberflächen mittels Röntgenzirkulardichroismus (XMCD) analysiert. Die winkelabhängige elektronische Struktur an den Metallzentren von Fe- und Co-OEP-Molekülen auf nicht-magnetischen Cu(100)- und sauerstoffbedeckten O/Cu(100)-Substraten wird mittels XAS bestimmt. Messungen der magnetischen Eigenschaften sind in einem magnetischen Feld von $B = 5$ T

bei $T = 8$ K ausgeführt worden. Für Fe-OEP auf O/Cu(100) wird auf Grund der Wechselwirkung mit dem Sauerstoff eine sehr starke magnetische Anisotropie beobachtet, die sich in einem Faktor fünf zwischen dem XMCD-Signal in der Ebene und senkrecht dazu niederschlägt. Der Magnetismus von Co-OEP auf O/Cu(100) wird durch die Beiträge des d_{z^2}-Orbitals dominiert. Dies führt zu einer charakteristischen Winkelabhängigkeit des XMCD-Signals auf Grund der Anisotropie der Spindichte.

Mit Hilfe von XMCD-Messungen wird gezeigt, dass sich eine Ausrichtung der magnetischen Momente der Fe-Zentren von Fe-OEP-Molekülen bei Raumtemperatur erreichen lässt, wenn diese auf FM Ni- und Co-Substraten abgeschieden werden. Die magnetischen Kopplungsenergien werden durch temperaturabhängige Messungen der Fe- und der Substratmagnetisierung unter Anwendung eines einfachen theoretischen Modells bestimmt. Es wird eine sehr viel stärkere magnetische Kopplung von Fe-OEP zu Co- als zu Ni-Substraten beobachtet. Ein Maßschneidern der magnetischen Kopplung wird durch Einbringen von atomarem Sauerstoff zwischen den Molekülen und den FM Ni- bzw. Co-Substraten erreicht. Erstmalig ist hier eine antiferromagnetische Kopplung zwischen Fe-Porphyrin-Molekülen und FM Substraten realisiert worden, was durch die entgegengesetzten Vorzeichen der Fe- und Substrat-XMCD-Signale nachgewiesen wird.

CONTENTS

INTRODUCTION

The demands of modern information technology have led in the last fifty years to a steady progress in miniaturization of functional units. As a result of heavy investments by the semiconductor industry in optical lithography processes, ever smaller structures have become feasible. A transistor produced in the actual 45 nm (feature size) process occupies a surface area of less than 0.1 μm^2. Similar efforts in the information storage media have attained striking bit densities in the current magnetic hard disk drives, so that today a bit is represented by the magnetization of only 10^7 atoms. Since the accuracy of a structure written by lithography depends ultimately on the wavelength of the light used in the patterning process, a great deal of work is currently invested in developing new optical elements and light sources to utilize light of the extreme ultraviolet range.

Instead of pushing down the structural size limits, it may be smarter to engineer functional units atom by atom in a bottom-up fabrication approach [1]. Handling individual atoms is clearly too costly for massive production, but a solution may be to take advantage of self-assembling properties particular of organic molecules. In this regard, chemists have synthesized countless varieties of molecules, carrying the needed flexibility to this approach. If such molecules were arranged on a surface in a controlled manner, the formation of complex functional units, based either on properties of individual molecules or on the interplay between molecules and surface, would be at hand. Additionally, the two-dimensional arrangement on the surface allows for addressing the individual units by their lateral position.

The mechanisms for a controlled assembly are typically provided by intermolecular and molecule–substrate interactions, resulting in the formation of highly ordered two-dimensional molecular structures (self-assembly), as well as the local ordering of molecules (molecular recogni-

tion). The most common forces range from the weaker hydrogen-bond formation and van-der-Waals interactions, to stronger ionic and covalent bonds. The utilization of molecules to functionalize surfaces provides the possibility to tune a variety of surface properties. Broadly speaking, one may think of four generic properties: chemical, involving the formation of bonds to environmental molecules, the redox behavior, and catalytic properties [2, 3]; geometric, using the conformation of molecules to modify wetting and sticking behavior [4]; electric, by the formation of surface dipoles and the modification of transport properties [5, 6]; and finally magnetic, by tuning the molecular spin state, the magnetic anisotropy, and the magnetic coupling [7, 8]. If bistable molecules are used, such surface properties may be switched by an external stimulus, for example, light, temperature, or electrical currents.

In this thesis, magnetic molecules have been investigated on surfaces. The complete system displays bidirectional interactions, so that the molecules modify the surface properties, while the magnetism of the molecules is affected by the underlying substrate. If the molecular magnetism can be tailored, these molecules may serve as nanoscale building blocks for future molecular spintronic devices, in which a spin-polarized current or a local magnetic field may be used to switch the spin of the molecule.

In recent years, a great deal of attention has been directed towards the study of metalorganic complexes on surfaces [9–11]. In these compounds, a metal ion is bonded to organic ligands *via* coordination bonds. In transition metal (TM) complexes, the central ion can adopt different oxidation states, which are used in biological processes of paramount importance such as oxygen transport in hemoglobin or light trapping in chlorophyll. The electronic and magnetic properties of the central ion are influenced significantly by the surrounding organic ligands. The $3d$ electrons are subject to a ligand field, which lifts up their energy degeneracy. Depending on the symmetry and strength of the ligand field, the $3d$ electrons arrange themselves so that high, intermediate, and low spin states can be observed.

Here we will focus on two different classes of Fe complexes on metallic surfaces. Firstly, spin-crossover (SCO) complexes are investigated. For these molecules, the ligand-field splitting energy of the electronic levels is in the same range as the electron–electron repulsion, resulting in a metastable arrangement of the $3d$ electrons. This makes the complexes sensitive to a

variety of tiny perturbations, such as thermal excitations, pressure, and interactions with solvents or adjacent molecules. If the sensitivity of SCO complexes could be exploited to functionalize surfaces, they may detect small changes in a supramolecular arrangement or modifications of surface properties, not accessible to a direct read-out. However, thin layers of SCO molecules on surfaces in the monolayer regime have rarely been investigated due to limitations dictated by the preparation method. *In-situ* deposition by sublimation of these complexes in UHV requires a high thermal stability of the molecules. *Ex-situ* deposition from solution *via* covalent linkage to the substrate by means of a sulfur-containing anchor group requires a chemical modification of the SCO complex that might suppress the occurrence of a spin transition.

The main questions addressed here are: How can these methods be exploited to prepare monolayers of a particular SCO complex on metallic surfaces? What effect has the interaction with the surface on the electronic properties of the metal center? Will the SCO transition be preserved when the molecule is deposited on the surface?

In contrast to SCO complexes, porphyrins are highly stable metalorganic compounds. Thin layers of porphyrin molecules can be readily prepared by *in-situ* sublimation in UHV. Porphyrins are quasi-planar complexes. The central ion is four-fold coordinated by the porphyrin macrocycle. Two coordination sites can be occupied by additional ligands. If porphyrins are deposited onto surfaces the central ion is directly influenced by the surface. This may result in a modification of the electronic properties of the ion, but it may also affect the magnetic properties.

In the last few years, many works studying porphyrin molecules on surfaces have been published [11], including metalation of porphyrins on the surface [12, 13], and reversible switching of the interaction between the central ion and the surface by coordination of NO towards the metal center [14]. However, the magnetic properties of porphyrins adsorbed on surfaces have rarely been investigated [15, 16], and this thesis devotes a major part to studying the nature of the magnetic coupling of Fe porphyrin molecules to transition-metal surfaces.

The detection of the properties of the central ion in adsorbed complexes with coverages in the submonolayer range is always challenging, since one monolayer of molecules corresponds to an effective transition-metal cov-

erage of about a thirtieth of a monolayer. For the study of these minute amounts of adsorbate, X-ray absorption spectroscopy is a pertinent technique, since it combines a high sensitivity with element specificity. Thus, the electronic properties of the constituents of a sample can be studied independently. Additionally, the use of X-ray magnetic circular dichroism offers the unique possibility to measure the spin and orbital magnetic moments for each element present in the system. Thus, if the molecules are adsorbed on a magnetic substrate, their magnetization can be followed independently of the much larger magnetization of the underlying substrate. The magnetic anisotropy and the anisotropy of the spin density at the metal center are, therefore, investigated by angle-dependent XMCD measurements. Furthermore, X-ray absorption measurements using linearly polarized light are carried out to determine orientation-dependent electronic properties of the 3*d* electrons of the central ion, in particular, the anisotropy of the charge density.

Submonolayers of Fe and Co octaethylporphyrin molecules are investigated on non-magnetic and ferromagnetic surfaces. X-ray absorption techniques are employed to tackle the following questions: Is it possible to adsorb porphyrin molecules onto metallic surfaces in a controlled manner? How are the electronic structure and the magnetic properties of the molecules influenced by the presence of the surface? Can one modify, for example, the oxidation state, the magnetic moment, or the magnetic anisotropy? Can the molecules be magnetically aligned by an interaction to FM substrates? Is it possible to tailor the strength or the orientation of such magnetic coupling?

1

CORE LEVEL SPECTROSCOPIES OF TRANSITION METAL COMPLEXES

This chapter starts describing the interactions of X rays with matter in general. I then introduce the fundamentals of X-ray absorption spectroscopy (XAS), especially at the K, and $L_{2,3}$ edges, relevant for the transition metal complexes investigated here. In the following X-ray magnetic circular dichroism (XMCD) is discussed in view of its angular dependence and the orbital projected contributions to it. Different detection methods of the X-ray absorption cross-section are presented, and an quantitative description of the total electron yield (TEY) detection method is given, serving as the basis for the normalization of the X-ray absorption (XA) spectra. In the following section, aspects of the electronic structure of transition metal complexes are illustrated by means of ligand field theory. Finally, a brief introduction to X-ray photoelectron spectroscopy (XPS) is given.

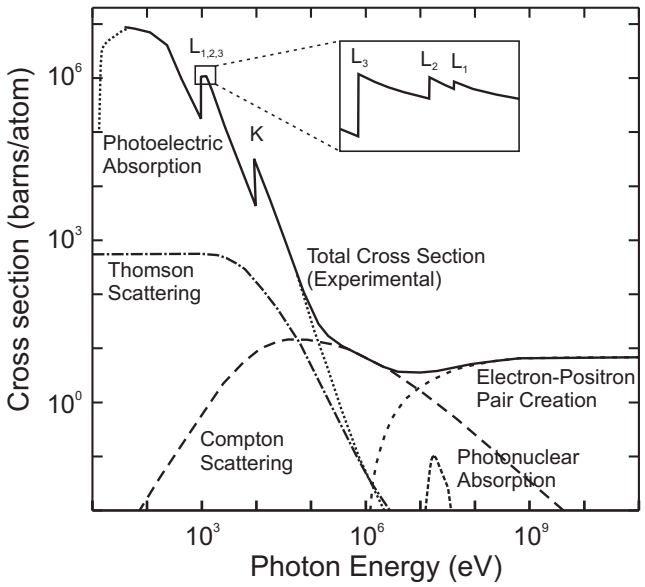

Figure 1.1: Cross section of photoabsorption in comparison to the one of elastic and inelastic scattering, as well as higher energy interactions of X rays with a Cu metal sample. Adapted from [17].

1.1 Interaction of X rays with Matter

If X rays traverse matter of thickness x, their intensity I is attenuated according to *Lambert-Beer's law*:

$$\mathrm{d}I = -\mu(E) I \mathrm{d}x \quad \Rightarrow \quad I = I_0 \mathrm{e}^{-\mu(E)x}. \tag{1.1}$$

The attenuation coefficient $\mu(E)$ composes additively *inter alia* of the contributions of elastic and inelastic scattering and of absorption. The cross section $\sigma_i(E) = \mu_i(E)/n$, with n the density of atoms, of the respective interactions is plotted in figure 1.1 against photon energy for a copper sample. In the soft X-ray regime up to 2 keV, relevant here, photoabsorption dominates over the other processes. The absorption spectrum is characterized by distinct absorption edges reflecting successive excitations of core electrons. These edges are denoted as $K \mathrel{\widehat{=}} 1s$, $L_1 \mathrel{\widehat{=}} 2s$, $L_2 \mathrel{\widehat{=}} 2p_{1/2}$, $L_3 \mathrel{\widehat{=}} 2p_{3/2}$, $M_1 \mathrel{\widehat{=}} 3s$, *etc.*

The absorption process can be understood within the scope of a simple one-electron picture. When absorbing a photon of energy $E = \hbar\omega$, a core electron is excited from an initial state $|i\rangle$ with energy E_i into a continuum of final states $|f\rangle$ with density $\rho(E_f)$ and energy $E_f = E_i + E$. The transition

rate $w_{i\to f}$ connects to the absorption cross section $\sigma(E)$ *via* the photon flux I_{ph}, according to:

$$\sigma(E) = \frac{\mu(E)}{n} = \frac{w_{i\to f}}{I_{ph}}, \tag{1.2}$$

and can be calculated with the help of *Fermi's golden rule*:

$$w_{i\to f} = \frac{2\pi}{\hbar}\left|\langle f|\mathcal{H}_{per}|i\rangle\right|^2 \rho(E_f)\,, \qquad \mathcal{H}_{per} = -\frac{e}{2mc}\vec{A}(\vec{r},t)\cdot\vec{p}$$

and the perturbation Hamiltonian $\mathcal{H}_{per}$ of an incoming electromagnetic plane wave of wave vector $\vec{k}$, polarization vector $\vec{\varepsilon}$, and vector potential

$$\vec{A}(\vec{r},t) = A_0\vec{\varepsilon}\mathrm{e}^{i(\vec{k}\cdot\vec{r}-\omega t)} \approx A_0\vec{\varepsilon}\mathrm{e}^{-i\omega t} + \ldots,$$

in dipole approximation:

$$w_{i\to f} = \frac{2\pi}{\hbar}|\langle f| - \frac{eA_0}{2mc}\mathrm{e}^{-i\omega t}\vec{\varepsilon}\cdot\vec{p}|i\rangle|^2\rho(E_f) = \frac{\pi e^2A_0^2}{2\hbar^3c^2}E^2|\langle f|\vec{\varepsilon}\cdot\vec{r}|i\rangle|^2\rho(E_f).$$

Thus, we obtain the absorption cross section using $I_{ph} = A_0^2\omega/(8\pi\hbar c)$ and equation 1.2:

$$\sigma(E) = \frac{4\pi^2e^2}{\hbar c}E|\vec{\varepsilon}\cdot\langle f|\vec{r}|i\rangle|^2\rho(E_f). \tag{1.3}$$

When the electron is excited above its ionization potential, the atom is ionized and the final state is represented by an outcoming electron (*photoelectric effect*). The energy distribution of the photoelectrons provides information about the occupied initial states. In an X-ray photoemission spectroscopy (XPS) experiment, this can be used to determine the composition of a sample as well as chemical properties of the elements, as will be discussed in section 1.8. If the photon energy is scanned over a certain range, the energy of the outcoming electron is varied. This electron is scattered by the neighboring atoms giving rise to broad resonances above the respective absorption edges if the scattered electronic wave interferes coherently at the position of the initial atom. The analysis of the extended X-ray absorption fine structure (EXAFS) is used to determine the local geometry in the vicinity of an element, *i.e.*, the distance of neighboring atoms. In contrast to diffraction-based techniques, EXAFS does not require an ordered crystal.

Below the ionization potential, an electron can be excited to unoccupied atomic states. By scanning the photon energy in a small region around

an absorption edge, the spectrum is a measure of the unoccupied density of states. These states are highly important because they constitute the valence shell of the atom, which mainly determines its properties. Such measurements are the fundament of near edge X-ray absorption fine structure (NEXAFS) spectroscopy. With the availability of X-ray optics in the soft X-ray regime, the $L_{2,3}$ edges of transition metals and the K edge of light elements found in organic systems became accessible. The spin-orbit splitting of the $2p$ core levels at the $L_{2,3}$ edges provides the possibility to carry out magnetic measurements by X-ray magnetic circular dichroism (XMCD) spectroscopy. Thus, X-ray absorption spectroscopy (XAS) in the soft X-ray regime is very well suited to study the properties of Fe and Co transition metal complexes investigated within the scope of this thesis.

1.2 Near Edge X-ray Absorption Fine Structure

NEXAFS spectroscopy[1] deals with the analysis of the strong resonances found in the vicinity of an absorption edge. In order to interpret the observed spectra, the expression for the absorption cross section, equation 1.3, has to be further evaluated. The calculation, boils down to the evaluation of the matrix element. It can be carried out in the basis set of atomic orbitals (AOs). This is of fundamental interest since each basis set can be expressed as a linear combination of the AO. In the one-electron picture, the initial state is given by a core AO and the final state by a valence orbital. Using AOs of the form:

$$|n, l, m_l, s, m_s\rangle = R_{n,l}(r) Y_{l,m_l} |s, m_s\rangle,$$

where n is the principal, l the angular, and s the spin quantum number, the matrix element factors into radial, spin, and angular parts:

$$\langle n', l', m'_l, s, m'_s | \vec{r} | n, l, m_l, s, m_s \rangle = \delta_{m'_s m_s} \langle n', l' | r | n, l \rangle \langle l', m'_l | \vec{r} | l, m_l \rangle. \quad (1.4)$$

For a given transition, s and m_s have to be preserved, since the dipole operator does not act on the spin. Tuning the photon energy to a certain absorption edge, n, l, n', and l' are fixed, and the radial part just determines the strength of the corresponding resonance. The radial component of the

[1] In the context of this thesis, I will refer to it with the more general term XAS since all absorption measurements are carried out in the vicinity of an absorption edge.

initial state $R_{n,l}(r)$ is localized at the core, thus only the density of states at the position of the element, selected by the photon energy, are probed. The full angular dependence is contained in the angular part, since the radial part is a scalar.

For dipole transitions into unoccupied final states, the absorption cross section is given according to equation 1.3:

$$\sigma(E) = GR\left|\vec{\varepsilon}\cdot\langle l', m_l'|\vec{r}|l, m_l\rangle\right|^2, \quad G = \frac{4\pi^2 e^2}{\hbar c}E, R = \left|\langle n', l'|r|n, l\rangle\right|^2. \quad (1.5)$$

Here, R denotes the squared radial part and G contains the photon energy and a constant. The intensity of a certain transition depends on the relative orientation of the transition matrix element and the polarization vector. This can be used in an angle-dependent measurement to identify the orientation of the atomic or molecular orbitals.

A close inspection of the transition matrix element reveals that nonzero values are only obtained if the dipole selection rules are fulfilled:

$$\Delta s = 0 \qquad \Delta m_s = 0 \qquad \Delta l = \pm 1 \qquad \Delta m_l = \begin{cases} +1 & \text{left circular} \\ 0 & \text{linear} \\ -1 & \text{right circular} \end{cases}$$

Thus, from an s initial state, only transitions into p orbitals can be excited. For a p initial state, d or s orbitals can be reached. At the $L_{2,3}$ edges ($2p_{1/2}$ and $2p_{3/2}$ initial states), the spin-orbit coupling is dominant and m_l and m_s are not good quantum numbers anymore. The dipole selection rules change as follows:

$$\Delta j = 0, \pm 1 \qquad \Delta s = 0 \qquad \Delta l = \pm 1 \qquad \Delta m_j = \begin{cases} +1 & \text{left circular} \\ 0 & \text{linear} \\ -1 & \text{right circular} \end{cases}$$

1.3 X-ray Natural Linear Dichroism

The polarization dependence of the X-ray absorption cross section can be exploited to determine the orientation of molecular bonds and orbitals. The intensity of a certain transition in angle-dependent XAS measurements depends on the relative orientation of the matrix element and the polarization vector of the X rays as follows from equation 1.5. The consequence can be easily understood within the one-electron model.

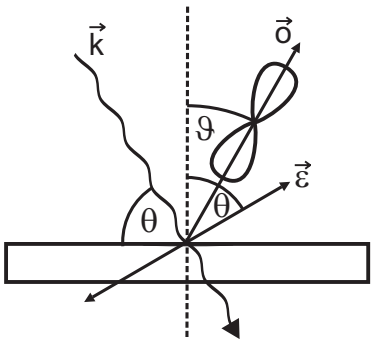

Figure 1.2: Unoccupied p orbital probed with linearly polarized X rays of wave vector $\vec{k}$. Illustrated are the definitions of the zenith angles of the polarization vector $\vec{\varepsilon}$ and the orbital vector $\vec{o}$.

1.3.1 Angular Dependence at the *K* Edge

Let us consider linearly polarized X rays exciting an s electron to an unoccupied p orbital, *e.g.*, from $1s$ to $2p$ at the K edge or from $2s$ to $3p$ at the L_1 edge. Since the charge distribution of an s orbital is isotropic, the angular dependence of the matrix element $\langle p_i|\vec{r}|s\rangle$, $i = x, y, z$ solely originates from the orientation of the p orbital excited to, resulting in a matrix element aligned along the symmetry axis of the respective p orbital. Due to the isotropic atomic initial state, this so-called search-light effect is also valid for molecular orbitals, where the final state is not necessarily of pure p character. Prominent examples are π^* and σ^* molecular orbitals. These orbitals are the antibonding generally unoccupied counterparts of the π and σ orbitals participating in a covalent bond. Single bonds possess one σ^* orbital along the interatomic axis. Double bonds display a σ^* and a perpendicular π^* orbital, while triple bonds exhibit a σ^* orbital and two π^* orbitals forming a plane perpendicular to the bond axis. The orientation of these orbitals and, thus, the direction of the bond can be determined from the angular dependence at the K edge.

Figure 1.2 represents an unoccupied p orbital probed with linearly polarized X rays. The intensity of the corresponding resonance is given by the dot product of the orbital vector $\vec{o}$, defined by the symmetry axis of the orbital, and the polarization vector $\vec{\varepsilon}$ of the X rays. If all molecules are adsorbed in the same way, but with random azimuthal orientations, the resulting resonance intensity for a given incidence angle $I(\theta)$ is obtained by integration over all azimuthal directions in spherical coordinates. The

zenith angles of the orbital ϑ and the polarization vector θ are defined in figure 1.2. The corresponding azimuth angles φ and ϕ are eliminated by the integration due to the assumed symmetry of the system:

$$\begin{aligned} I(\theta) &= \frac{1}{2\pi}\int_0^{2\pi}(\vec{o}\cdot\vec{\varepsilon})^2 \mathrm{d}\varphi = \frac{1}{2\pi}\int_0^{2\pi}\left(\begin{pmatrix}\sin\vartheta\cos\varphi\\ \sin\vartheta\sin\varphi\\ \cos\vartheta\end{pmatrix}\cdot\begin{pmatrix}\sin\theta\cos\phi\\ \sin\theta\sin\phi\\ \cos\theta\end{pmatrix}\right)^2 \mathrm{d}\varphi \\ &= \cos^2\theta\cos^2\vartheta + \frac{1}{2}\sin^2\theta\sin^2\vartheta. \end{aligned}$$

We can now determine the tilt angle ϑ of a molecular orbital, relative to the surface normal by measuring XAS at two different incidence angles. Maximum contrast would be obtained by measuring into two orthogonal directions, *e.g.*, $\theta_1 = 0°$ and $\theta_2 = 90°$. Since an incidence angle of $0°$ corresponds to a $\vec{k}$ vector parallel to the surface, θ_1 is chosen close to $0°$ (usually $20°$) due to technical limitations. The ratio of the corresponding resonance intensities is given by:

$$\begin{aligned} r(\theta_1, 90°) &= \frac{I(\theta_1)}{I(90°)} = \sin^2\theta_1 + 2\frac{\cos^2\theta_1}{\tan^2\vartheta} \\ \Rightarrow \quad \vartheta &= \arccos\sqrt{1 - \frac{2\cos^2\theta_1}{r(\theta_1, 90°) - 1 + 3\cos^2\theta_1}}\,. \end{aligned} \tag{1.6}$$

This offers a direct method to determine the orientation of a particular molecular orbital. However, it relies on the assumption that this orbital displays the same zenith angle ϑ for all molecules. With increasing disorder, the resonance intensity becomes independent of the incidence angle resulting in a ratio of $r(\theta_1, \theta_2) = 1$ and an apparent orientation of the orbital of $\vartheta = 54.7°$.

1.3.2 Angular Dependence at the $L_{2,3}$ Edges

At the $L_{2,3}$ edges, an electron is excited from a $2p$ initial state to an unoccupied $3d$ (or $4s$) orbital. This situation is more complex than at the K edge, since it involves three possible initial p orbitals with an anisotropic charge distribution and five final d orbitals.

In table 1.1 the oscillator strength $|\vec{\varepsilon}\cdot\langle d_i|\vec{r}|p_j\rangle|^2$ is evaluated for linearly polarized light with the polarization vector $\vec{\varepsilon}$ aligned into x, y, z directions.

	d_{z^2}	d_{xz}	d_{yz}	d_{xy}	$d_{x^2-y^2}$	
p_x	2	0	0	0	6	
p_y	0	0	0	6	0	$\vec{\varepsilon}\|\|\vec{x}$
p_z	0	6	0	0	0	
p_x	0	0	0	6	0	
p_y	2	0	0	0	6	$\vec{\varepsilon}\|\|\vec{y}$
p_z	0	0	6	0	0	
p_x	0	6	0	0	0	
p_y	0	0	6	0	0	$\vec{\varepsilon}\|\|\vec{z}$
p_z	8	0	0	0	0	

Table 1.1: Oscillator strengths (in relative units) for transitions between p and d orbitals in cubic symmetry and the polarization vector aligned along x, y, z Cartesian coordinates.

Note that for each Cartesian coordinate of $\vec{\varepsilon}$ and given d orbital, there is only one initial p orbital with nonzero oscillator strength. For each of the final d orbitals we have to sum over all p orbitals resulting in a specific vector that describes the sensitivity of the individual d orbital to a certain polarization direction (table 1.2). The intensity of the corresponding resonance can then be obtained by evaluating the dot product between this vector and $\vec{\varepsilon}$.

Here it should be mentioned that the assignment of observed resonances to unoccupied final orbitals cannot be done on a one-to-one basis as it would be suggested by the one-electron model. In fact, due to the interaction of the created core hole with the electrons of the d shell, one has to account for the multi-electronic nature of the initial and final state represented by $2p^6 3d^n$ and $2p^5 3d^{n+1}$, respectively. This leads to different energetic resonance positions depending on the arrangement of $3d$ and $2p$ electrons due to the Coulomb interaction. A rigorous treatment can only be done by calculating all possible transitions within the framework of multiplet-theory codes.

In contrast to the K edge, the angular dependence of XAS at the $L_{2,3}$ edges is not suitable to determine the orientation of an adsorbed molecule due to the higher number of possible transitions. However, once the ori-

d_{z^2}	d_{xz}	d_{yz}	d_{xy}	$d_{x^2-y^2}$
$\begin{pmatrix}2\\2\\8\end{pmatrix}$	$\begin{pmatrix}6\\0\\6\end{pmatrix}$	$\begin{pmatrix}0\\6\\6\end{pmatrix}$	$\begin{pmatrix}6\\6\\0\end{pmatrix}$	$\begin{pmatrix}6\\6\\0\end{pmatrix}$

Table 1.2: Oscillator strengths (in relative units) summed over all initial p orbitals with the polarization vector $\vec{\varepsilon}||x, y, z$.

entation of the adsorbate is known from the K-edge angular dependence, it can be a powerful tool to investigate the orbital occupation of a $3d$ transition metal center within a molecular complex. Even more, in combination with XMCD measurements the magnetic properties can be separated into the contributions of the individual $3d$ orbitals.

The presented formalism can be generalized in terms of an angle-independent contribution and the deviation given by the quadrupole moment $\mathcal{Q}$ of the charge distribution [18–20]. The absorption intensity for a transition to an unoccupied valence state $|\Phi^i_{l'}\rangle$ with angular momentum l' using linearly polarized X rays with the $\vec{E}$ vector along $\alpha = x, y, z$ coordinates is given by [20]:

$$I^i_\alpha = n^i_h GR \frac{l'}{3(2l'+1)} \left(1 - \frac{2l'+3}{2l'} \langle \Phi^i_{l'} | \mathcal{Q}_{\alpha\alpha} | \Phi^i_{l'} \rangle \right), \tag{1.7}$$

where n^i_h denotes the orbital-projected number of holes. The quadrupole moment operator is a symmetric tensor of second rank with vanishing trace. In space representation, using spherical coordinates, it is given by:

$$\begin{aligned}\mathcal{Q}_{\alpha\beta} =& \delta_{\alpha\beta} - \frac{3 r_\alpha r_\beta}{r^2} \\ =& \begin{pmatrix} 1-3\sin^2\theta\cos^2\phi & -3\sin^2\theta\sin\phi\cos\phi & -3\cos\theta\sin\theta\cos\phi \\ -3\sin^2\theta\sin\phi\cos\phi & 1-3\sin^2\theta\sin^2\phi & -3\cos\theta\sin\theta\sin\phi \\ -3\cos\theta\sin\theta\cos\phi & -3\cos\theta\sin\theta\sin\phi & 1-3\cos^2\theta \end{pmatrix}.\end{aligned}$$

1.4 X-ray Magnetic Circular Dichroism

XMCD utilizes the difference in absorption of left and right circularly polarized X rays caused by a magnetization of the unoccupied orbitals. The

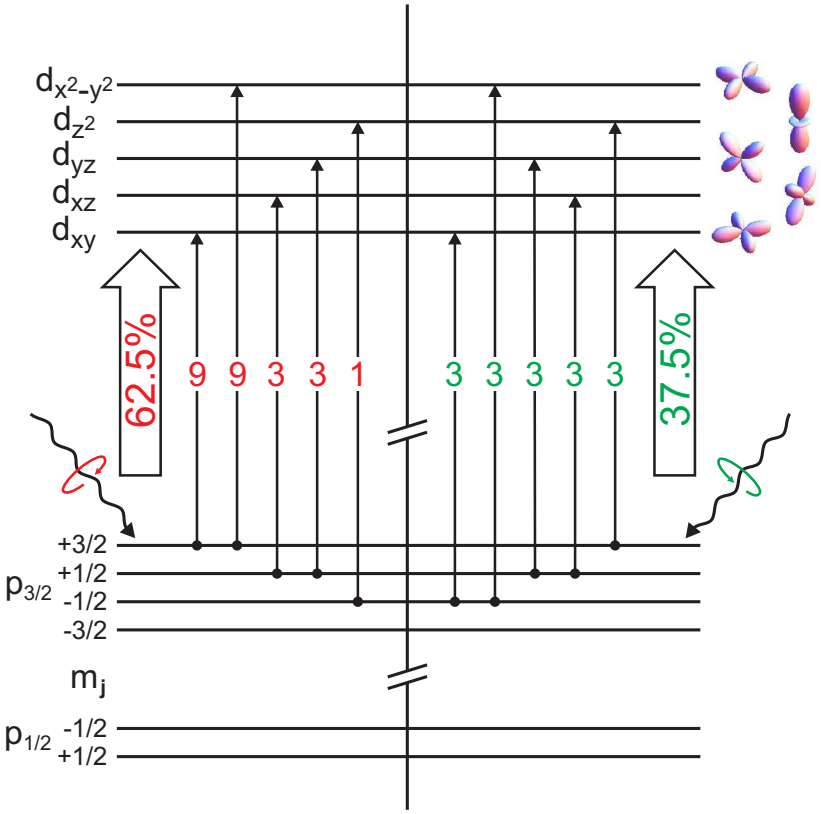

Figure 1.3: Intensities (in relative units) for transitions between spin-orbit and exchange-split initial $p_{3/2}$ states to ligand field-split final spin-up d orbitals when excited with left and right circularly polarized X rays.

beauty of XMCD lies in the existence of sum rules that link the integrated intensity of XAS and XMCD spectra to ground state properties of the valence states. This is the number of empty states, the spin moment, and the orbital moment. Unlike conventional magnetometry, XMCD combines the spectroscopic and the magnetic information, allowing for element-selective magnetization measurements.

XMCD was first predicted by Erskine and Stern in 1975 for the $M_{2,3}$ edges of Ni [21]. The first XMCD was measured at the Fe-K edge by Schütz *et al.* (1987) [22]. XMCD can be understood within the one-electron picture. For this thesis the $3d$ orbitals of Fe and Co transition metal ions, affected by the presence of a ligand field, are of main importance. Their final states are given by the $3d$ orbitals in cubic symmetry. The initial $2p$ orbitals are split into $2p_{1/2}$ and $2p_{3/2}$ subsets due to a strong spin-orbit coupling of 10

to 20 eV. The degeneracy of this subsets is lifted in the presence of an exchange interaction. These initial and final states can be expressed as a linear combination of AO, and the intensity of the individual transitions can be calculated by evaluating the angular part of the transition matrix element in equation 1.5. The resulting intensities are given in figure 1.3 for spin-up d orbitals ($m_s = \frac{1}{2}$), left and right circularly polarized X rays with $\vec{k}||\vec{z}$, and $\vec{z}$ being the quantization axis for both the spin and the ligand field. By summing the transitions for all singly occupied d orbitals, we obtain the integrated XMCD signal. Considering, for example, a high-spin $3d^5$ Fe^{3+} ion, here, all d orbitals are filled with one electron and, thus, contribute to the XMCD signal. For a $3d^5$ low-spin state, four electrons are paired, and only one orbital accounts for the XMCD signal, whereas five contribute to the XAS signal.

The transition can be envisaged as a two-step process. In a first step, a circularly polarized photon is absorbed, transferring its angular momentum to the excited electron. When excited from a spin-orbit split level, the momentum is carried as a spin and orbital polarization of the photoelectron. In a second step the photoelectron is inserted in the unoccupied final states, serving as a detector of spin and orbital polarization. The spin polarization at the L_3 and L_2 edge is of opposite sign, due to opposite spin-orbit coupling of the $2p$ initial states, $l + s$ and $l - s$, respectively. A spin polarization of the photoelectron only occurs for spin-orbit split initial states, *e.g.*, at the $L_{2,3}$ or $M_{2,3}$ edges. At the K edge, no such spin polarization is possible, since the initial state orbital momentum is zero ($1s \rightarrow 2p$). However, there still exists a dichroism effect if the final state exhibits an orbital polarization [23, 24].

1.4.1 Sum Rules

The sum rules connect the integrated intensity of the spectra to ground state properties of the system, thus building the fundaments for a quantitative analysis of XAS and XMCD data. The sum rules were derived by Thole and Carra *et al.* in 1992 and 1993 [25, 26]. The validity of the sum rules had been experimentally verified in 1995 by Chen *et al.* [27] by high-precision X-ray absorption experiments, detecting the total electron yield and the transmission of thin Fe and Co foils simultaneously.

In the context of this thesis, the d orbitals studied at the $L_{2,3}$ edges are of major importance. Under the influence of an ligand field, the valence states

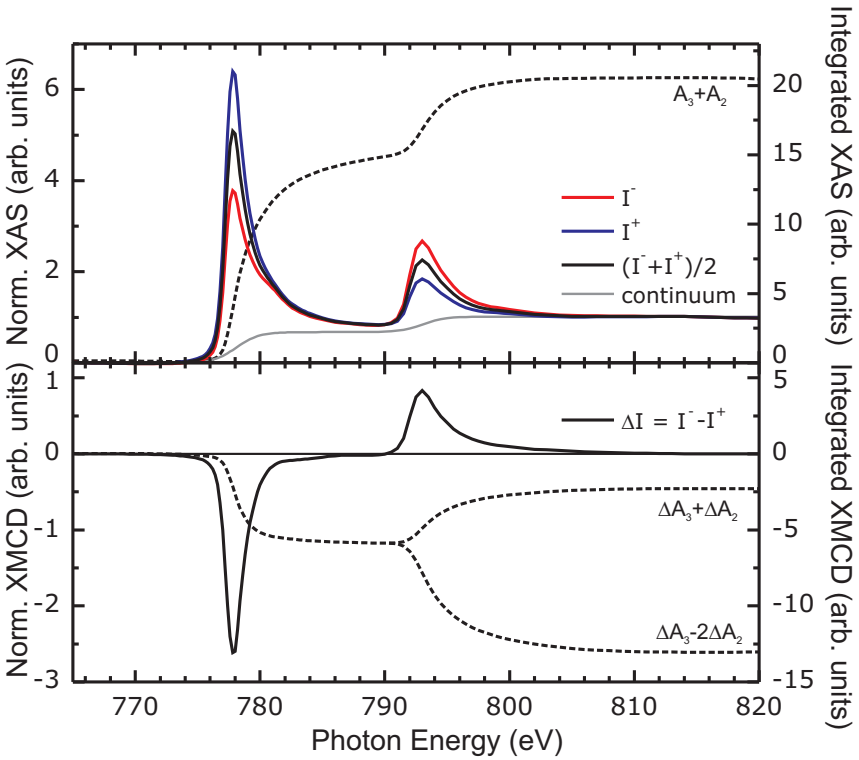

Figure 1.4: Upper panel: Co-$L_{2,3}$ XA spectra of 5 ML Co/Cu(100) taken with left and right circularly polarized X rays (red and blue). Additionally, the polarization-averaged spectrum (black) and its integrated intensity (dashed) after subtraction of the contributions of transitions into the continuum (gray) is shown. Lower panel: XMCD intensity difference (black) and corresponding integrated signals (dashed), see text.

split into symmetry-adapted orbitals. The ligand field around the central ion of porphyrins is basically of D_{4h} symmetry and the valence states can be expressed as the d orbitals in cubic symmetry with the quantization axis along the symmetry rotational axis of the ligand field. The sum over all $2p \rightarrow 3d$ transitions is connected to the number of $3d$ holes in the valence shell. Experimentally this quantity is determined by integrating the intensity over the L_3 and L_2 edges.

Figure 1.4 shows the XAS signal at the Co-$L_{2,3}$ edges for magnetically saturated 5 ML Co/Cu(100) taken with left and right circularly polarized X rays[2] I^- and I^+. The XMCD (lower panel) spectrum, given by the dif-

[2]XMCD depends on the relative alignment of the magnetization of the sample and the

ference of these two spectra $\Delta I = I^- - I^+$, contains the magnetic part of the signal. The nonmagnetic part is obtained by averaging the initial spectra, commonly referred to as white line. Contributions of transitions into the continuum of states above the ionization potential are separated by subtraction of an *ad hoc* step function I_{step} [27]. The function consists of two Fermi functions centered at the L_3 and L_2 edges with relative heights of 2 : 1, reflecting the occupation of the $p_{3/2}$ and $p_{1/2}$ levels. Contributions from $2p \rightarrow 4s$ transitions can be neglected since their intensity is smaller by a factor > 20 compared to the ones from $2p \rightarrow 3d$ transitions, mainly due to their smaller radial overlap [28].

The integrals over the L_3 and L_2 edges can be obtained from the XMCD spectrum and the white line after subtracting the step function:

$$\Delta A_i = \int_{L_i} \Delta I \mathrm{d}E, \quad A_i = \int_{L_i} \left((I^- + I^+)/2 - I_{\text{step}} \right) \mathrm{d}E, \quad i = 2, 3\,.$$

The charge sum rule relates the integrated intensity of the white line to the number of holes n_h in the valence shell. For the $L_{2,3}$ edges ($l' = 2$), it follows from equation 1.7 when summing over all d orbitals weighted with their respective orbital-projected number of holes n_h^i. Defining $\mathcal{Q}_\alpha^i = \langle d_i | \mathcal{Q}_{\alpha\alpha} | d_i \rangle$, $C = \frac{2}{15} GR$, and $n_h = \sum_i n_h^i$, it yields [19]:

$$[A_3 + A_2]_\alpha = C(n_h + n_Q^\alpha) = C \sum_i n_h^i \left(1 + \frac{7}{B} \mathcal{Q}_\alpha^i \right), \tag{1.8}$$

where $n_Q^\alpha = \frac{7}{4} \sum_i \mathcal{Q}_\alpha^i n_h^i$ is the anisotropy of the charge density. $\alpha = x, y, z$ denotes the direction of the electric field vector and the $\vec{k}$ vector when using linearly ($B = -4$) and circularly ($B = 2$) polarized X rays, respectively. Since $\mathcal{Q}_{\alpha\beta}$ has a vanishing trace, the anisotropic contribution cancels if an average over all three Cartesian coordinates is performed. In this case, the integrated intensity is directly proportional to the number of d holes. The same result can be obtained in a single measurement if the molecular complexes are oriented randomly, *e.g.*, in an polycrystalline sample. If the molecules are adsorbed on a surface and display random azimuthal orientations, such a spectrum can be obtained by measuring at a certain incidence angle. This so-called magic angle ensures that the signals along all Cartesian coordinates contribute equally to the resultant spectra. Note that the correspond-

photon angular momentum. Conventionally, I^- and I^+ are defined such that their difference is negative at the L_3 edge.

ing incidence angle θ between the $\vec{k}$ vector and the surface is different for linearly and circularly polarized X rays, being 54.7° and 35.3°, respectively.

The spin sum rule relates the integral over the $L_{2,3}$ edges of the XMCD intensity difference to the spin magnetic moment. Additionally, it contains the magnetic dipole operator T_α that expresses the anisotropy of the spin density. It couples the charge and spin density according to $T_\alpha = \sum_\alpha \mathcal{Q}_{\alpha\beta} S_\beta$. For transition metal complexes, the spin-orbit splitting of the $3d$ electrons is small ($\sim$ 50 meV) compared to a typical ligand-field splitting ($\sim$ 1 to 2 eV). As a consequence the spin density directly follows the charge density and T_α can be expressed as a product of the orbital-projected spin moment μ_S^i and the quadrupole moment of charge $\mu_D^\alpha = -\frac{7\mu_B}{\hbar}\langle T_\alpha \rangle = -\frac{\hbar}{2\mu_B}\sum_i \mathcal{Q}_\alpha^i \mu_S^i$ [19]. Assuming that the magnetization and the $\vec{k}$ vector are collinear, the spin sum rule is then given by:

$$[\Delta A_3 - 2\Delta A_2]_\alpha = -\frac{C}{\mu_B}(\mu_S + \mu_D^\alpha) = -\frac{C}{\mu_B}\sum_i \mu_S^i \left(1 + \frac{7}{2}\mathcal{Q}_\alpha^i\right). \tag{1.9}$$

The presence of μ_D^α can be understood considering that an anisotropic charge density also implies an anisotropic spin density. In turn, it vanishes for spherical charge distributions, *e.g.*, in spherical or cubic symmetry. This is the reason why it is usually neglected for metallic samples. Again, μ_S can be obtained by averaging over all Cartesian coordinates or measuring at the magic angle ($\theta = 35.3°$). This requires the sample to be magnetized in the same direction, generally only possible in strong magnetic fields and low temperature. It is important to realize that, although equations 1.8 and 1.9 both contain $\mathcal{Q}_\alpha^i$, their angle-dependent behavior is not the same, due to the difference in n_h^i and μ_S^i. For example, if an orbital d_i is fully empty it contributes intensity to the white line, but not to the XCMD since its two holes have opposite spin, due to the Pauli exclusion principle. In contrast to the charge sum rule, the integrals over the L_3 and L_2 enter as a difference, meaning that the intensity has to be well-separated. This is indeed the case for the later transition metals owing to the strong spin-orbit splitting of $2p$ core states. For the early transition metals, however, the condition is not fulfilled and this sum rule cannot be applied [29].

The orbital sum rule connects the integrated XMCD intensity with the orbital momentum along a given direction:

$$[\Delta A_3 + \Delta A_2]_\alpha = -\frac{3C}{2\mu_B}\mu_L^\alpha. \tag{1.10}$$

	d_{z^2}	d_{xz}	d_{yz}	d_{xy}	$d_{x^2-y^2}$
circular polarization	$\begin{pmatrix}5\\5\\2\end{pmatrix}$	$\begin{pmatrix}3\\6\\3\end{pmatrix}$	$\begin{pmatrix}6\\3\\3\end{pmatrix}$	$\begin{pmatrix}3\\3\\6\end{pmatrix}$	$\begin{pmatrix}3\\3\\6\end{pmatrix}$
circular dichroism	$\begin{pmatrix}8\\8\\-4\end{pmatrix}$	$\begin{pmatrix}0\\12\\0\end{pmatrix}$	$\begin{pmatrix}12\\0\\0\end{pmatrix}$	$\begin{pmatrix}0\\0\\12\end{pmatrix}$	$\begin{pmatrix}0\\0\\12\end{pmatrix}$

Table 1.3: Oscillator strengths (in relative units) of the individual d orbitals probed with circularly polarized X rays (left) with wave vector $\vec{k}||x, y, z$. For XMCD (right) magnetic saturation along the direction of the wave vector is required in addition.

Here, no additional angle-dependent term enters because the orbital momentum is anisotropic by definition. The measurement, again, requires that the sample is magnetically saturated along the measurement direction. The importance of μ_L^α stems from the fact that it is related to the magnetocrystalline anisotropy *via* the difference of the orbital moment along the easy and hard magnetization axes of a magnetic sample. Applying the orbital sum rule is demanding since the L_3 and L_2 edge are of opposite sign. Thus, the sum is small and the determination of μ_L^α becomes sensitive to tiny slopes or bendings in the measured spectra.

Evaluating the matrix element of the quadrupole moment of charge in the sum rules yields the intensities for the individual d orbitals to the XAS and XMCD signal. The final-orbital resolved intensities are depicted in table 1.3 [19]. For XMCD, the magnetization of the orbitals has to be aligned collinear with the $\vec{k}$ vector.

When using electron yield detection, the absorption cross section is not determined in absolute units, mainly because the conversion efficiency of X rays into secondary electrons enters as an unknown constant. Therefore, in order to apply the spin- and orbital-moment sum rules, they are usually normalized to the isotropic charge sum rule (based on a coordination averaged measurement as indicated by $\bar{\alpha}$). Furthermore, if the magnetization of the sample and the $\vec{k}$ vector of the incident X rays are not collinear (indicated by α and α'), only the projection of the moments onto $\vec{k}$ is measured. This is reflected in the formula by a factor $\cos\phi$. Finally, the degree of circular

polarization P_c enters as well. We obtain:

$$\mu_S + \mu_D^\alpha = -\frac{n_h \mu_B}{P_c \cos\phi} \frac{[\Delta A_3 - 2\Delta A_2]_{\alpha'}}{[A_3 + A_2]_{\bar{\alpha}}}, \tag{1.11}$$

$$\mu_L^\alpha = -\frac{2}{3} \frac{n_h \mu_B}{P_c \cos\phi} \frac{[\Delta A_3 + \Delta A_2]_{\alpha'}}{[A_3 + A_2]_{\bar{\alpha}}}. \tag{1.12}$$

Note that the number of d holes enters as an input parameter. If the sample is not magnetically saturated the spin and orbital moment, and the term describing the asymmetry of the spin density have to be replaced by the thermal expectation values of the corresponding operators: $\mu_S \rightarrow -2\langle S_\alpha \rangle \frac{\mu_B}{\hbar}$, $\mu_D^\alpha \rightarrow -7\langle T_\alpha \rangle \frac{\mu_B}{\hbar}$, $\mu_L^\alpha \rightarrow -\langle L_\alpha \rangle \frac{\mu_B}{\hbar}$.

The ratio of the orbital and spin moment can be derived by normalizing the orbital sum rule to the spin sum rule:

$$\frac{\mu_L^\alpha}{\mu_S + \mu_D^\alpha} = \frac{2}{3} \frac{[\Delta A_3 + \Delta A_2]_{\alpha'}}{[\Delta A_3 - 2\Delta A_2]_{\alpha'}}. \tag{1.13}$$

The ratio is obtained solely from the XMCD spectrum and without additional input parameters. Furthermore, it does not require magnetic saturation. μ_D^α cancels out for a measurement at the magic angle.

1.5 Detection of the Photoabsorption Cross Section

XAS and XMCD rely on the determination of the photoabsorption cross section in the range of an absorption edge. A direct approach to measure the absorption cross section experimentally can be realized in a transmission experiment, detecting the transmitted photons as a function of photon energy. Unlike gas-phase experiments, such a set-up is not easily realized when studying molecules adsorbed on surfaces, since it necessarily involves very thin substrates. In addition, the obtained signal is dominated by the contributions of the substrate. Alternatively, fluorescence photons or Auger electrons produced by the annihilation of the core hole can be used as a measure of the cross section. In figure 1.5 (a) the two decay processes are shown. An electron is excited from a core level to an unoccupied state. The created core hole is filled with an electron, and the energy is used to extract an electron

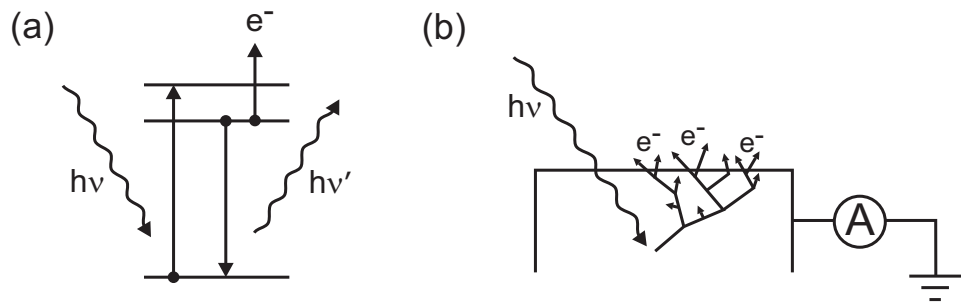

Figure 1.5: (a) Photoabsorption of an electron and decay of the core hole by fluorescence or Auger effect. (b) Cascade of low-energy electrons generated by an Auger electron, and detection of the resulting current.

in an Auger process or to emit a fluorescence photon. In (b) the generation of secondary electrons by an initial Auger electron is depicted. The photons impinging the surface penetrate into to sample and are thereby attenuated according to their mean free path. The generated electrons are scattered in the sample and excite additional electrons. Only electrons that have sufficient energy to overcome the surface potential barrier can contribute to the measured signal, given by the detection of the extracted electrons or the drain current of the sample.

The detection of electrons has the advantage of a high surface sensitivity, since the mean free path of electrons is much smaller than that of X rays. In addition, the Auger decay dominates over fluorescence at the K edge of N and C and at the $L_{2,3}$ edges of transition metals by more than two orders of magnitude [30]. The produced Auger electrons undergo inelastic scattering processes in the solid, generating an avalanche of low-energy electrons. The Auger electrons of a certain transition can be discriminated from other electrons using an energy filter with pass energy centered around the Auger transition. This detection method is called Auger electron yield (AEY). Since it is strongly transition-selective, it ensures a high signal-to-background ratio. A problem occurs if photoelectron peaks enter or leave the energy window when the photon energy is varied. A photoelectron peak that stays inside the energy window only increases the contribution of the background. In partial electron yield (PEY), all electrons above a certain threshold are detected. In that way, also Auger electrons that suffered an energy loss due to inelastic scattering contribute to the signal, while low-energy electrons are filtered out. This results in a higher signal but also decreases the signal-to-

background ratio. Such measurements can be carried out by simply using a retarding grid in front of an electron multiplier allowing for a high acceptance angle of the detector. A third possibility, referred to as total electron yield (TEY), is to detect all electrons that leave the sample. Since no energy filtering is involved, this can be realized by simply measuring the drain current of a sample. TEY yields the highest signal but also the lowest signal-to-background ratio of the described electron-detecting methods. However, the simple setup makes it less sensitive to variations in measurement geometry, providing the stability and reproducibility which is advantageous for normalization of the recorded spectra. Furthermore, it is the only of the above described electron-detecting techniques that allows for measurements in an applied magnetic field.

The XAS measurements presented in this thesis were acquired by TEY. Considering a sample with a depth-dependent absorption coefficient $\mu(x)$, the contribution of electrons generated in a depth x to the TEY signal is given by [31]:

$$\mathrm{d}Y_e = n_e N_{ph}(x)\mu(x)\mathrm{e}^{-\int_0^x 1/\lambda_e(x')\mathrm{d}x'}\mathrm{d}x\,, \qquad N_{ph}(x) = N_{ph}^0\mathrm{e}^{-\int_0^x \mu(x')\mathrm{d}x'}\,,$$

where $\lambda_e(x)$ is the effective electron escape depth, $N_{ph}(x)$ the number of photons attenuated by the overlying layers and n_e is the average number of electrons produced by one absorption event, *i.e.*, the electron gain factor. The TEY signal is calculated by integrating over the sample thickness:

$$Y_e = n_e N_{ph}^0 \int_0^\infty \mathrm{e}^{-\int_0^x (\mu(x')+1/\lambda_e(x'))\mathrm{d}x'}\mu(x)\mathrm{d}x. \tag{1.14}$$

1.6 Normalization of Spectra

The main goal of the normalization is to separate the photoabsorption cross section of an adsorbate from undesired energy- or time-dependent components in the measured signal. These are contributions of the substrate, the transmission function of the beamline and instabilities of the X-ray beam. In order to choose a proper normalization scheme, a detailed picture has to be developed of how these contributions enter into the measured signal.

Given a homogeneous sample with absorption coefficient μ_C, the integral in equation 1.14 evaluates to:

$$Y_e = n_e N_{ph}^0 \frac{\mu_C}{1/\lambda_e + \mu_C}.$$

Typically the mean free path of soft X rays $1/\mu_C$ is longer by two orders of magnitude than the one of electrons. In this case, we can approximate $\mu_C/(1/\lambda_e + \mu_C) \approx \lambda_e \mu_C$. However, for non-perpendicular X-ray incidence, μ_C has to be replaced by $\mu_C/\sin\theta$, with θ the angle between the surface and the $\vec{k}$ vector of the X rays. This leads to an effective decrease of the mean free path. For incidence angles very close to 0°, $\sin\theta/\mu_C \gg \lambda_e$ is no longer valid. The TEY signal saturates and it is not proportional to μ_C any longer [32].

If the sample consists of an adsorbate on a substrate of absorption coefficients μ_A and μ_C, and a material-independent electron mean free path and electron gain factor, integrating equation 1.14 leads to:

$$Y_e = n_e N_{ph}^0 \left(\left(1 - \mathrm{e}^{-(\frac{1}{\lambda_e}+\mu_A)\Delta x}\right) \frac{\mu_A}{1/\lambda_e + \mu_A} + \left(\mathrm{e}^{-(\frac{1}{\lambda_e}+\mu_A)\Delta x}\right) \frac{\mu_C}{1/\lambda_e + \mu_C} \right).$$

Where Δx is the thickness of the adsorbate layer. Note that as long as the signal does not saturate, measuring at grazing incidence angles increases the overall signal by $1/\sin\theta$ since $\mu_{A,C}$ is replaced by $\mu_{A,C}/\sin\theta$. The signal-to-background ratio is hardly influenced since the exponents in the damping factors are dominated by $1/\lambda_e$. The dependence of the signal-to-background ratio on Δx can be used as a measure of the thickness or the amount of an adsorbate. If $\sin\theta/\mu_A \gg \lambda_e$ is not fulfilled the damping factors also contribute to the saturation effects at higher thicknesses Δx of the adsorbate layer [32]. The spectra presented in this thesis were measured from adsorbates with coverages in the monolayer regime and at incidence angles bigger than 20°, consequently the importance of saturation effects is ruled out.

It is instructive to rewrite the last equation in order to stress the energy dependence of the different constituents for $1/\mu_{A,C} \gg \lambda_e$:

$$Y^{\mathrm{sample}}(E) = m_e E A_1 I(E)(k_1 \lambda_e \mu_A(E) + k_2 \lambda_e \mu_C(E)),$$
$$k_1 = 1 - \mathrm{e}^{-(1/\lambda_e+\mu_A)\Delta x},\ k_2 = \mathrm{e}^{-(1/\lambda_e+\mu_A)\Delta x}.$$

Here, A_1 is the illuminated area. The energy dependence of the photon flux density $I(E) = N_{ph}^0(E)/A_1$ mainly arises from the transmission function of

the beamline containing reflectivity changes of the X-ray optics and absorption of X rays due to contaminations of the beamline. The electron gain is basically proportional to the photon energy: $n_e = m_e E$ [33]. The energy dependence of λ_e and m_e can be neglected due to the small range the photon energy is scanned. The one of the exponents is suppressed because they are dominated by $1/\lambda_e$.

To separate $\mu_A(E)$ from the contributions of the photon flux density $I(E)$ and the substrate $\mu_C(E)$, the spectra of the "clean" substrate $Y^{\text{clean}}(E)$ is always measured before adsorbing the adsorbate:

$$Y^{\text{clean}}(E) = m_e E A_1 I(E) \lambda_e \mu_C(E)\,, \quad Y^{\text{grid}}(E) = m_e E A_2 I(E) \lambda_e \mu_G(E).$$

For both measurements the signal of a gold grid $Y^{\text{grid}}(E)$ is recorded in parallel. Dividing the signal of the sample and of the "clean" substrate by the respective signals of the grid yields:

$$Y^{\text{sample}}_{\text{grid}}(E) = \frac{A_1}{A_2}\left(k_1 \frac{\mu_A(E)}{\mu_G(E)} + k_2 \frac{\mu_C(E)}{\mu_G(E)}\right), \quad Y^{\text{clean}}_{\text{grid}}(E) = \frac{A_1}{A_2} \cdot \frac{\mu_C(E)}{\mu_G(E)}.$$

By this procedure the energy-dependent modulation by the photon flux density cancels out. Furthermore, time-dependent features in the signal due to instabilities of the X-ray beam are removed. This is only possible since the two signals are recorded simultaneously. The obtained signals can now be divided by each other:

$$\frac{Y^{\text{sample}}_{\text{grid}}(E)}{Y^{\text{clean}}_{\text{grid}}(E)} = k_1 \frac{\mu_A(E)}{\mu_C(E)} + k_2 \quad \Rightarrow \quad Y_{A/C}(E) = \frac{k_1}{k_2} \cdot \frac{\mu_A(E)}{\mu_C(E)} + 1.$$

Evaluating this expression in the pre-edge region E_0 of the adsorbate, *i.e.*, $\mu_A(E_0) = 0$, provides the damping constant of the substrate k_2. Dividing by the latter yields $Y_{A/C}(E)$, such that $Y_{A/C}(E_0) = 1$.

Alternatively the signal can be normalized by subtracting the signal of the "clean" substrate. Here the damping of the substrate signal in the sample has to be compensated by multiplying by the already obtained damping constant k_2, *i.e.*, scaling the two spectra to fit in the pre-edge region:

$$Y_{A/G}(E) = Y^{\text{sample}}_{\text{grid}}(E) - k_2 Y^{\text{clean}}_{\text{grid}}(E) = k_1 \frac{A_1}{A_2} \cdot \frac{\mu_A(E)}{\mu_G(E)}.$$

Finally, μ_C and μ_G can be approximated by linear functions if they are smoothly varying in the range the photon energy is scanned. Then multiplying[3] with these functions provides a signal proportional to the absorption coefficient. For the spectra presented in this thesis both normalization procedures are applied as a crosscheck. In addition the scaling contains useful information when comparing the signals of different samples. $Y_{A/C}(E)$ is a measure of the adsorbate signal relative to that of the substrate, and is geometry independent. $Y_{A/G}(E)$ is especially valuable when comparing adsorbates on different substrates.

There are, however, various difficulties that might complicate the normalization procedure. First of all, the X rays provided by the beamline are not purely monochromatic. For example, the second order of the monochromator produces a component with double the energy. In this case, the signals of the sample, of the "clean" substrate, and of the grid $Y(E)$, have to be replaced by $Y(E) + k_3 Y(2E)$. The ratio k_3 of the second to the first order component depends on the energy range and the settings of the monochromator, and is normally of the order of 5%. This modifies the normalized signals according to:

$$Y'_{A/C}(E) = \frac{k_1}{k_2} \cdot \frac{\mu_A(E)}{\mu_C(E) + k_3 \frac{I(2E)}{I(E)} \mu_C(2E)} + 1\,,$$

$$Y'_{A/G}(E) = k_1 \frac{A_1}{A_2} \cdot \frac{\mu_A(E)}{\mu_G(E) + k_3 \frac{I(2E)}{I(E)} \mu_G(2E)}\,.$$

For small amounts of adsorbate, $\mu_A(2E) = 0$ can be assumed. There may, however, be two complications. On the one hand, $\mu_{C,G}(2E)$ might not be smoothly varying with energy, which could become severe if a resonance of the substrate falls in the energy range of $2E$. In this situation, the value of k_3 was reduced by operating the monochromator at constant fixed focus (cff) values of 1.6 instead of 2.25. On the other hand, $I(E)$ might approach 0. This is especially troublesome at the C-K edge, where the intensity drops by more than one order of magnitude, due to carbon contaminations of the beamline. However, since this effect is restricted to a very small energy range ($\sim$2 eV), it can be compensated by adding a constant to $Y^{\mathrm{grid}}(E)$. This constant can now be adjusted such that the artifact vanishes.

[3]For $Y_{A/C}(E)$, unity has to be subtracted before multiplying. In order to distinguish the two ways of normalization, it is added afterwards again.

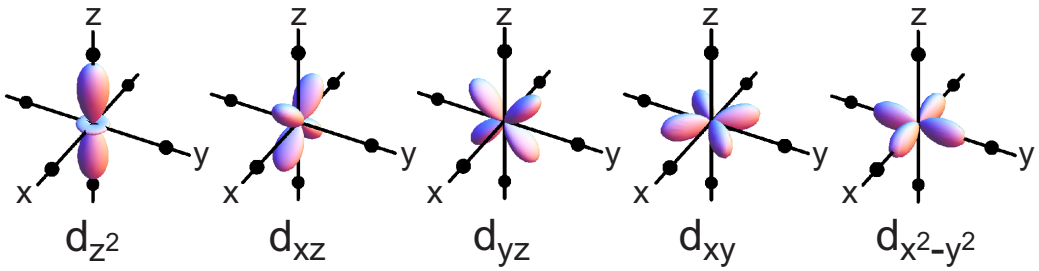

Figure 1.6: *d* orbitals in cubic symmetry. Indicated are, in addition, the positions of an octahedral arrangement of point charges.

For most of the spectra presented in this thesis the adsorbate signal is normalized to the substrate signal ($Y_{A/C}$), indicated by "XAS (arb. units)" on the y axis. This signal is independent of the ratio of the illuminated areas on the sample and on the grid (A_1/A_2) and, thus, provides with the possibility to compare the signals of adsorbates on the same substrates. If the signals of adsorbates on different substrates are presented in one graph the adsorbate signals is normalized relative to each other by normalizing to their edge jump, *i.e.,* the post-edge region, after subtracting unity from $Y_{A/C}$. Such a normalization is indicated by "Norm. XAS (arb. units)" on the y axis. However, for small adsorbate signals, the edge jump cannot always be determined reliably due to small bendings of the spectra. In that case, the spectra are scaled consistently to each other. The normalization of the XAS spectra was carried out with Mathematica[4] routines programmed in the framework of the thesis. For the XMCD spectra, pairs of spectra for left and right circularly polarized X rays were always treated in the same way to prevent artifacts in the difference spectra.

1.7 Ligand Field Theory

The multitude of electronic configurations, which the 3*d* electrons of the central ion of a transition metal complex can adopt, is a result of its electronic interaction with the organic ligands. Simply put, the effect of the ligands can be regarded as an electrostatic field at the metal site. In this model the ligands are represented by point charges, arranged around the metal center, thereby displaying a characteristic symmetry. The model is referred to as crystal field theory (CFT). Although it neglects the geometry of

[4] © Wolfram Research

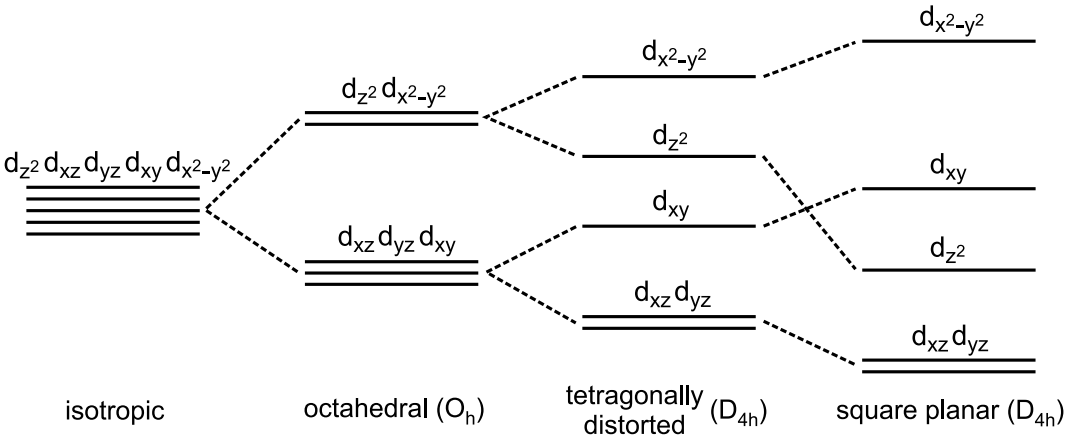

Figure 1.7: Splitting of d orbitals under the influence of octahedral, symmetric tetragonal-distorted, and square-planar arranged point-charges. In brackets the corresponding point-symmetry groups are given.

the molecular orbitals (MOs) of the ligands and their hybridization with the atomic orbitals (AOs) of the metal center, many of the physical effects can be readily explained within this model.

In figure 1.6 the d orbitals in cubic symmetry are shown. An octahedral crystal field is given by six point charges equidistantly placed on the three Cartesian axes. Due to their distinct charge distribution, the individual d orbitals are differently affected by the electrostatic interaction with the ligands. If we assume negative point charges, the orbitals that display charge density on the Cartesian axes are more strongly repelled than the others. For the given symmetry, the orbitals group into two degenerate subsets referred to as e_g (d_{z^2}, $d_{x^2\text{-}y^2}$) and t_{2g} (d_{xz}, d_{yz}, and d_{xy}). It is worth mentioning that each of the subsets displays an isotropic charge distribution. For historical reasons, the energetic splitting between the two subsets is referred to as $10Dq$. The energy levels for this situation are depicted in figure 1.7. When introducing a tetragonal distortion by weakening the ligands on the z axis or increasing their distance to the center, the d_{z^2}, d_{xz}, and d_{yz} orbitals are lowered in energy (tetragonally distorted)–even more so if these ligands are absent (square planar). The symmetry point group for the latter two cases is D_{4h}. In this symmetry, d_{xz} and d_{yz} are the only degenerate orbitals, forming an orbital denoted as d_π. The symmetry of the ligand field for the SCO complexes, discussed in chapter 3, can be approximated by an octahedral symmetry, whereas for the porphyrin molecules, presented in chapter 4, it

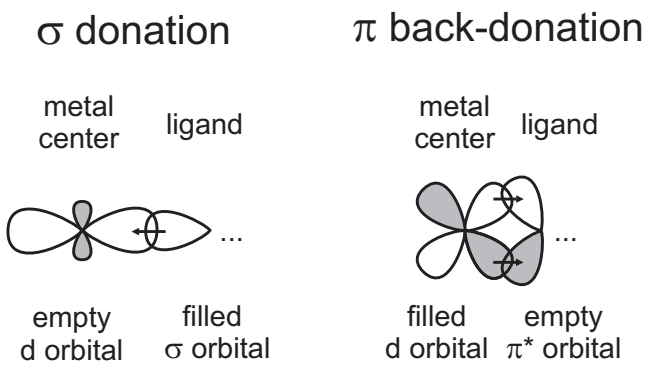

Figure 1.8: Metal–ligand charge transfer. Donation from a ligand σ orbital into an metal d orbital (left) and back donation from a metal d orbital into a ligand π^* orbital (right).

can be approximated by a square planar or tetragonally distorted symmetry.

In ligand field theory (LFT) each point charge is replaced by MOs. These MOs may covalently interact with the AOs of the metal center. The resulting energetic splittings can be calculated within the framework of density functional theory (DFT) calculations [34–37]. One important difference to CFT is the possibility for charge transfer between metal and ligand orbitals of the same symmetry. The two most prominent transfer processes are sketched in figure 1.8 [38–40]. In the first case charge is transfered from an occupied σ orbital at the ligand site to an unoccupied metal d orbital (σ donation). In the second case the charge transfer takes place from an occupied d orbital into an unoccupied ligand π^* orbital. These two processes may occur at the same time, and stabilize each other. It is important that the donation and back donation involves specific orbitals. For the charge transfer between the metal center and a porphyrin macrocyle, donation takes place into the $d_{x^2\text{-}y^2}$ orbital, whereas back donation involves the d_π (d_{xz}, d_{yz}) orbital. In the presence of axial ligands, donation into the d_{z^2} orbital may take place. The extent of charge transfer depends on the ratio of ionic and covalent character of the coordination bond [38, 41, 42].

1.8 X-ray Photoelectron Spectroscopy

Unlike XAS, X-ray photoelectron spectra are recorded at fixed photon energy, and the excited electrons are detected energy resolved by means of a hemispherical mirror analyzer (HMA). Besides the photoemission of core-

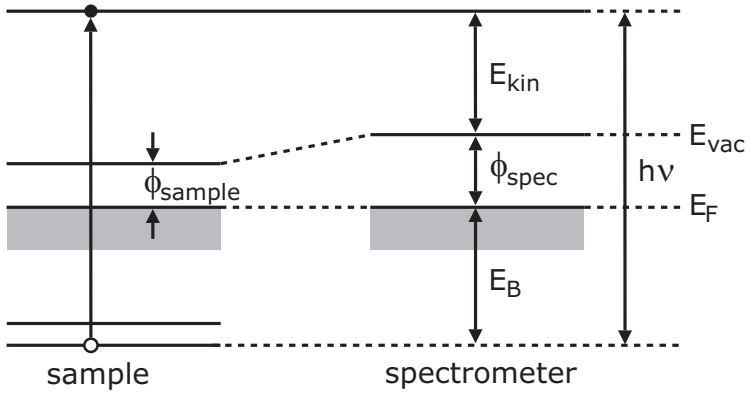

Figure 1.9: Scheme of the energy levels relevant for XPS. Indicated are the relative energetic positions of the Fermi levels E_F, the work functions ϕ, and the vacuum levels E_{vac} of sample and spectrometer, together with the kinetic energy E_{kin} and the binding energy E_B of the photoelectron, as well as the excitation energy $E_{\text{exc}} = h\nu$.

level electrons, the resulting spectra contain contributions from Auger electrons and low-energy secondary electrons, which can be separated by their energetic position. The final state for a photoemission process is given by an outcoming electron and a core hole at the excited ion. Besides energy conservation no selection rules have to be fulfilled (*cf.* equation 1.3). X-ray photoelectron spectroscopy (XPS), therefore, probes the occupied density of states of a sample, whereas XAS probes the unoccupied density of states. Since the binding energies of the core electrons are characteristic of each element, and their density of states is highly localized, XPS provides a means to determine the composition of a sample in a quantitative manner.

A scheme of the detection process is given in figure 1.9. Core electrons of the sample are excited by photons of excitation energy $E_{\text{exc}} = h\nu$. The electrons leave the sample and are detected by the spectrometer at their kinetic energies E_{kin}. Since the spectrometer and the sample are electrically connected, their Fermi levels E_F are aligned. The binding energy E_B of the electrons can be determined from the energy conservation law:

$$E_B = h\nu - E_{\text{kin}} - \phi_{\text{spec}} ,$$

where ϕ_{spec} is the work function of the spectrometer[5]. Note, that the work

[5]The work function is the minimum energy needed to excite electrons from a sample into the vacuum at $T = 0$ K. Since this definition is of limited meaning for the spectrometer, its work function has to be regarded as an effective value.

function of the sample ϕ_{sample} does not enter into the equation.

In a first approximation, the binding energy of the photoelectron is given by the binding energy of the initial core level. The binding energy is not only characteristic of each element, but also depends on the charge density in the ground state (*initial state effect*). However, when the photoelectron is emitted, the remaining electrons rearrange to screen the generated core hole. The extent of the screening strongly depends on the properties of the valence electrons (*final state effect*). These two effects result in differences of the observed binding energies up to several eV. These so-called *chemical shifts* provide sensitivity to the chemical state of a given element.

The spectral profile of an electron that has been photoemitted from one core level is given by a Voigt function, *i.e.*, the convolution of a Lorentz and a Gauss function. Their weighting reflects the ratio of the contributions of life time and experimental broadening. Since part of the electrons undergo energy losses, due to inelastic scattering events in the sample, the main peak is subseeded with an inelastic tail to lower kinetic energies. These contributions are removed from the spectrum by means of a Shirley background, assuming that at a given energy all photoelectrons with higher kinetic energy contribute equally to the inelastic tail. Besides these uncorrelated energy losses there can also be characteristic energy losses by excitation of an additional electron. Within this two-electron process part of the energy is used to excite the second electron to an unoccupied (*shake-up*) or unbound (*shake-off*) state. This results in additional structures at lower kinetic energies.

In the context of this thesis, XPS is mainly utilized to probe the chemical state of sulfur with a binding energy in the range of 162 eV. For measurements of small fractions of sulfur, X-ray guns with typical excitation energies of 1253 eV and 1486.7 eV are not practical, because the photoemission cross section decreases with increasing energetic distance between the binding energy and the excitation energy $E_{\text{exc}} - E_B$ [43]. By using synchrotron light, the photon energy can be tuned to measure at smaller kinetic energies and, thus, higher XPS signals, as well as higher energy resolution. The analysis is carried out with the program *Casa XPS*[6]. The spectra are fitted with a linear and a Shirley background, and pseudo Voigt functions, given by the product of a Lorentz and a Gauss function.

[6] © 2005 Casa Software Ltd

2

EXPERIMENTAL DETAILS

In this chapter details on preparation of samples and measurements are given. In the first section, the design of a water-cooled evaporator for *in-situ* sublimation of organic compounds is presented. This evaporator has been developed within the framework of this thesis, and has been used for the deposition of the Fe complexes. In the following section the ultra high vacuum (UHV) chambers, employed for sample preparation and measurements, are described. In section 2.3 the generation of synchrotron radiation is briefly introduced, and the beamlines at which the experiments were carried out are presented. The last section concerns the preparation of the substrates and their characterization.

2.1 Design of an Evaporator for Organic Compounds

Evaporators for organic compounds are commercially available, however, none of these fully fulfilled the requirements for the preparation samples. Most particularly, the commercially available evaporators lacked the capability to function while pointing downwards and to provide a reliable detection of the flux during the preparation. Therefore, an evaporator for organic compounds has been developed and built in order to overcome these restrictions.

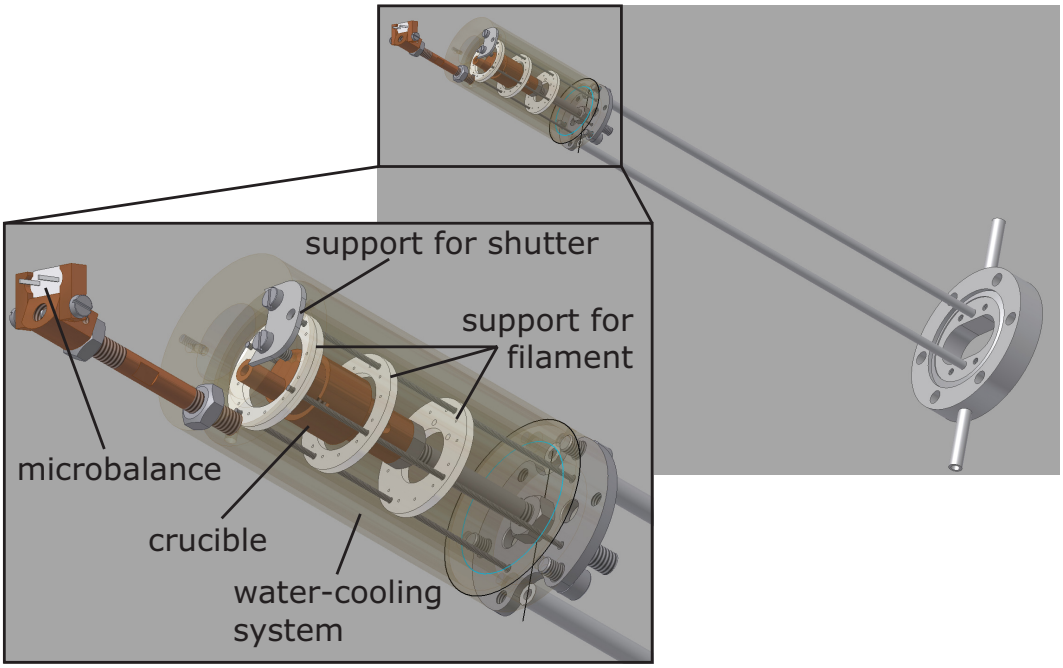

Figure 2.1: Drawing of the main components of the molecule evaporator. The close up shows the mounting of the microbalance, the crucible, the filament and the shutter on the water-cooling shield.

A sketch of the design is shown in figure 2.1. The main components are: a closable tantalum crucible from which the molecules are sublimated, a cage-like filament facilitating a radiative heating of the crucible, a mechanical shutter to control the evaporation time, a quartz microbalance for online detection of the molecular flux, and a water-cooling system to thermally stabilize the microbalance and prevent heating of the environment.

The crucible is made of two tantalum cylinders that are screwed into each other. The one end is then screwed onto the support inside the filament cage. The other end contains a reservoir for the material and an opening through which the molecules are sublimated onto the substrates. This design allows for an evaporation geometry where the opening of the crucible is pointing downwards. The crucible is inserted into the evaporator by means of a hollow stainless steel cylinder with two teeth fitting into the corresponding pockets of the crucible.

The heating is achieved by means of a tantalum wire with a thickness of 0.25 mm mounted through the holes of three *macor* rings resulting in a cage-like appearance. The rings are held by four 1 mm thick stainless steel rods

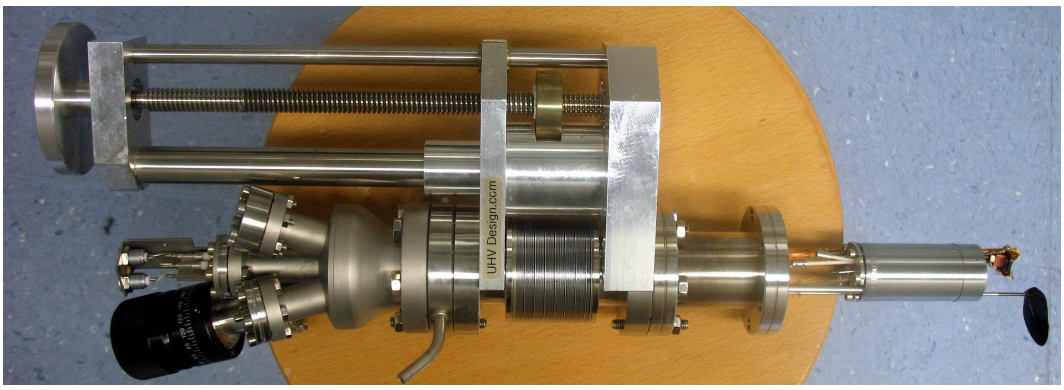

Figure 2.2: Picture of an assembled molecule evaporator, mounted on a linear-motion device. The electrical and mechanical feedthroughs are mounted on a cluster flange.

and separated from each other by ceramic bushes of 2 cm. The assembly is fixed by spot welted swellings before and behind the outer *macor* rings. The heating cage is mounted inside the water-cooling system by the elastic force of tantalum foil, which in addition serves as a passive heat-radiation shield. The crucible is heated by the radiation of the filament and is placed in the middle of the cage. The temperature is detected directly behind the crucible by means of a type-K thermocouple. The position of the crucible can be adjusted by six screws at the base plate that holds the crucible *via* a hollow stainless steel rod. Three of the screws are screwed into the water-cooling system and three are pressing against it. The water-cooling system is made of two hollow stainless steel cylinders[1] welded into each other, in which the water circulates.

During evaporation, the flux of the molecules is detected by a quartz microbalance mounted directly onto the evaporator. A commercial 6 MHz quartz is used as a microbalance after sawing off its cover. The quartz is thermally stabilized by coupling it to the water-cooling system *via* its copper mounting. The frequency shift of the quartz is proportional to the amount of evaporated material. The frequency of the quartz is determined by a frequency counter.

A picture of an assembled evaporator is shown in figure 2.2. The assembly described above is mounted on a CF38 linear motion with 15 cm travel

[1]Hard-soldered copper cylinders, that have been used earlier, caused several UHV leaks.

length. The feedthroughs for the connections of the filament, the thermocouple, the microbalance, as well as the rotation for the shutter are mounted on a cluster flange. The evaporator is mounted onto a UHV chamber behind a VAT CF38 gate valve, so that it can be pumped independently of the chamber by a small UHV pump stand. This set up allows the refill and exchange of molecular material while the chamber is kept fully operational. Once UHV conditions are achieved, the gate valve is opened, and the evaporator is inserted into the chamber by its linear motion. The distance between the crucible and the sample during evaporation of the molecules is in the range of 10 cm to 15 cm depending on the flange which the evaporator is mounted to. Typical evaporation rates are in the range of 0.05 ML/min corresponding to frequency shifts in the range of 1 Hz/min. The tube-like ending of the crucible results in a focused molecular beam with a homogeneous center of 2 cm at the position of the sample.

2.2 Experimental Set Ups

Three different experimental set-ups have been employed to perform the experiments. The XAS measurements as well as the sample preparation were carried out in UHV. Tunable X rays were provided by the synchrotron facilities in Berlin and Grenoble, BESSY II[2] and ESRF[3]. Two UHV chambers were used for measurements at the beamlines UE56/2 and PM3 at BESSY II. The measurements at ESRF were carried out at the high-field magnet endstation at the beamline ID08.

All XAS experiments were carried out by measuring the total electron yield (TEY), *cf.* section 1.5 and 1.6, *via* the drain current of the sample. Since measurements of adsorbates in the submonolayer regime result in small XAS signals, corresponding to currents in the pA range, special care must be taken to minimize electrical perturbations. A resistance higher than 20 GΩ between sample and ground potential turned out to be imperative for current measurements with noise levels below 0.1 pA. A basic scheme for the XAS measurements is given in figure 2.3. The sample is mounted on a rotatable manipulator, allowing for the variation of the X-ray incidence angle.

[2]Helmholtz-Zentrum Berlin für Materialien und Energie (formerly Berliner Elektronenspeicherring-Gesellschaft für Synchrotronstrahlung mbH)

[3]European Synchrotron Radiation Facility

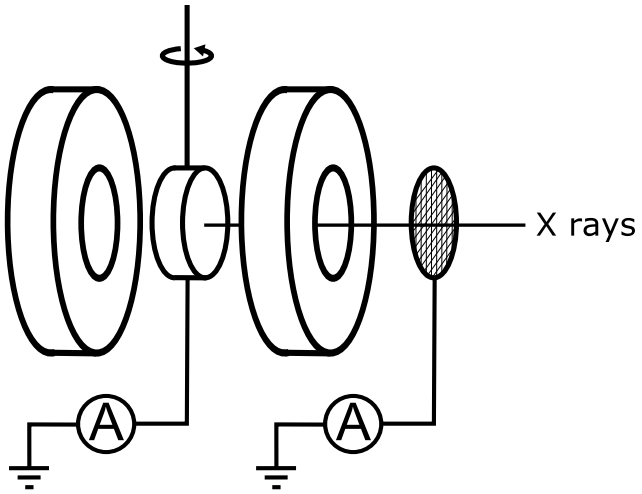

Figure 2.3: Basic XAS measuring scheme showing the propagating X rays, the sample, grid, and coils for magnetic measurements.

For the magnetic measurements, a magnetic field can be applied along the $\vec{k}$ vector of the X rays. The TEY of a gold grid is recorded in parallel to that of the sample. By normalizing the signal of the sample to that of the gold grid, instabilities of the beam, being responsible for part of the noise, cancel out. Within the framework of this thesis such a gold grid was constructed. The gold grid is mounted rotatable in a CF38 double cross allowing for an *in-situ* deposition of gold material from an e-beam-heated tungsten crucible. The cross is mounted between the UHV chamber and the beamline, for the experiments performed at BESSY II.

The experiments described in chapter 3 and section 4.2 were carried out in UHV chamber 1, depicted in figure 2.4 and 2.5. The sample is mounted on an *Omicron* sample plate which can be inserted into the manipulators and transferred inside the UHV chamber. It is possible to transfer samples into and out of the chamber by means of a separately pumped load-lock. Sample preparation and measurements are carried out on manipulator 1. The sample stage can be rotated around both the polar and azimuthal angles. The sample can be heated resistively and cooled by liquid nitrogen. Since such multifunctionality is not compatible with measurements at low temperatures, a second manipulator was set up in the framework of this thesis and mounted to the chamber with an angle of 60° to the horizontal. Manipulator 2 is cooled with liquid He to allow for measurements down to 18 K, this is desirable for studying SCO molecules. The newly designed

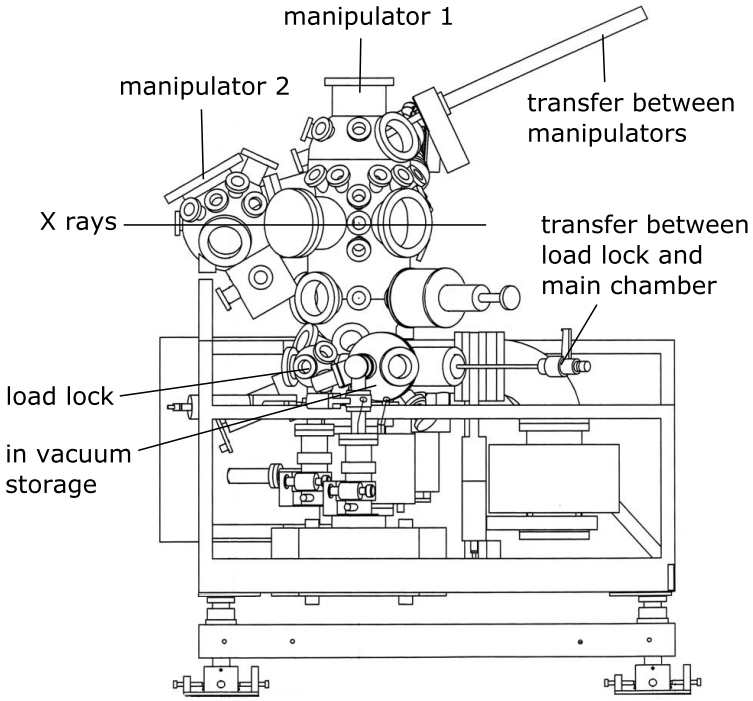

Figure 2.4: Side view of UHV chamber 1 without components. Indicated are the positions of the manipulators, the in-vacuum transfer, and the height at which the X rays traverse the chamber.

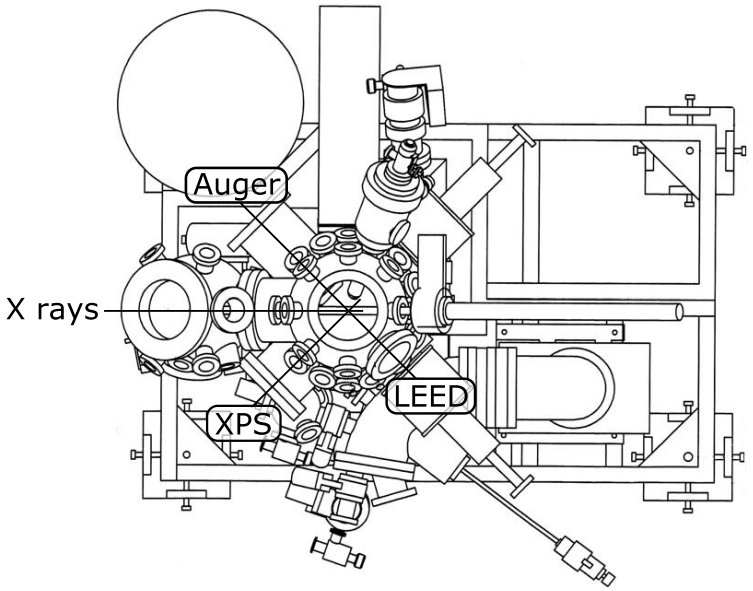

Figure 2.5: Top view of UHV chamber 1 without components. Indicated are the orientations for LEED, Auger, and XPS measurements.

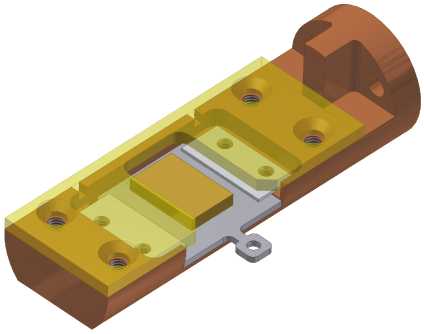

Figure 2.6: Sample holder used in conjunction with manipulator 2. Illustrated are the sample mounted on an *Omicron* sample plate and held with two springs. The Cu cap is depicted transparently.

sample holder is shown in figure 2.6. Here, the sample is held in a Cu block with a Cu cap covering all but a 10 mm by 15 mm section of the sample in order to provide the beam with access to the sample surface. Around the Cu block a passive heat shield made of tantalum foil is mounted. XAS measurements are carried out on both manipulators. XPS measurements are performed on manipulator 1 with the sample surface perpendicular to the axis of a hemispherical mirror analyzer (HMA) and linearly polarized X rays with an incidence angle of 45°. Sputter gun and molecule evaporators are mounted to varying flanges. A screen and a gun for low-energy electron diffraction (LEED) and a cylindrical mirror analyzer (CMA) for Auger spectroscopy are used for sample characterization.

The experiments presented in sections 4.5 and 4.7 were carried out in UHV chamber 2, shown in figure 2.7. The chamber consists of two levels. For XAS measurements, the lower level is equipped with an *in-situ* water-cooled coil system providing applied magnetic fields up to 50 mT [44, 45]. A Cu(100) single crystal is screwed to a tantalum plate mounted to a liquid He flow cryostat. The extraction of all excited electrons is ensured by means of a metal ring on a positive potential of 1.4 kV, mounted close to the sample position. Sample preparation is carried out at the upper level of the chamber. Since the LEED Screen and the Auger system are opposing each other, medium-energy electron diffraction (MEED) can be carried out during deposition of metal films, serving for an accurate calibration of the film thickness. The molecule evaporator is mounted behind a CF38 gate valve, as described in section 2.1.

For the experiments described in section 4.4 a permanently installed

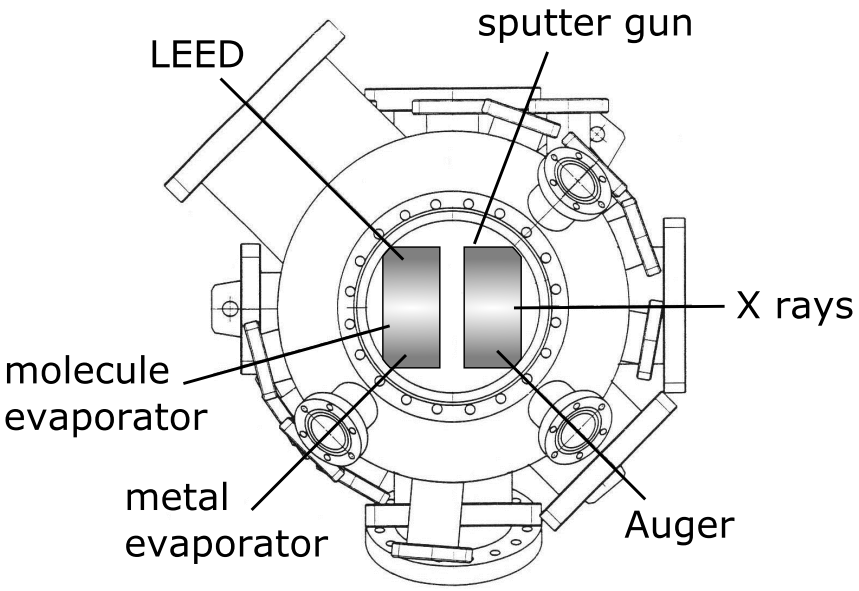

Figure 2.7: Top view of UHV chamber 2 without components. Indicated are the orientations for LEED and Auger measurements, as well as the orientation of the metal and molecule evaporator, and the sputter gun, together with the X-ray propagation direction. In the middle of the chamber the in-vacuum coil system is shown.

end-station at the beamline ID08 at the ESRF were used. XAS and XMCD measurements were carried out in a barrel-like chamber housing a superconducting magnet in a liquid He bath. The samples were prepared in a separate UHV chamber equipped with a scanning tunneling microscope (STM) for the characterization of the sample. The sample is transferred into the chamber of the superconducting magnet in a two-step transfer including an in-vacuum hand over.

2.3 Synchrotron-Radiation Measurements

XAS techniques require tunable X rays of high brilliance. For the experiments presented in this thesis, such X rays were provided by the synchrotron radiation sources BESSY II and ESRF. For the generation of synchrotron radiation, electrons are accelerated to relativistic energies and kept on a circular orbit in an UHV storage ring by means of dipole magnets (bending magnets). The electron storage rings of BESSY II and ESRF have a perimeter of 240 m and 844 m and operate at 1.6 GeV and 6 GeV, respec-

tively. The radiation is generated by the deflection of the electrons by magnets. Due to the relativistic electron energy, the directional characteristic of the radiation is given by a narrow cone tangential to the electron orbit. By means of a monochromator the energy of the X rays can be selectively tuned. Since soft X rays are strongly absorbed by air, the X rays are guided in an UHV tube to the experiment. In addition to the dipole magnets, insertion devices are placed at straight sections of the storage rings. The experiments described in chapter 3 and section 4.2 were carried out at a bending-magnet beamline, whereas for the experiments presented in sections 4.4, 4.5, and 4.7 an undulator was utilized. The latter consists of an array of permanent magnets which force the electrons on an oscillatory trajectory. The emitted X rays coherently interfere which each other, thereby the intensity scales with the number of periods to the power of two. In contrast to bending magnets, the emission spectrum of undulators is given by discrete peaks.

The experiments described in chapter 3 and section 4.2 were carried out at the bending-magnet beamline PM3 at BESSY II. The beamline provides X rays in the range of 200 eV to 1200 eV with horizontal linear or circular polarization. The beamline is equipped with an SX700 plane grating monochromator. A 1200 mm^{-1} grid has been used. The X-ray spot size at the sample position has been $\sim$ 0.3 mm^2. Typical flux densities have been in the range of 10^{16} photons/(s m^2). Due to the continuous spectrum of the bending magnet, the second order component of the X rays, passing the monochromator, can be as high as 20%.

The experiments presented in section 4.5 and section 4.7 have been performed at the undulator beamline UE56/2-PGM2 at BESSY II. The beamline provides X rays in the range of 60 eV to 1300 eV with horizontal or vertical linear as well as circular polarization. Due to the discrete spectrum of the undulator, contributions from the second order of the monochromator in the X rays are below 5%. Spectra below 500 eV photon energy were measured using the first harmonic of the undulator. For spectra above 500 eV the third harmonic was used. In the latter energy range a circular polarization degree of 85% is provided by the beamline [46]. Typical flux densities have been in the range of 10^{17} photons/(s m^2). Energy resolutions were set typically to 150 meV and 300 meV at the N-K edge and the Fe-$L_{2,3}$ edges, respectively. The beamline features a refocusing mirror as the last optical element. Since this is positioned close to the experiment it suffers from the contamination of carbon. This results in a drop of intensity by almost two

orders of magnitude at the C-*K* edge.

The experiments described in section 4.4 were carried out at the undulator beamline ID08 at ESRF. The beamline provides X rays in the range of 400 eV to 1500 eV with horizontal and circular polarization. The beamline is equipped with a spherical grating monochromator. All spectra were measured using the first harmonic of the undulator, providing a circular polarization degree of 100%.

For the spectra presented in chapter 4, the photon energies at the Fe-$L_{2,3}$ edges have been calibrated relative to each other and to the XAS signal of an 15 ML Fe/Cu(100) sample (L_3 maximum at 707.7 eV).

Radiation Damage Effects

When measuring organic molecules with intense X rays, a possible degradation of the molecules by the X rays is an important concern. Damage to a molecule is usually not the consequence of direct interaction between the atoms of the molecule and the X rays, more often such damage is the result of an interaction with secondary electrons produced by the absorption of X rays by the substrate [47, 48]. Sensitivity to X ray-induced damage varies depending on the system being investigated. XAS studies of Mn_{12} showed strong X ray-induced effects, because the complexes are highly sensible to reduction [49]. Measurements of aliphatic SAMs on Au(111) also showed severe degradation effects [47, 50, 51]. However, these effects were largely reduced for SAMs with aromatic constituents [52].

Most of the measurements within this thesis were carried out on Cu and other transition metal substrates. In contrast to Au, the cross section, and thus the amount of secondary electrons experienced by the adsorbate, of Cu is 7 times lower in the energy range of the Fe-$L_{2,3}$ edges and about 3 times lower in the range of the C- and N-*K* edges [53]. Furthermore, all investigated molecules display a strong aromaticity. The proximity to the surface may also stabilize the molecule, since this allows a rapid decay of additional electrons at the molecule [54]. None of the presented samples showed a change in the XA spectra that could be correlated with the illumination time. Although this does not mean that the molecules are not modified at all, the properties that are probed in XAS and XMCD measurements were not affected.

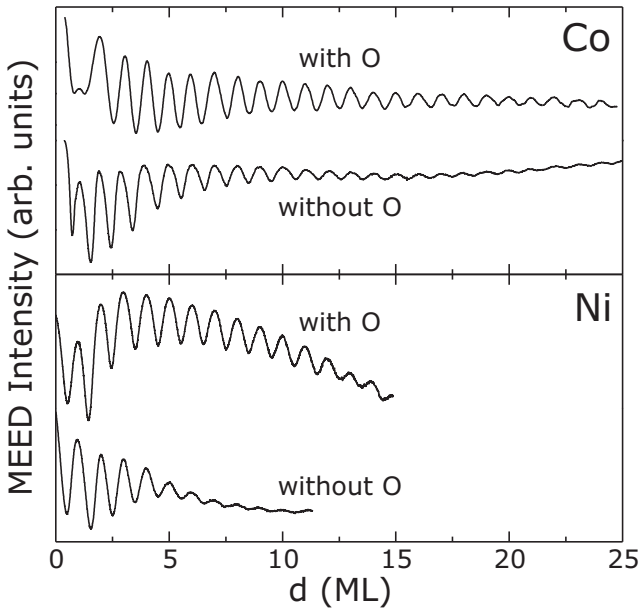

Figure 2.8: MEED intensity oscillations of Co (upper panel) and Ni (lower panel) films deposited onto Cu(100) and O/Cu(100) [24].

2.4 Substrate Preparation

Au(111) and Cu(100) single crystals were cleaned by repeated sputtering and annealing cycles. Sputtering was carried out by Ar^+ bombardment under incidence angles of between 30° and 60° to the substrate surface. Successively, the Au(111) and Cu(100) crystals were heated to 950 K and 800 K, respectively. Through this procedure, atomically flat surfaces, virtually free of contaminations, were obtained, as was verified by XPS, Auger, and LEED measurements.

O/Cu(100) substrates were prepared by annealing a Cu(100) single crystal at 500 K in an oxygen atmosphere. 1200 Langmuir of O_2 were dosed at an oxygen pressure of 2×10^{-6} mbar. This results in a $(\sqrt{2}\times 2\sqrt{2})$R45° reconstruction of the Cu surface as depicted in figure 2.10 (middle panel). The amount of atomic oxygen on the surface corresponds to a coverage of 0.5 ML.

FM Co and Ni films were prepared by means of e-beam evaporation onto Cu(100) and oxygen-covered, reconstructed O/Cu(100) single crystals. During the deposition, the amount of evaporated material was monitored by MEED intensity oscillations. For this measurement it is essential that the

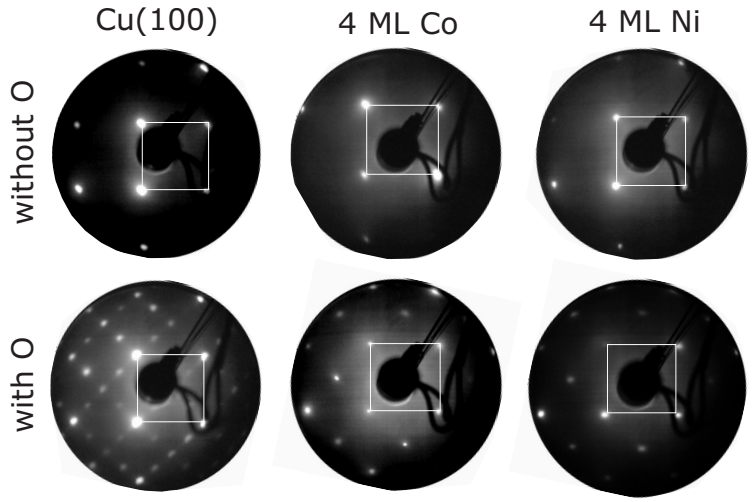

Figure 2.9: LEED patterns of Cu(100) and O/Cu(100) substrates and after the deposition of 4 ML of Co and Ni. The Cu(100) unit cell is highlighted by a white square [24].

sample can be placed between an electron gun and the fluorescent screen. An electron beam of 5 keV was supplied by the electron gun of the Auger system (*cf.* section 2.2), hitting the sample at grazing incidence angles of $\sim 5^\circ$ with respect to the sample surface. The diffraction pattern was visualized by an opposing LEED screen. The intensity of the (00) spot was recorded *vs.* time by means of a CCD camera. The intensity oscillates as a function of the surface roughness, being maximum when a ML is completed.

In figure 2.8 MEED intensity oscillations of Co and Ni films deposited onto bare and oxygen-covered Cu(100) single crystals are shown. For both materials a layer-by-layer growth is observed. The decrease of the amplitude of the intensity oscillations reflects an increasing deviation from pure layer-by-layer growth with increasing thickness. The overall drift of the intensity can be attributed to instabilities of the emission of the electron gun. In the presence of oxygen the layer-by-layer growth is stabilized which is referred to as surfactant growth. Thereby the oxygen floats on top of the surface, as it is known[4] from STM and Auger measurements [59] and depicted in figure 2.10 (right panel).

[4]There is an on-going debate to which extent oxygen atoms might be incorporated into the metallic films during the growth [55–57]. Up to 30% of incorporated oxygen atoms have been deduced indirectly from surface stress measurements [55]. These results have been questioned by Liu *et al.* by means of STM measurements [56, 58].

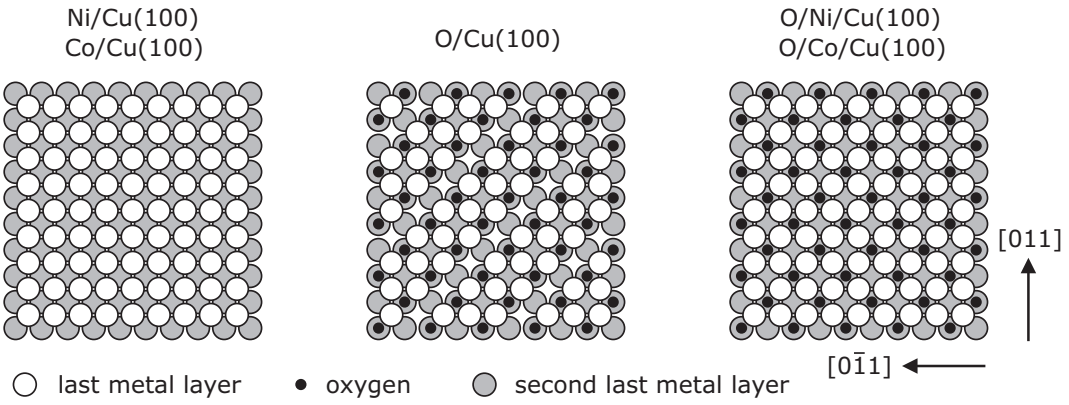

Figure 2.10: Sketch of the position of atoms in the last two metal layers for Ni and Co on Cu(100), for the surfactant-grown films, and the $(\sqrt{2} \times 2\sqrt{2})$R45° reconstructed O/Cu(100) substrate.

Figure 2.9 shows LEED patterns of the substrates obtained before and after deposition of Ni and Co onto a bare (uppper row) and oxygen-covered (lower row) Cu(100) single crystal. The electron energies vary between 176 eV and 217 eV. The white square highlights the unit cell of Cu(100). On Cu(100), Ni and Co films adopt a pseudomorphic growth, as is reflected by the p(1 × 1) LEED pattern. O/Cu(100) presents a $(\sqrt{2} \times 2\sqrt{2})$R45°, so-called missing row, reconstruction of the surface (figure 2.10), and domains with perpendicular orientations of the Cu rows. This results in several additional spots visible in the respective LEED pattern. If Ni or Co material is deposited on top of such a substrate, the oxygen floats on top of the surface resulting in a c(2×2) superstructure of half a monolayer of atomic oxygen, as reflected by the LEED pattern. The oxygen is located at fourfold hollow sites of the Ni and Co films, as shown in figure 2.10.

The magnetic properties of the FM films vary depending on the thickness of the film. The Curie temperature T_C is strongly reduced with respect to the bulk values of 1388 K and 627 K of Co and Ni, respectively [60]. This is the result of the reduction in magnetic correlation length perpendicular to the surface, as it is described by the so-called *finite-size law* [61]. While the easy axis for Co films lies in-plane along ⟨110⟩ directions, Ni films undergo a spin-reorientation transition (SRT) from in- to out-of-plane at a thickness of 11 ML [59, 62, 63]. The SRT is shifted to smaller thicknesses upon the adsorption of adsorbates [59, 63].

On top of these substrates, Fe complexes were deposited by means of

sublimation from a Knudsen cell (*cf.* section 2.1).

3

SPIN-CROSSOVER MOLECULES ON SURFACES

3.1 Introduction

The spin-crossover (SCO) phenomenon in transition metal complexes relies on a metastable arrangement of the 3*d* electrons of the central ion in the ligand field constituted by the surrounding atoms. A minute balance between the electron–electron repulsion, favoring a parallel arrangement of their spins according to Hund's rule, and the ligand-field splitting, in favor of a pairwise filling of the lower energy levels, is necessary. The former leads to a maximum total spin (high spin, HS), while in the latter case a minimum total spin (low spin, LS) is displayed. The energy differences determining the spin state are in the order of meV. This makes the transition sensitive to a variety of tiny perturbations, such as thermal excitations, pressure [64], and interaction with solvents or adjacent molecules [65].

A temperature-induced SCO transition had first been reported in 1931 by Cambi *et al.* [66, 67]. Such a transition occurs, if the LS state is slightly higher in energy then the HS state. Due to its higher multiplicity, the entropy of the HS state is higher than that of the LS state. As a result the HS state is stabilized at higher temperatures. While the SCO transition for complexes in solution can be described by Boltzmann statistics and acts on a temperature scale in the range of 100 K, intermolecular interactions of these

complexes in their solid phase result in cooperative transitions, giving rise to a complex temperature-dependent behavior. Abrupt changes of the spin state, hysteresis, and multiple transition phenomena have been reported [68, 69]. Decurtins *et al.* [70, 71] reported on a photo-induced switching of the spin state in 1984. By irradiation with light, the HS state can be populated at the expense of the LS state. At low temperatures, the energy barrier between the LS and HS states, due to the large difference in metal–ligand bond length, cannot by overcome by thermal excitations, as a consequence the spin state is trapped. This phenomenon is referred to as *light-induced excited spin-state trapping* (LIESST) [72]. These effects have been extensively studied by Mössbauer spectroscopy [73, 74], SQUID [75], X-ray diffraction [76–78], as well as XAS [79–81] and EXAFS [82, 83] measurements. The existence of bistable states and the pronounced change of color, concomitant with the spin transition, led to the prospect of utilizing these complexes in data storage devices and displays [84].

The vision of exploiting the high sensitivity of SCO complexes to functionalize surfaces is appealing, since they may sense tiny changes in a supramolecular arrangement, or changes in the properties of a surface, that are not accessible to a direct read-out. The sensitivity of SCO molecules is a strength on the one hand, but on the other hand, it makes the preparation a challenge. The smallest influence on the electronic structure could shift the balance of the metastable arrangement of the *d* electrons to one or the other side. The formation of hydrogen bonds, intermolecular stress within a monolayer, or hybridization of the molecular orbitals with those of a surface will likely suppress the transition.

Thin layers of SCO molecules on surfaces in the monolayer regime have rarely been investigated due to the limitations dictated by the preparation method. The *in-situ* deposition by sublimation of these complexes in UHV requires a high thermal stability of the molecules [85]. In addition, many SCO complexes form salts, resulting in high sublimation temperatures, due to the ionic interaction. A flexible approach is the deposition of the molecules by means of electrospray ion-beam deposition [86, 87], but it requires a great technical effort. The *in-situ* deposition of large molecules by dosing a solution through a fast operating pulse valve into UHV has also been reported [88, 89]. Matsuda *et al.* [90] report on an SCO transition of a 30 nm thick film of $Fe(bpp)_2(BF_4)_2$ (bpp = 2,6-bis(pyrazol-1-yl)pyridine), prepared by spin coating onto a glass substrate. However, this method is

not suited to obtain a well-defined arrangement of molecules in the monolayer regime, since it provides no mechanism to remove residual adsorbates from the surface inherent to *ex-situ* deposition methods. Such layers can be obtained through the deposition of molecules onto gold surfaces from solution by means of a sulfur-containing anchor group. The formation of well-ordered monomolecular layers is frequently described in literature and referred to as a *self-assembled monolayer* (SAM) [91–94]. However, it usually requires a chemical modification of the SCO complex that might suppress the occurrence of the spin transition. A preparation of SCO molecules as Langmuir-Blodgett films has also been reported in [95, 96].

In the context of this thesis various SCO complexes have been investigated as molecular layers in the monolayer regime. In section 3.2 the results obtained by *in-situ* sublimation of $Fe(phen)_2(NCS)_2$ and $Fe(phen)_2(NCSe)_2$ onto Au(111) and NaCl/Cu(311) substrates are described. Section 3.3 presents XAS measurements of 5 ML and 1 ML of $Fe(bp)_2$ on Au(111). A self-assembled monolayer of $Fe(bppmc)_2$ was investigated by means of S $2p$ XPS, and Fe-$L_{2,3}$ and N-K XAS, presented in section 3.4. The spin state of the molecules on the surface is determined by the comparison of the Fe-$L_{2,3}$ XAS signal to that of the bulk material. The influence of the spin transition on the electronic structure of the N atoms of the ligands is investigated by means of N-K edge XAS.

3.2 Iron Phenanthroline Complexes

$Fe(II)(phen)_2(NCS)_2$ (phen=1,10-phenanthroline) was the first synthetic Fe(II) complex reported to show a spin-crossover transition [97]. $Fe(phen)_2(NCS)_2$ is a neutral SCO complex. The central, divalent Fe ion is surrounded by two bidentate phenanthroline ligands and two monodentate isothiocyanate ligands, which compensate the positive charge of the Fe. A structure formula is given as an inset of figure 3.1 (upper panel). The complex shows a pronounced LIESST effect and has been widely studied as a bulk material [77, 80, 97, 98]. It shows a cooperative SCO effect with an abrupt transition centered at 176 K [98]. For $Fe(phen)_2(NCSe)_2$, the isothiocyanate ligands are exchanged with isoselenocyanate. For a high-quality single crystal of $Fe(phen)_2(NCSe)_2$, an abrupt transition centered at 235 K was reported [78]. However, it was pointed out that the SCO behavior crit-

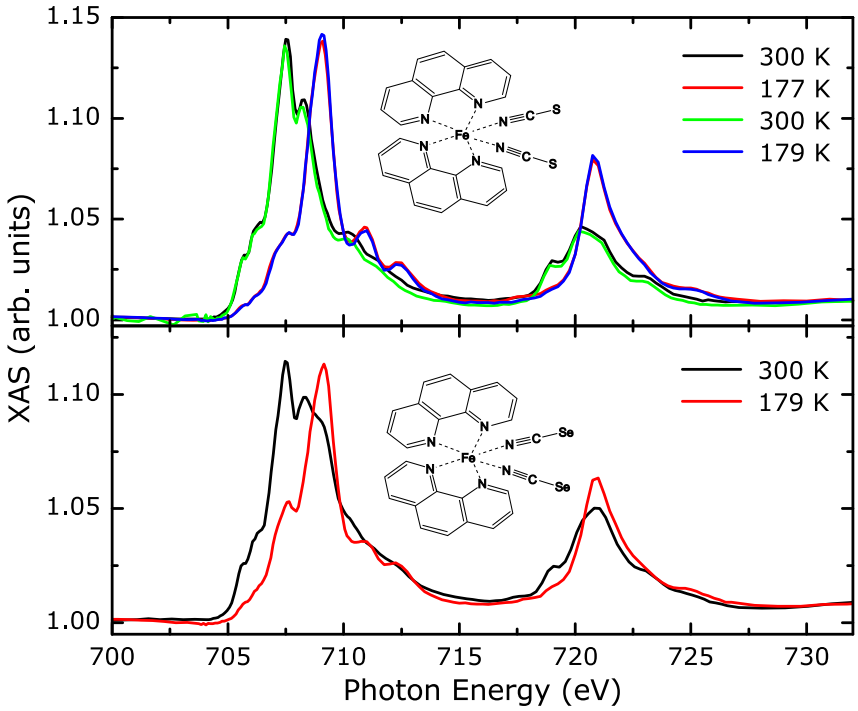

Figure 3.1: Fe-$L_{2,3}$ XAS signals from bulk material of $Fe(phen)_2(NCS)_2$ (upper panel) and $Fe(phen)_2(NCSe)_2$ (lower panel) recorded by consecutive temperature-dependent measurements.

ically depends on the method of sample preparation. The SCO transition was monitored at the Fe-$L_{2,3}$ as well as the Fe-K edge for $Fe(phen)_2(NCS)_2$ and $Fe(phen)_2(NCSe)_2$ [79–81]. XAS measurements at the N-K edge have not been carried out so far.

Figure 3.1 shows temperature-dependent XA spectra at the Fe-$L_{2,3}$ edges of the bulk material of $Fe(phen)_2(NCS)_2$ (upper panel) and $Fe(phen)_2(NCSe)_2$ (lower panel). The samples were prepared by stamping the powder of the molecules into an indium foil. For $Fe(phen)_2(NCS)_2$, the typical signatures of the HS and LS states could be observed at the Fe-$L_{2,3}$ edges [79, 81] for spectra taken at 300 K and about 180 K, respectively. The change of the Fe-$L_{2,3}$ XAS signal is fully reversible, as can be seen from successive measurements at 300 K, 177 K, 300 K, and 179 K. The spectra were recorded at the bending magnet beamline PM3 at BESSY. No time dependence of the spectra at constant temperature was observed, indicating the absence of beam-induced damage or spin transition (*soft X-ray induced excited spin-state trapping* [80]) of the molecules on the time scale of several measurements ($\sim$ 1 hour). The spectral shape can be understood consider-

ing the change in occupation of the 3*d* levels [99]. For a ligand field with cubic symmetry, the 3*d* levels split into t_{2g} (d_{xy}, d_{xz}, and d_{yz}) and e_g ($d_{x^2\text{-}y^2}$ and d_{z^2}) manifolds. In the HS state, both manifolds are partly filled and thus contribute to the Fe-$L_{2,3}$ spectra. In the LS state, the t_{2g} manifold is completely occupied. Hence, only the e_g manifold contributes to the Fe-$L_{2,3}$ spectra, so that the Fe-$L_{2,3}$ edges are shifted towards higher photon energies with respect to the HS case. This effect is additionally enhanced by the increase of the ligand field splitting in the LS state.

The evaluation of the branching ratio presents a more general approach to distinguish the two possible spin states by means of Fe-$L_{2,3}$ XAS [100, 101]. This is the ratio of the integrated area of the L_3 to L_2 peaks according to $A_3/(A_3 + A_2)$, $A_i = \int_{L_i} I(E)\mathrm{d}E$, where $I(E)$ is the XAS intensity of the $p \rightarrow d$ transition (*cf.* section 1.4.1). Differences in the branching ratio are a consequence of a different spin-orbit splitting of the 3*d* electrons for the two spin states. In the absence of a 3*d* spin-orbit splitting, the *statistical branching ratio* of 2/3 would be observed, reflecting the occupation of the $2p_{3/2}$ and $2p_{1/2}$ levels. This value is expected for an LS arrangement of the d^6 electrons since $S = 0$. For the spectra shown in the upper panel of figure 3.1, values of 0.78 and 0.69 are found for the branching ratio of the Fe-$L_{2,3}$ XAS signals at 300 K and 170 K, respectively.

For $Fe(phen)_2(NCSe)_2$, the spectral shape of the Fe-L_3 edge indicates a mixture of HS and LS states at room temperature. The ratio of HS to LS states is estimated as 2 : 1, by comparison to the Fe-$L_{2,3}$ spectra of $Fe(phen)_2(NCS)_2$. At 179 K a predominant LS signal is found, corresponding to a HS–LS ratio of 1 : 10.[1] The presence of a mixed spin state for the two temperatures indicates a much broader spin transition as compared to $Fe(phen)_2(NCS)_2$, which would be expected if the spin transition were less cooperative. The discrepancy to reference [78] might be attributed to a lower degree of order in the micro-crystalline powder of the molecules measured here.

The rearrangement of the Fe 3*d* electrons is accompanied by a modification of the molecular structure. X-ray diffraction measurements have shown that the iron–nitrogen bond length is reduced by 10% upon spin transition [102]. The influence of the rearrangement of the Fe-3*d* electrons on the elec-

[1] Measurements at elevated temperatures had not been carried out, due to the risk to contaminate the UHV chamber with indium (melting point: 429.75 K) used as a support for the molecular powder.

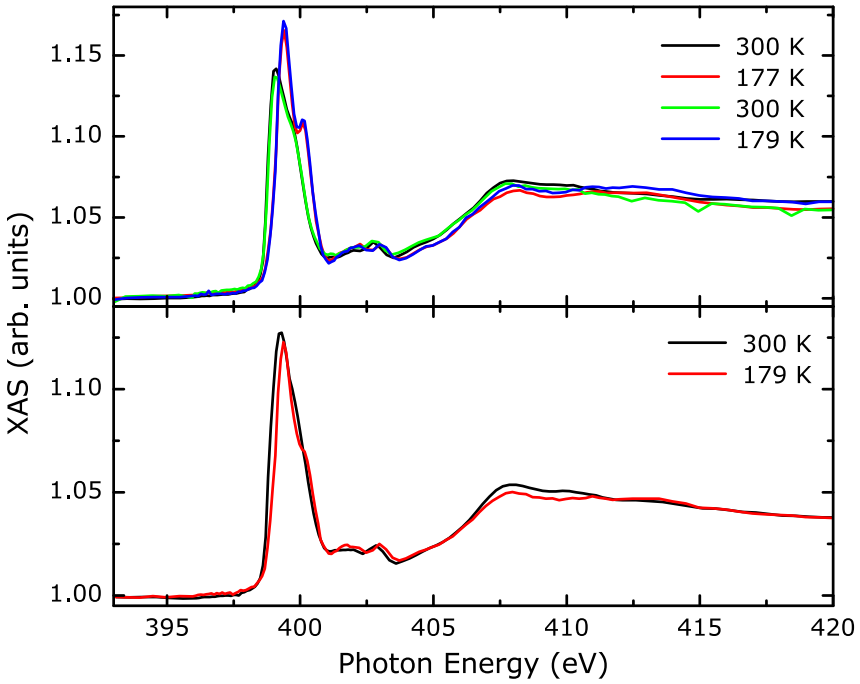

Figure 3.2: N-*K* XAS signal of $Fe(phen)_2(NCS)_2$ (upper panel) and $Fe(phen)_2(NCSe)_2$ (lower panel) as bulk materials recorded by consecutive temperature-dependent measurements.

tronic structure of the nitrogen ligands, can be probed at the N-*K* edges. In figure 3.2 the corresponding XA spectra are shown for the bulk material of $Fe(phen)_2(NCS)_2$ and $Fe(phen)_2(NCSe)_2$. A pronounced temperature-dependent change of the N π^* resonances is found for $Fe(phen)_2(NCS)_2$. This change is fully reversible. The spectra recorded at room temperature show a peak at 399.1 eV with a shoulder at 399.8 eV. For the spectra at low temperature, a double peak with maxima at 399.4 eV and 400.1 eV is observed. The area ratio of the two peaks of approximately 2 : 1 suggests an assignment of the lower energy peak to the nitrogen atoms of the phenanthroline ligands, whereas the peak at higher energy can be assigned to the isothiocyanate ligands. At higher temperature the splitting of the peaks is reduced. However, a simulation of the observed XA spectra by means of density functional calculations [103, 104] would be necessary to substantiate the proposed assignment. For $Fe(phen)_2(NCSe)_2$, a much smaller change of the N-*K* XAS signal is visible. This can be attributed to the presence of a mixture of spin states. But for low temperatures, the two peaks are hardly separated. This indicates that the electronic modification at the nitrogen site upon the spin transition is smaller for $Fe(phen)_2(NCSe)_2$ than for

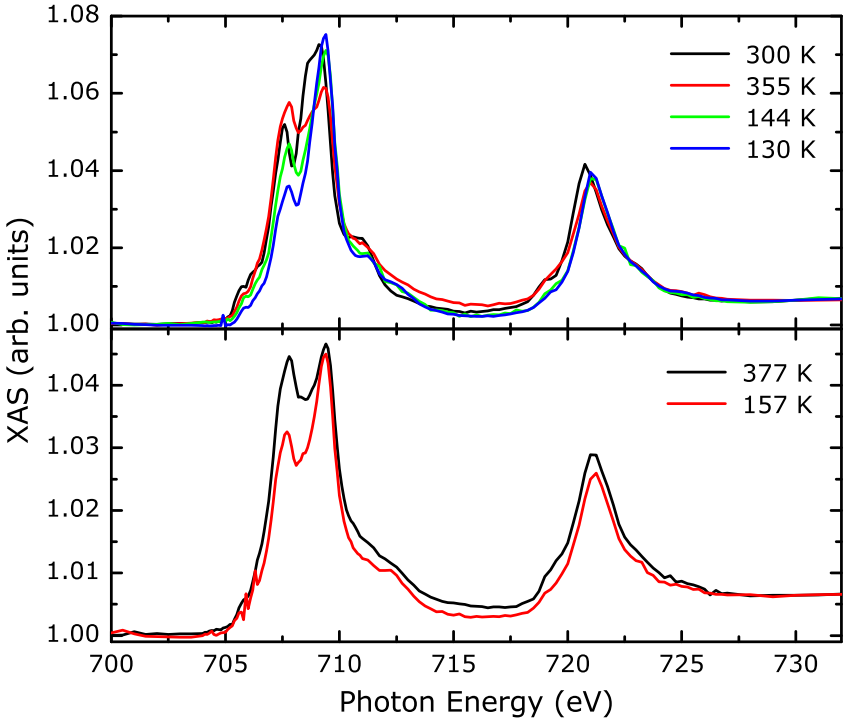

Figure 3.3: Temperature-dependent Fe-$L_{2,3}$ XAS signal of a multilayer of $Fe(phen)_2(NCS)_2$ and phenanthroline on Au(111). The six spectra have been measured in the sequence indicated by the order in the legends.

$Fe(phen)_2(NCS)_2$.

Our focus is to study the SCO transition of $Fe(phen)_2(NCS)_2$ and $Fe(phen)_2(NCSe)_2$ on surfaces. Since these are neutral complexes, the preparation is attempted by *in-situ* sublimation of the molecules. $Fe(phen)_2(NCS)_2$ was evaporated in UHV from a Knudsen cell at 500 K. The evaporation process is accompanied by the production of N- and C-containing fragments, as seen from a strongly enhanced relative intensity of the C- and N-*K* XAS signals from a deposition at lower temperatures. Several attempts to inhibit the production of fragments were performed: The deposition rate was reduced to evaporate at lower temperatures, the tantalum crucible of the evaporator (*cf.* section 2.1) was replaced by an open glass crucible to increase the evaporation efficiency by the cylindrical geometry and to exclude a potential interaction of the molecules with the tantalum crucible. However, the production of fragments could not be suppressed, but seems to be an inherent part of the evaporation process.

Figure 3.3 shows the Fe-$L_{2,3}$ edges of $Fe(phen)_2(NCS)_2$ on Au(111) with an effective coverage of approximately 5 ML. The coverage is deduced from the intensity of the Fe-L_3 signal and the size of the molecule. However, the complexes are incorporated in a layer of N- and C-containing fragments, as will be discussed below. The initial spectrum at room temperature displays a shape consistent with a mixed spin state of predominant LS character. When heated to 355 K, spectral weight is shifted to lower photon energies, as would be expected for an increase in the number of molecules presenting a HS state. However, the increase in temperature might also cause a chemical reaction with the fragments or desorption of molecules. Subsequently, the sample was cooled to 130 K and a sizable shift of intensity to higher energies is observed. This is a clear indication of a transition from HS to LS states, since a decrease in temperature cannot result in chemical reactions or desorption of molecules. In turn, this proves that the Fe signal observed indeed stems from intact $Fe(phen)_2(NCS)_2$ molecules. Already the occurrence of an LS state indicates the presence of intact $Fe(phen)_2(NCS)_2$ complexes, since a disintegration of the molecules results in a reduced ligand field, favoring a HS state. The Fe-$L_{2,3}$ spectrum at 130 K is similar to the spectrum for bulk $Fe(phen)_2(NCS)_2$ at 177 K, shown in the upper panel of figure 3.1. The peak at 707.7 eV can be attributed to a residual HS Fe species of approximately 20%. The lower energy peak at 707.7 eV gains intensity, when the sample is heated up again to 377 K (lower panel), signifying an increase of the percentage of molecules displaying a HS state. In addition, the overall intensity decreased, implying a desorption of molecules from the surface. When the sample is cooled down to 157 K, the LS signature in the spectrum is restored again. However, the percentage of molecules displaying a non-variable spin state seems to be increased.

In contrast to the Fe-$L_{2,3}$ XAS signal, the C- and N-K edge XAS signals relative to the Fe XAS signal are reduced by a factor 2 when heating the sample the second time to 377 K. This implies the presence of N- and C-containing fragments on the surface. When the sample is heated, these fragments desorb from the surface and also cause a desorption of some of the Fe-containing molecules. The behavior with respect to the sulfur can be best followed by means of XPS. The area ratio of the N 1s, C 1s, and S 2p XPS peaks before and after heating up was $5:1$, $5:1$, and $1:1$, respectively. This implies that the fragments do not contain sulfur. Thus, these fragments are most likely phenanthroline molecules, produced during the evaporation process by the reaction of $Fe(phen)_2(NCS)_2$ molecules with each other.

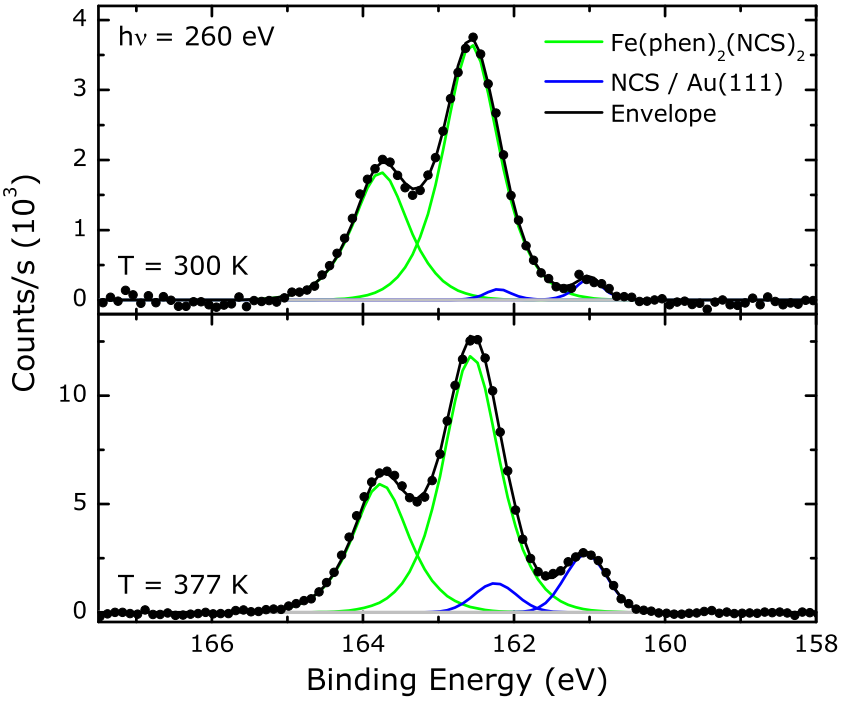

Figure 3.4: S $2p$ XPS spectra of a multilayer of $Fe(phen)_2(NCS)_2$ and phenanthroline on Au(111) excited with 260 eV at 300 K and 377 K. The green line shows the fit for sulfur assigned to the thiocyanate ligand of the complex. The blue line represents a sulfur species of disintegrated complexes.

In figure 3.4, the S $2p$ XPS spectra are shown, measured with an excitation energy of 260 eV before (upper panel) and after (lower panel) heating the sample to 377 K. The spectra are fitted with two doublets with the S $2p_{3/2}$ peak centered at 162.4 eV and 161.0 eV, respectively. For each doublet, the areal ratio between the S $2p_{3/2}$ and the S $2p_{1/2}$ peak is fixed to 2 : 1 and the energy splitting to 1.2 eV. The binding energy is calibrated relative to the Au $4f_{7/2}$ peak of the substrate set to 84.0 eV. Before heating, a ratio of 15 : 1 is found between the S $2p_{3/2}$ peaks at 162.4 eV and 161 eV. After heating, a ratio of 5 : 1 is observed. The presence of two different sulfur species in the latter case can be explained by considering an interaction between the sulfur-containing thiocyanate ligands and the gold surface [105, 106]. Before annealing, the $Fe(phen)_2(NCS)_2$ molecules are embedded in a layer of phenanthroline molecules, inhibiting the direct contact of the major part of the $Fe(phen)_2(NCS)_2$ molecules with the surface. During annealing, the phenanthrolin molecules partly desorb, and an increasing fraction of the

$Fe(phen)_2(NCS)_2$ molecules come into contact with the surface. As a consequence, some of the isothiocyanate ligands might undergo a chemical reaction with the gold surface, which could result in the disintegration of the $Fe(phen)_2(NCS)_2$ molecules, and thus lead to a decrease of the ligand field strength experienced by the Fe ion. Hence, an irreversible increase of the HS state of the Fe ions would be expected.

For $Fe(phen)_2(NCSe)_2$, less production of fragments during the evaporation process was observed, as indicated by the N-*K* XAS signal with respect to the background. When evaporated onto Au(111), a HS signature of the Fe-L_3 XAS signal could be observed, which does not change when cooling down to 140 K. However, a chemical reaction of the selenocyanate ligand with the gold surface cannot be excluded.

Although Au(111) is a comparably inert surface, chemical reactions between gold and sulfur or selenium atoms are well known [91–94]. The reactivity is even stronger for other metals like, for example, copper. Since a conducting sample is a prerequisite for the measurement technique, an isolator cannot be used as substrate. However, a strategy to prevent a direct contact of the molecules with the metal surfaces, but to maintain a well defined surface, is to cover the metallic surface with a thin inert layer of a few monolayers of isolating material. Such substrates can be obtained from oxides, for example, CoO/Ag(100) or MgO/Ag(100) [107, 108]. Here, NaCl was grown on Cu(311) in order to achieve a decoupling of the molecules and the metal. The growth of NaCl is well studied [109, 110]. On Cu(311), NaCl forms a complete first monolayer, due to a strong affinity to the Cu(311) surface. A carpet-like growth is observed even on step etches of the copper surface. If the substrate is kept at 400 K during the evaporation process, also the second monolayer is completed before a three-dimensional growth mode of the NaCl occurs [111]. NaCl was sublimated from a Knudsen cell at 700 K onto a Cu(311) single crystal held at 400 K. Successively, $Fe(phen)_2(NCS)_2$ or $Fe(phen)_2(NCSe)_2$ were evaporated onto the substrate held at 300 K. On NaCl, both molecules display a mixture of HS and LS states after evaporation. An increase of the LS signature in the Fe-$L_{2,3}$ XAS signal at low temperatures could not be observed, indicating that an efficient decoupling of the molecules could not be achieved. This is corroborated by the observation of a second species in the S 2*p* XPS growing upon temperature increase, as it was observed in the case of the Au(111) surface. This can be explained by copper adatoms, diffusing on the NaCl surface, or a dislocation of NaCl at

domain boundaries or at step bunches of the Cu(311) substrate. Details on this study can be found in reference [112].

3.3 Iron Bispyridyl-pyrrole Complex

In the previous section, a metastable spin-state could be demonstrated for $Fe(phen)_2(NCS)_2$ molecules embedded in a layer of phenanthroline molecules. The spin-crossover transition seemed to be suppressed if the molecules were in direct contact with the Au(111) surface. In addition, the reliability of the preparation suffered from the production of phenanthroline fragments as an inherent part of the evaporation process. The preparation by sublimation of the molecules in UHV is beneficial, since it provides control on the choice of the substrate and the coverage. It would be desirable to utilize a complex that is thermically stable at temperatures allowing for the sublimation of the molecules in UHV. In addition, a chemical reaction with the surface has to be prevented.

$Fe(II)(bp)_2$ (bp=2,5-bis(2-pyridyl)pyrrole) is a neutral complex. Its ligand field is constituted by two tridentate bispyridyl-pyrrole ligands. A structure formula is given as an inset of figure 3.5. The higher denticity leads to an increase in thermal stability. The sublimation at 1.4×10^{-3} mbar was shown to occur at 487 K [113]. The periphery of the molecule only contains carbon atoms, which are not expected to form a covalent bond to gold.

Figure 3.5 shows the XAS signals at the Fe-$L_{2,3}$ edges of 5 ML of $Fe(bp)_2$ on Au(111) at room temperature and the corresponding spectra for a polycrystalline bulk sample measured at normal X-ray incidence. Since only the first monolayer is in direct contact with the gold surface, and the sublimation was already demonstrated [113], it can be safely concluded that the major part of the signal, if not the whole signal, stems from intact molecules. It is known from NMR and SQUID measurements, that $Fe(bp)_2$, as a bulk material, presents a HS state [113]. The similarity between the two spectra suggests that $Fe(bp)_2$ in the multilayer on Au(111) also presents a HS state. However, subtle differences of the Fe-L_3 edge are observed. A HS state is consistent with the observed branching ratio of the L_3 and L_2 edge of 0.77 and 0.78 for the $Fe(bp)_2$ multilayer and bulk material, respectively.

Fe-$L_{2,3}$ XA spectra for 1 ML of $Fe(bp)_2$ on Au(111) are depicted in figure 3.6. The spectrum at 300 K closely resembles the corresponding spectra

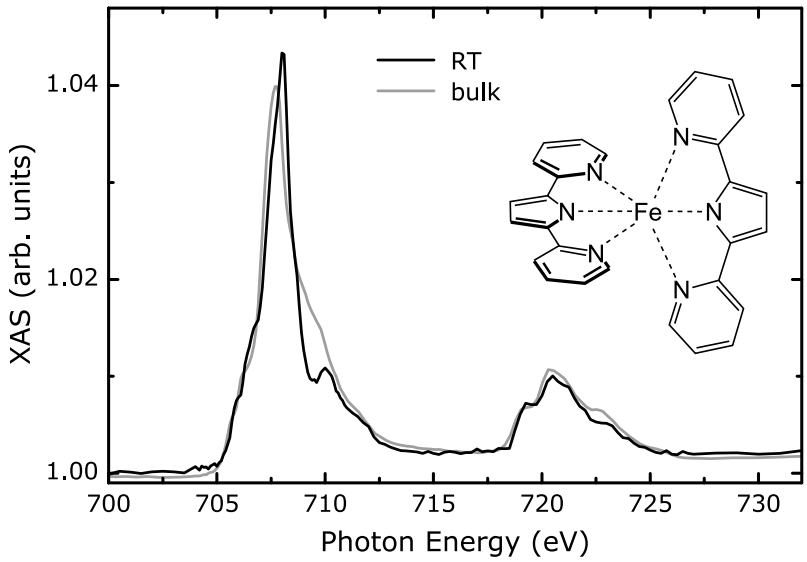

Figure 3.5: Fe-$L_{2,3}$ XAS signals of 4.5 ML of $Fe(bp)_2$ on Au(111) (black line) and as a bulk material (gray line), scaled to about the same height. Inset: Structure formula of the complex.

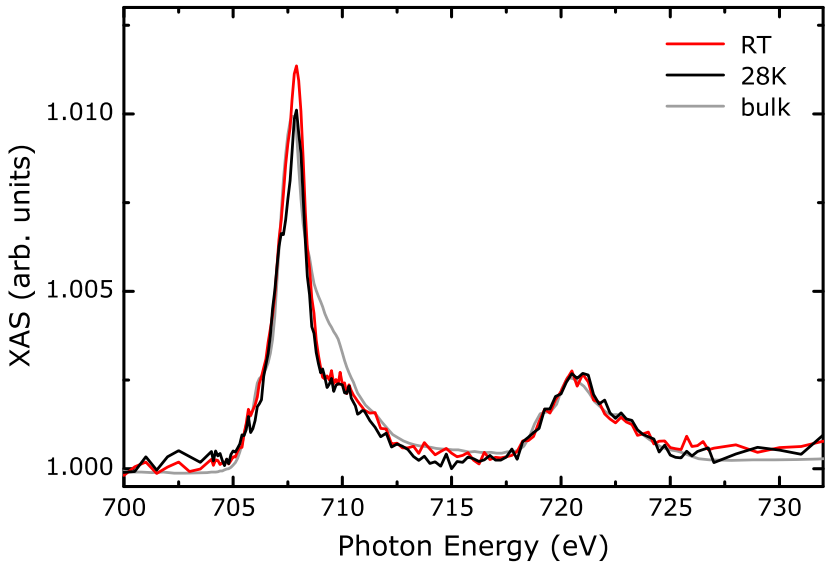

Figure 3.6: Temperature-dependent Fe-$L_{2,3}$ XAS signal of 1 ML of $Fe(bp)_2$ on Au(111) (black line). The gray line depicts the corresponding spectra of the bulk material of $Fe(bp)_2$ recorded at room temperature and scaled to about the same height.

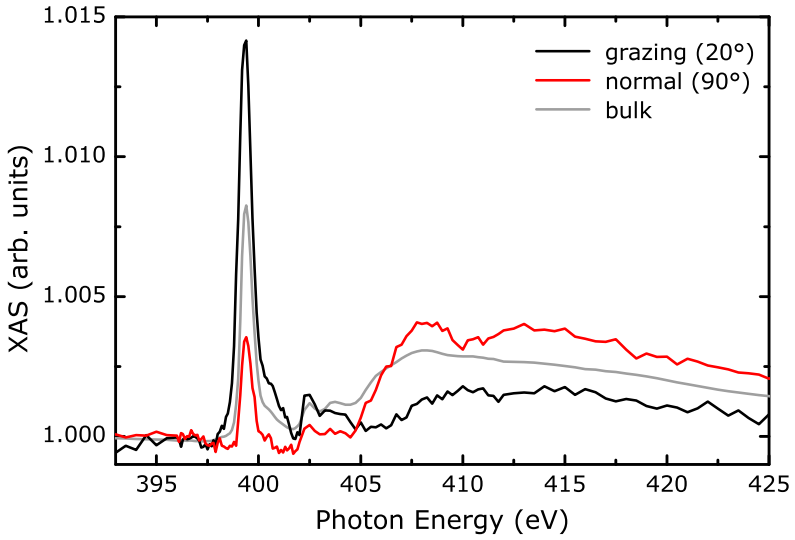

Figure 3.7: Angle-dependent N-*K* XAS signals of 1 ML of $Fe(bp)_2$ on Au(111), and the corresponding isotropic spectrum of the bulk material scaled to about the same height.

of the multilayer of $Fe(bp)_2$, shown in figure 3.5. This implies that the integrity of the molecule is preserved even when in direct contact with the gold surface. No change of the Fe-$L_{2,3}$ line shape is observed upon cooling to 28 K. This implies that the strength of the ligand field has to be increased in order to obtain a metastable arrangement of the Fe 3*d* electrons.

The adsorption geometry of the molecule on the surface is investigated by means of angle-dependent measurements at the N-*K* edge. Figure 3.7 presents the N-*K* XAS signals for 90° (normal, red line) and 20° (grazing, black line) X-ray incidence. A clear intensity difference of the N π^* resonance at 399.3 eV is found. Analysis of the observed intensity ratio results in an average tilt angle of the unoccupied N π^*-orbitals of 32° with respect to the surface normal, according to equation 1.6. Such value is consistent with an adsorption geometry, where the plane constituted by perpendicularly oriented N π^*-orbitals of the ligands is oriented perpendicular to the surface. In that case an average tilt angle of 35.3° is expected. However, a small distortion of the molecule leading to a preferential alignment of the ligands parallel to the surface might also contribute.

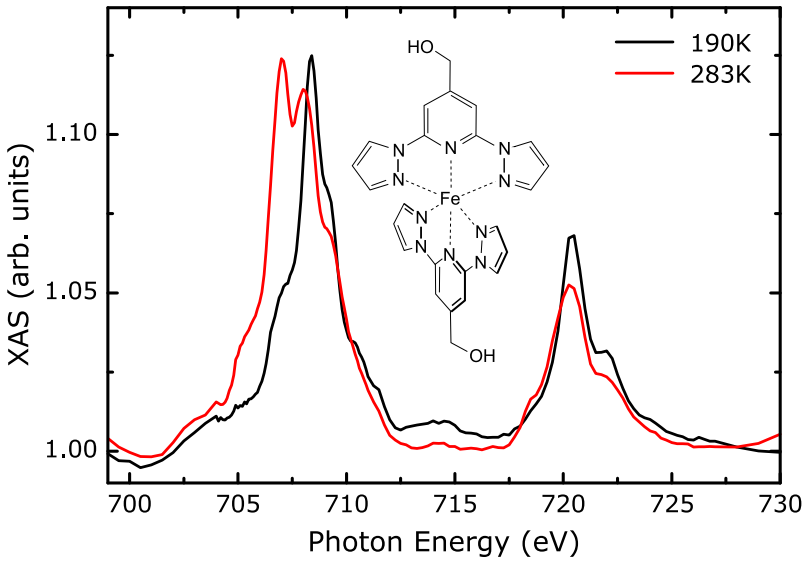

Figure 3.8: Temperature-dependent Fe-$L_{2,3}$ XAS signal from bulk material of $Fe(bppm)_2(BF_4)_2$. Inset: Structure formula of the complex.

3.4 Iron Bispyrazolyl-pyridine Complexes

The preparation of thin layers of SCO molecules by sublimation in UHV, on the one hand, provides the flexibility to choose the coverage and the substrate. On the other hand, however, it restricts the choice of the molecule to the ones that are sublimable in UHV. Many SCO complexes form salts, where the charge of the central metal ion is not compensated by the surrounding ligands but by additional anions. Due to the ionic interaction, the temperature necessary for sublimation is usually higher than the temperature at which the molecules disintegrate. In this chapter, a different route to prepare a monomolecular layer of molecules on gold substrates is introduced. The molecules are deposited from solution onto gold-coated mica substrates by means of sulfur-containing linker groups attached to the molecules. During the deposition process, the sulfur atoms form a covalent bond to the gold surface, displacing weakly bound contaminations from the gold surface. This primary adsorption process occurs on the time scale of a few seconds. Successively, the density of the adsorbed ensemble is increased by a rearrangement of the molecules at the surface. This leads to a densely packed, potentially well-ordered monomolecular layer of molecules defined by the intermolecular interactions of the molecules within the ensemble. Such a system is referred to as a self-assembled monolayer (SAM) [91–94].

Here, Fe(II)(bppm)$_2$(BF$_4$)$_2$ (bppm=2,6-bis(1H-pyrazol-1-yl)-4-(hydroxymethyl)pyridine) was chosen as a starting point for a chemical modification. This Fe(II) complex consists of two tridentate ligands surrounding the Fe center, as depicted in the inset of figure 3.8. Many derivates of this complex are reported to show an SCO transition [75, 114–116]. The synthetical goal is to attach a sulfur-containing linker group to the complex that allows for a self assembly of the molecule on a gold surface, while maintaining the metastable arrangement of the Fe 3*d* electrons required for a spin-crossover transition. The only successful synthesis of an Fe(II) bispyrazolyl-pyridinyl complex with sulfur-containing anchor groups that showed an SCO transition was reported by Chandrasekar *et al.* [117]. However, the complex was only measured as bulk material and not deposited onto a gold surface.

Fe(bppm)$_2$(BF$_4$)$_2$ as a bulk material shows an SCO transition between 260 K and 300 K at ambient pressure [75]. Since XAS measurements of this compound are not reported in literature, such measurements are carried out here to obtain the spectral fingerprint of the two spin states. Figure 3.8 depicts the Fe-$L_{2,3}$ edges for a polycrystalline Fe(bppm)$_2$(BF$_4$)$_2$ sample, pressed into indium foil, at 283 K and 190 K. The Fe-L_3 edge at 283 K presents a double peak at 706.6 eV and 707.5 eV. Such a double structure was also found for Fe(phen)$_2$(NCS)$_2$ at room temperature (figure 3.1), implying a predominant HS state of Fe(bppm)$_2$(BF$_4$)$_2$. At 190 K the Fe-L_3 edge is mainly characterized by a single peak at 707.9 eV.

The influence of the rearrangement of the Fe 3*d* electrons on the electronic structure of the nitrogen ligands, can be probed by XAS at the N-*K* edge. Figure 3.9 shows the N-*K* XA spectra recorded at 283 K and 190 K. The spectra are composed of three sharp resonances at 400 eV, 402 eV, and 403.5 eV. The resonance at 400 eV, which can be associated with a π^* resonance, exhibits subtle changes of the corresponding fine structure upon the spin transition.

Experimentally, an *ex-situ* deposition of molecules sets high demands on the preparation procedure. In particular, a thorough rinsing of the sample surface after the deposition is necessary, in order to avoid additional molecules adsorbed on the SAM. Since the complex contains a divalent Fe ion, special care has to be taken in order to prevent oxidation of the Fe. Fe(II)(bppmc)$_2$(BF$_4$)$_2$ (bppmc=2,6-bis(1H-pyrazol-1-yl)pyridine-4-(N-(2-mercaptoethyl)carboxamide), shown in the inset of figure 3.11, was synthesized by Marco Haryono in the group of Prof. A. Grohmann [118].

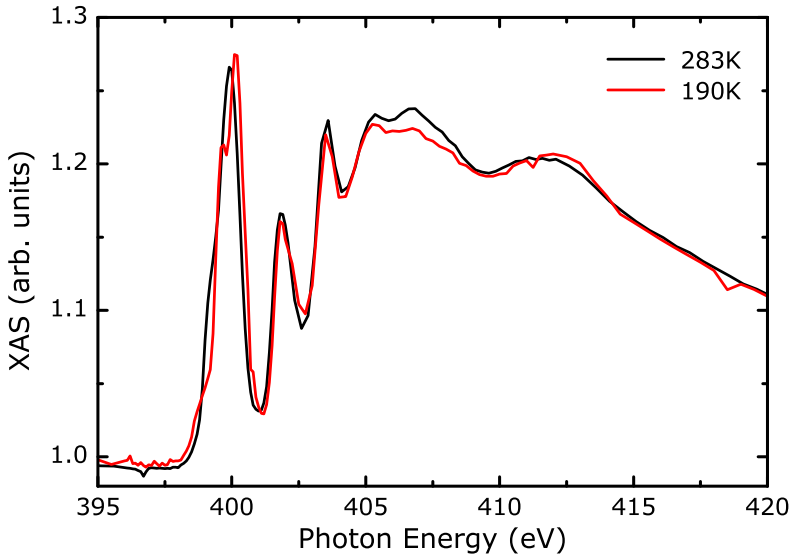

Figure 3.9: Temperature-dependent N-*K* XAS signal from bulk material of $Fe(bppm)_2(BF_4)_2$.

The complex was deposited from a 1 mmolar solution in acetonitrile onto 300 nm of gold on mica substrates.[2] The substrate was kept in the solution for 24 h. After the deposition, the sample was repeatedly rinsed with acetonitrile and ethanol. The whole preparation was carried out in a glove box in order to avoid oxidation of the Fe centers of the molecules. The preparation of the samples was carried out at the *Technische Universität Berlin*. Afterwards, the samples were transferred in N_2 atmosphere and directly mounted to the UHV chamber, prior the the X-ray measurements.

Figure 3.10 presents the S $2p$ XPS spectrum excited with a photon energy of 260 eV. The spectrum is dominated by an S $2p$ doublet, which can be identified as sulfur bound to Au with its well-known binding energy of the S $2p_{3/2}$ signal at 162 eV [119, 120]. The small contribution of sulfur displaying a binding energy of the S $2p_{3/2}$ signal of 161 eV (blue lines) can be associated with atomic sulfur, or sulfur linked to a highly coordinated Au site [121–123]. The signal at an S $2p_{3/2}$ binding energy of 163.7 eV (red lines) can be attributed to unbound thiol groups. This implies that both linker groups of the $Fe(bppmc)_2$ molecule bind to the surface, and virtually no additional layer of unbound complexes is adsorbed on top of the molecular layer.

Figure 3.11 details the Fe-$L_{2,3}$ XA signals of the SAM of $Fe(bppmc)_2$ at

[2]The substrates were purchased at Georg Albert PVD Beschichtungen GbR.

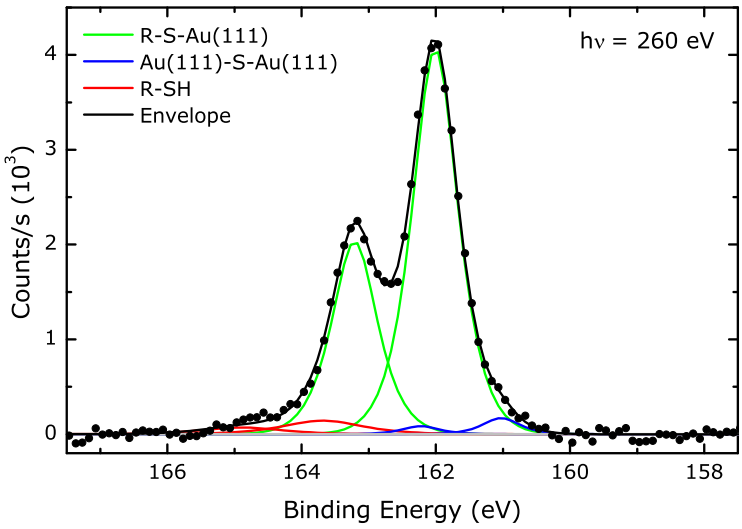

Figure 3.10: S 2*p* XPS spectra of the SAM of Fe(bppmc)$_2$ excited with 260 eV. The green line shows the fit for sulfur bound to gold. At the peak positions expected for atomic sulfur (blue) and unbound thiol groups (red) nearly no intensity is observed.

room temperature (black) and at 18 K (red). The Fe-L_3 intensity corresponds to an coverage in the range of 0.8 ML. The spectral shape of the Fe-L_3 edge is the same at 18 K and room temperature, excluding a change of the spin state. The comparison to a polycrystalline bulk sample of Fe(bppmc)$_2$(BF$_4$)$_2$ (gray), which presents a HS state, suggests that, the Fe(bppmc)$_2$ molecules in the SAM are also in a HS state. The XAS signal at 695 eV stems from the anions in the bulk sample and represents the F-*K* edge. No F-*K* XAS signal is found for the SAM of Fe(bppmc)$_2$, intimating that the anions are not present on the surface. The charge of the Fe center is likely to be compensated by an image charge on the gold surface, leading to the formation of a surface dipole.

In figure 3.12, the N-*K* XA spectra for the SAM of Fe(bppmc)$_2$ recorded at normal and grazing incidence angles are shown. No pronounced dependence on the incidence angle is observed for the intensities of the different resonances. This implies that the molecules are not adsorbed as suggested by the inset in figure 3.11, but with a tilted orientation of the molecular axis.

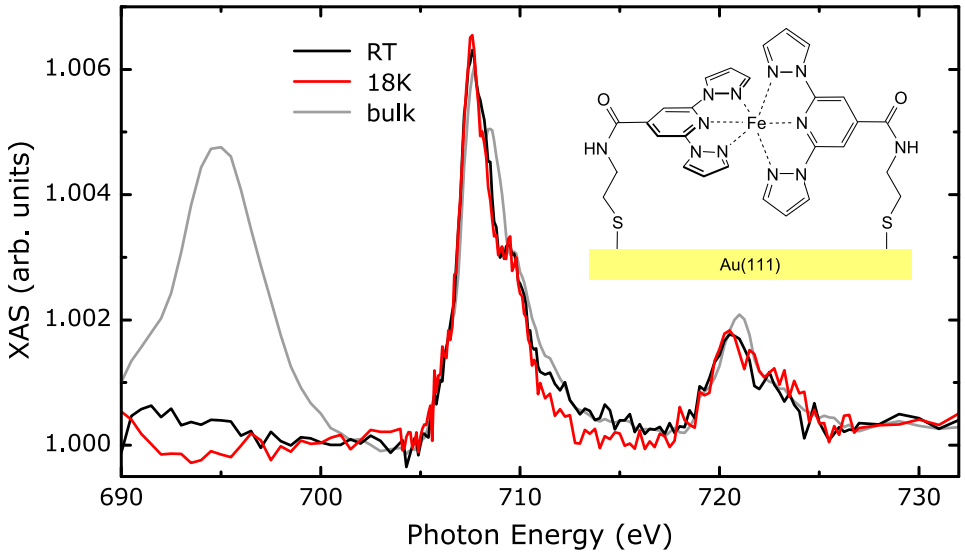

Figure 3.11: Temperature-dependent Fe-$L_{2,3}$ XAS signal of a SAM of Fe(bppmc)$_2$, measured at normal incidence. The gray line depicts the corresponding spectrum from bulk material of Fe(bppmc)$_2$(BF$_4$)$_2$ recorded at room temperature and scaled to match the same height. Inset: Structure formula of the complex.

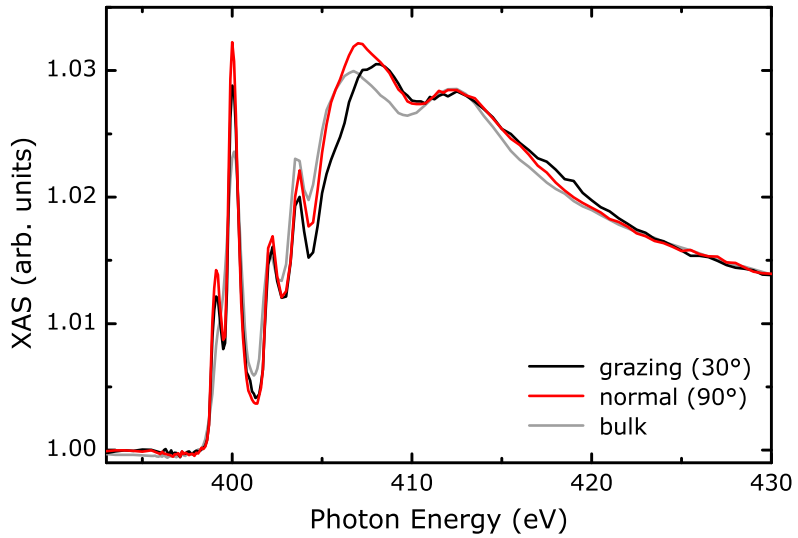

Figure 3.12: Angle-dependent N-*K* XAS signal of 1 ML of a SAM of Fe(bppmc)$_2$ and the corresponding isotropic spectrum of the bulk material (gray), scaled to about the same height.

4

Magnetic Ordering of Porphyrin Molecules

4.1 Introduction

Metalloporphyrins have attracted the attention of the scientific community for a very long time now. Initially, this interest originated from their biological significance and catalytic capabilities. Metalloporphyrins form the active centers of many biochemical molecules like chlorophyll, hemoglobin, and cytochrome. Together with phthalocyanines, porphyrins belong to the group of quasi-planar complexes. These complexes frequently display extraordinarily high stability, owing to the tetradentate nature of the ligand and their conjugated macrocycle. The reason for their biological importance lies in their unsaturated coordination sites, allowing for an interaction with additional ligands. From the chemical point of view, porphyrins are a versatile platform for synthesis, since their properties can be widely tuned by the variation of their functional groups or exchange of the metal center. While the functional groups mainly determine the interaction of the molecules with each other or with other molecules, the metal center defines the electronic and magnetic properties.

The investigation of porphyrin and phthalocyanine molecules on surfaces in the monolayer and submonolayer regime is a fast-growing field of scientific research. Numerous scanning tunneling microscopy (STM) works

have studied the lateral ordering of various porphyrins and phthalocyanines [124–128]. In recent works more functional aspects have been addressed. Gao *et al.* have reported the formation of molecular rotors by Zn phthalocyanine molecules anchored to Au adatoms on Au(111) [129]. Grill *et al.* have used prophyrins with Br-containing functional groups to form molecular wires by covalent binding of the molecules [130]. Flechtner *et al.* demonstrated that the interaction of Co porphyrins to Ag(111) substrates can be reversibly switched *via* coordination of NO towards the metal center. The *in-situ* metalation of porphyrins on surfaces by separate evaporation of the free-base porphyrin molecule and the metal atoms has been reported for various metallic centers, *e.g.*, Co, Fe, Zn, and Ce [13, 131–134]. However, the magnetic properties of porphyrin and phthalocyanine molecules on surfaces have rarely been investigated. Scheybal *et al.* reported the induced magnetic ordering of Mn porphyrin molecules on a Co substrate [15]. Iacovita *et al.* have used spin-polarized STM to visualize the spin-dependent transport through Co phthalocyanine molecules adsorbed on Co nanoislands on Cu(111) [16]. Nevertheless, the research on monomolecular layers of magnetic molecules on surfaces is subject to rapid progress. Gambardella *et al.* showed that the magnetic anisotropy of Fe coordinated in a network of benzenedicarboxylic acid on Cu(100) can be switched from in- to out-of-plane upon the adsorption of O_2 [8]. Recently, Mannini *et al.* succeeded in measuring the magnetic hysteresis of surface-mounted single molecular magnets containing 4 Fe centers [7].

In this chapter, measurements of the electronic structure and the magnetic properties of Fe and Co porphyrin molecules on non-magnetic and FM substrates are presented. On both kinds of substrates, an additional modification of the chemical properties of the molecules is achieved by placing a layer of atomic oxygen between the molecules and the respective surfaces. Angle-dependent measurements are carried out by XAS, providing element-specificity and magnetic sensitivity by means of XMCD. Firstly, XAS measurements of the bulk material of Fe and Co porphyrin molecules with different functional groups are presented in section 4.2. Since the electronic and magnetic properties of the bulk materials are known from literature, these spectra serve as a reference for the interpretation of the spectra obtained from the porphyrin molecules when adsorbed onto surfaces. Measurements of submonolayers of Fe and Co OEP molecules adsorbed onto non-magnetic Cu(100) and O/Cu(100) substrates are described in section 4.3 and 4.4. Angle-dependent measurements of the magnetic properties were

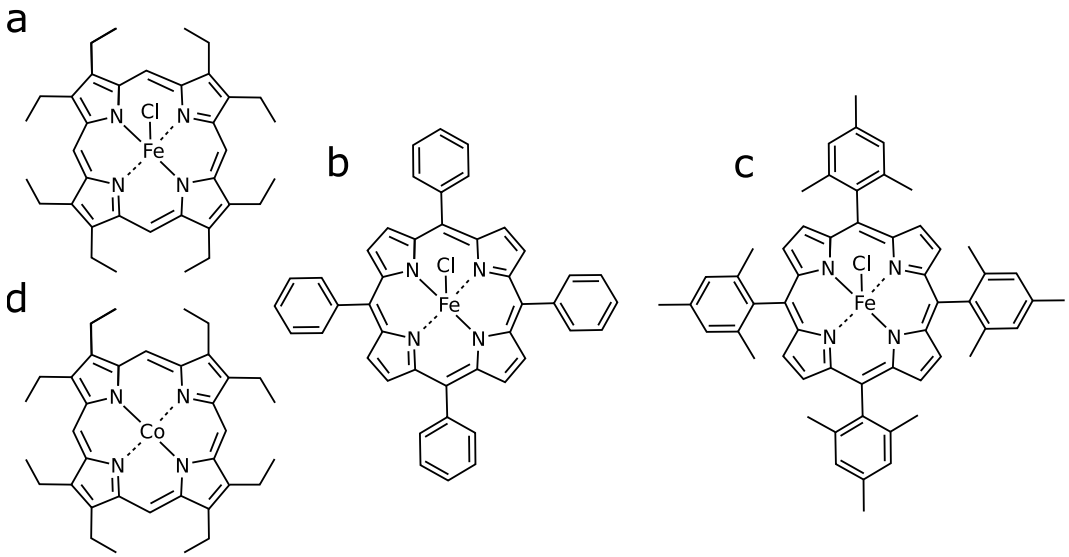

Figure 4.1: Structural formulae of (a) 2,3,7,8,12,13,17,18-octaethylporphyrin Fe(III) chloride (Fe OEP Cl), (b) meso-tetraphenylporphyrin Fe(III) chloride (Fe TPP Cl), (c) 5,10,15,20-tetrakis(2,4,6-trimethylphenyl)porphyrin Fe(III) chloride (Fe TtMP Cl), and (d) 2,3,7,8,12,13,17,18-octaethylporphyrin Co(II) (Co OEP).

carried out using an external magnetic field of $B = 5$ T at $T = 8$ K to align the magnetic moment of the metal center. Section 4.5 deals with the induced magnetic ordering of Fe OEP molecules on FM Ni and Co thin films on Cu(100). A model is developed to determine the magnetic coupling energy from the temperature dependence of the Fe and substrate magnetizations, as is presented in section 4.6. Finally, tailoring of the magnetic coupling is achieved by placing atomic oxygen between the molecules and the FM substrates. As a result, the molecule and substrate magnetic moments are aligned antiparallel. The coupling energies and the magnetic moments, obtained from a sum-rule analysis, of both ferro- and antiferromagnetically coupled Fe porphyrin molecules are discussed in section 4.7.

4.2 X-ray Absorption Measurements of Porphyrin Bulk-Samples

In this section, XA measurements are presented of polycrystalline samples from porphyrin molecules which contain different metallic cen-

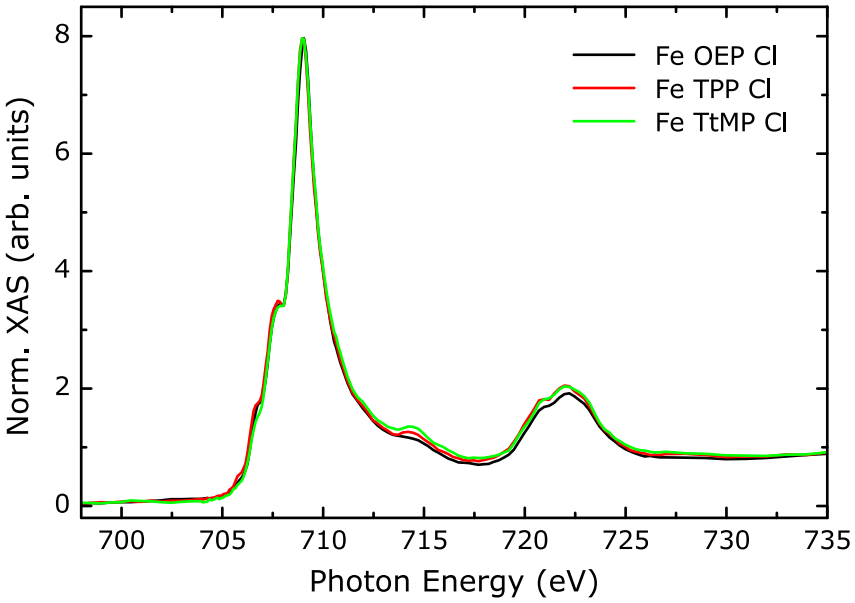

Figure 4.2: Isotropic XA spectra at the Fe-$L_{2,3}$ edges obtained from the bulk material of three different Fe porphyrin molecules.

ters and functional groups. The measurements serve as fingerprints for the electronic structure of the molecules that will be compared to the corresponding spectra when such molecules are deposited onto surfaces. Three Fe porphyrins with increasing size are investigated: 2,3,7,8,12,13,17,18-octaethylporphyrin Fe(III) chloride (Fe OEP Cl), meso-tetraphenylporphyrin Fe(III) chloride (Fe TPP Cl), and 5,10,15,20-tetrakis(2,4,6-trimethylphenyl)porphyrin Fe(III) chloride (Fe TtMP Cl). In addition, 2,3,7,8,12,13,17,18-octaethylporphyrin Co(II) (Co OEP) is studied. The structural formulae of these molecules are given in figure 4.1. In general, the central part of porphyrins is basically planar and the metallic center is situated in the ligand field constituted by the four nitrogen atoms. For the investigated Fe porphyrins a chlorine ion is added as a fifth ligand to obtain a stable 3^+ oxidation state on the Fe site. This results in a conformation where the Fe ion is pulled out of the nitrogen ligand plane. For Fe TPP Cl and Fe TtMP Cl, the phenyl groups bind in meso-positions *via* single bonds. Although single bonds allow for rotation around their axes, such movement is hindered by steric interactions of the hydrogen atoms and the methyl groups in the case of Fe TPP Cl and Fe TtMP Cl, respectively. However, if the molecules are deposited on a surface these interactions might be overruled by the molecule–substrate interaction [127, 135, 136].

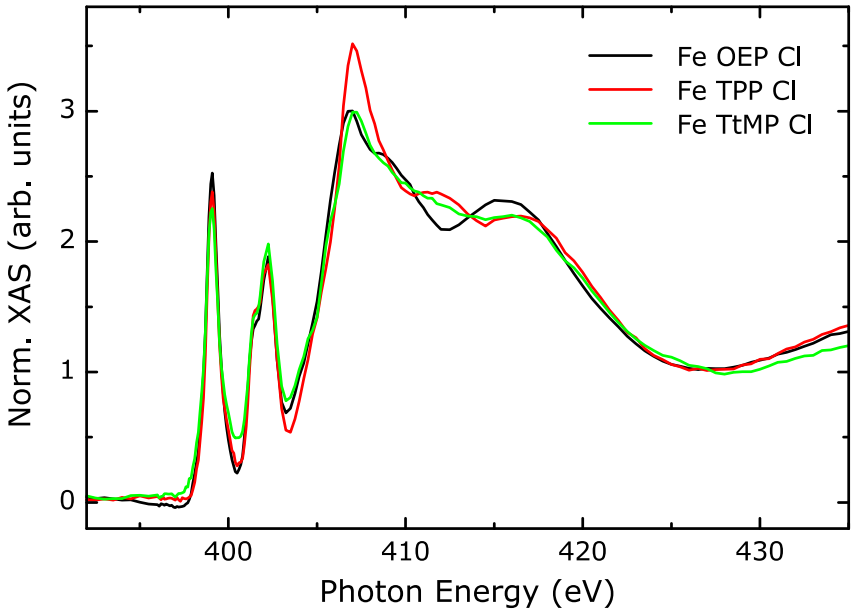

Figure 4.3: Isotropic XA spectra at the N-*K* edge obtained from the bulk material of three different Fe porphyrin molecules.

Figure 4.2 shows the Fe-$L_{2,3}$ edges of Fe OEP Cl, Fe TPP Cl, and Fe TtMP Cl. The Fe ions of the porphyrin complexes display a HS state, with electronic configuration $(d_{xy})^1(d_\pi)^2(d_{z^2})^1(d_{x^2\text{-}y^2})^1$ [137]. The three Fe spectra exhibit almost identical shapes, reflecting the identical structure of the central part of the individual molecules, due to the localized character of the X-ray absorption technique. The $L_{2,3}$ edges exhibit fine structure due to multiplet splitting commonly found for transition metal ions in a ligand field. At 714.5 eV, small differences between the spectra of the individual molecules are visible.

In figure 4.3 the N-*K* edges of the three porphyrins molecules are shown. These spectra reflect the electronic structure at the nitrogen sites. At a first glance the four N atoms constituting the ligand field of the iron center occupy equivalent sites. However, if the porphyrin molecule exhibits buckling, subtle differences in the position and, consequently, the electronic structure between two pairs of N atoms may arise. Although the transition matrix element of an $s \rightarrow p$ transition is strongly orientation-sensitive for each molecule, the obtained spectrum is isotropic due to the polycrystalline nature of the sample. The spectra are characterized by three sharp π^* resonances at 399.1 eV, 401.5 eV, and 402.2 eV. Above 406 eV, broad σ^* resonances are found originating from the antibonding orbital of the σ bond

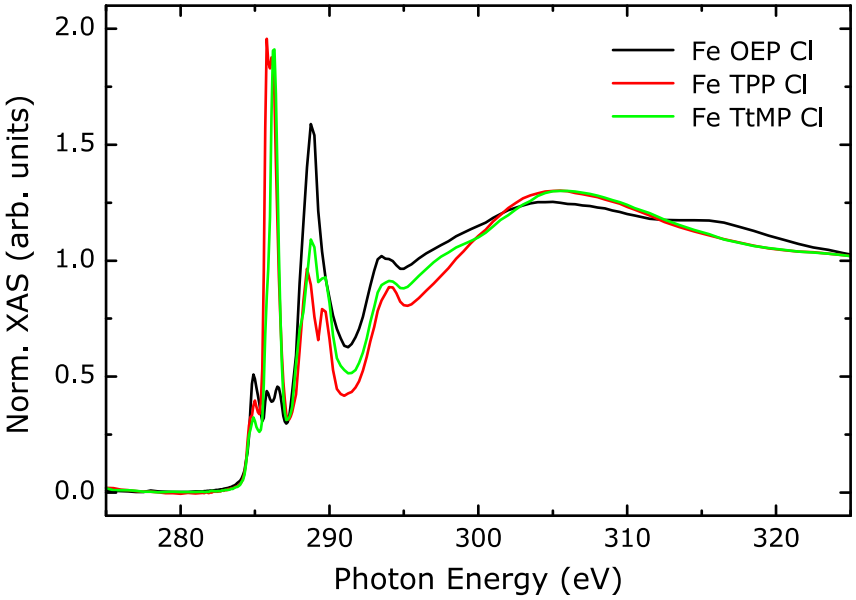

Figure 4.4: Isotropic XA spectra at the C-*K* edge obtained from the bulk material of three different Fe porphyrin molecules.

to the adjacent atoms.

The C-*K* edge reflects the difference of the individual porphyrins, since they mainly differ in their functional groups which are ethyl, phenyl, and 2,4,6-trimethylphenyl, respectively. Figure 4.4 shows the corresponding XA spectra of the Fe porphyrin molecules. Although each molecule consists of many different C atoms, the spectra show well-separated features, since there exist groups of C atoms with similar properties. Furthermore, transitions to the same molecular orbital might be excited from different C sites, due to the conjugated nature of the molecule. Five main π^* resonances are found arranged in two groups. The three lower energy resonances at 284.9 eV, 285.8 eV, and 286.3 eV can be regarded as fingerprints for the functional groups. For Fe OEP Cl, these resonances show the lowest intensity as can be expected for ethyl groups since their C atoms only form single bonds. For Fe TPP Cl, the resonances at 285.8 eV and 286.3 eV exhibit significant intensity that can be ascribed to transitions into the π^* orbital of the conjugated phenyl groups. For Fe TtMP Cl, only the resonance at 286.3 eV shows intensity due to the presence of the three methyl groups bond to each phenyl ring. The resonances at 288.5 eV and 289.6 eV can be assigned to transitions into the molecular orbitals of the porphyrin macrocycle, since they are also present for Fe OEP Cl, whose functional groups does not possess π bonds.

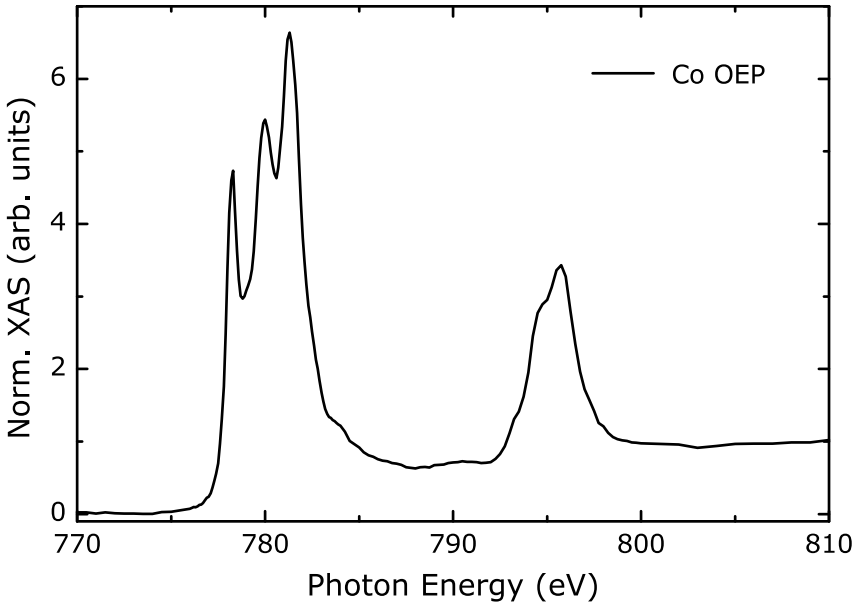

Figure 4.5: Isotropic XA spectra at the Co-$L_{2,3}$ edges of a Co OEP bulk sample.

Above 296 eV, broad σ^* resonances are found. Due to the higher number of C atoms and the broad nature of these resonances, an assignment is not possible without simulations of the XA spectra by means of density functional theory (DFT) calculations [103, 104].

Figure 4.5 shows the Co-$L_{2,3}$ edges of Co OEP. The Co-L_3 is composed of widely separated, sharp peaks, typically found for Co^{2+} ions [101, 138, 139]. In contrast to the Fe ion in the Fe porphyrins, shown in figure 4.2, the Co ion presents a low-spin state, with electronic configuration $(d_{xy})^2(d_\pi)^4(d_{z^2})^1$ [36, 137]. The absence of an anion leads to a fully planar arrangement of the Co ion in the plane of the four nitrogen ligands.

In figures 4.6 and 4.7 the XA spectra at the N- and C-K edges of Co OEP are compared to those of Fe OEP Cl. Despite the strong difference in the arrangement of the d electrons of the metal center, only smaller differences in the spectral shape are observed. The pre-peak in the N-K spectra of Co OEP at 397.5 eV is an artifact of the measurement, and can be attributed to the Co-L_2 edge excited with the second order of the monochromator (*cf.* section 2.3).

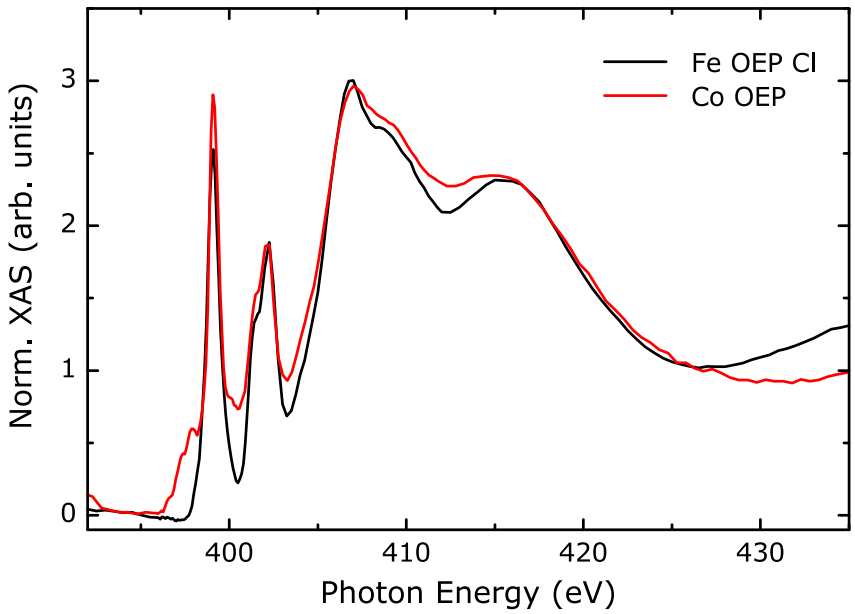

Figure 4.6: Comparison of the XA spectra at the N-*K* edge of Fe OEP Cl and Co OEP bulk samples.

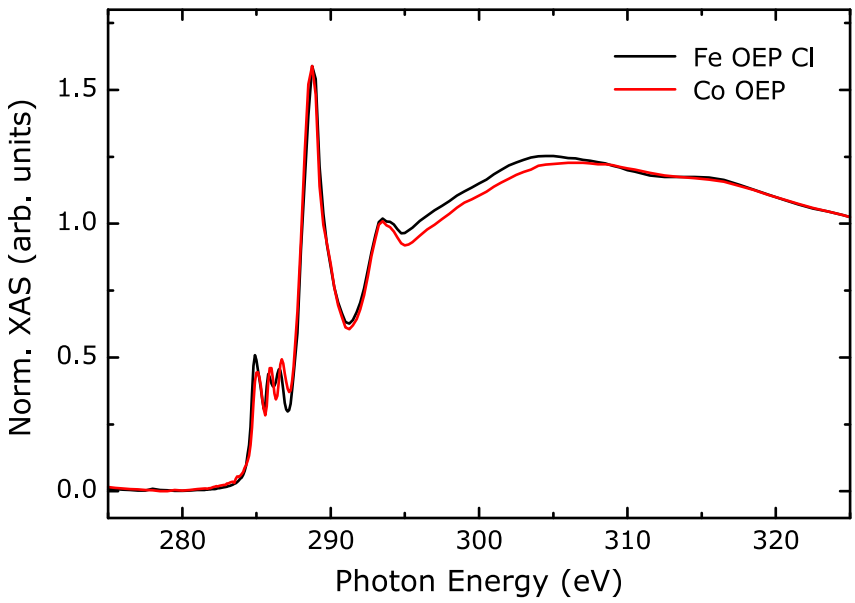

Figure 4.7: Comparison of the XA spectra at the C-*K* edge of Fe OEP Cl and Co OEP bulk samples.

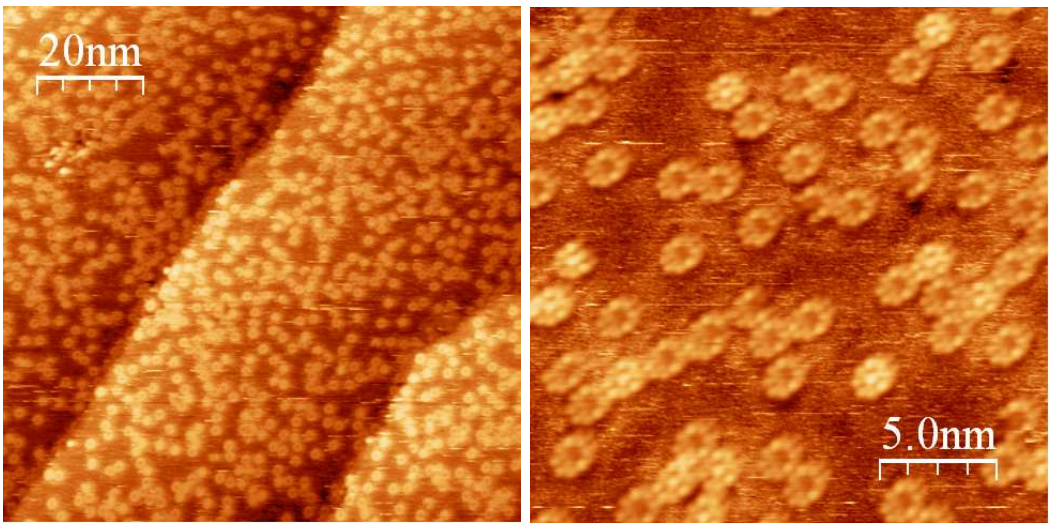

Figure 4.8: STM images of Fe OEP on Cu(100) at room temperature (left panel: 1.3 V, 0.08 nA; right panel: 1.2 V, 0.17 nA).

4.3 Adsorption of Fe Porphyrins on Cu(100) Surfaces

When going from bulk condition to surfaces, the molecules are arranged in two instead of three dimensions. On the surface, molecules frequently display a preferential orientation. In this section, STM measurements of Fe OEP molecules adsorbed onto a Cu(100) single crystal are presented. From this measurements the adsorption geometry of the molecules is deduced. The sample is prepared by evaporation of Fe OEP Cl from a Knudsen cell at 485 K (*cf.* section 2.1) onto the substrate held at room temperature.

Figure 4.8 shows two images of Fe OEP on Cu(100) at room temperature. These were taken with an Omicron variable-temperature scanning tunneling microscope at the beamline ID08 at ESRF. In the right-hand image, the intramolecular structure of the porphyrin molecules is resolved. It is directly evident that the Fe porphyrin molecules adsorb flat on Cu(100). The left-hand image provides an overview on the distribution of the molecules. It can be seen that they show a tendency to decorate the steps of the Cu(100) surface. Their mobility is quite low since they do not agglomerate and hardly change their position between successive images. The coverage of the molecular layer can be determined by the ratio of area with and without molecules. A coverage of (0.38$\pm$0.04) monomolecular layers is deduced

from the evaluation of several images. From successive XA measurements of the same sample a peak height of 2.1% of the Fe-L_3 edge with respect to the Cu background is determined. These values provide the basis for the calibration of the coverage in the submonolayer regime, used throughout the thesis.

The eight ethyl groups of the individual molecules can be clearly distinguished in the right image. Most of the molecules appear highly symmetric, indicating that although the ethyl groups can rotate around their single bonds they favor one particular orientation. For molecules that do not exhibit this symmetric appearance, some of their ethyl groups might possess different orientations. Furthermore, the image evidences the existence of two species of Fe porphyrin molecules: one that shows a bright center and another presenting no intensity in the center of the molecule. The ratio between these two species is approximately 1 : 3.

There are several possible explanations for such an appearance. One might tend to assign the bright center to the chlorine ligand: a molecule with a dark center would then just be a molecule with chlorine between the molecule and the surface. However, with this reasoning, the observed ratio of 1 : 3 cannot be explained, since the statistical nature of the adsorption process would result in a ratio of 1 : 1, *i.e.*, for half of the molecules the chlorine ligand faces vacuum and for the other half the surface. The three times higher number of molecules with dark centers would imply that for half of the molecules the chlorine ligand decouples from the Fe center upon evaporation of the molecules or adsorption on the surface[1]. In both cases it is likely that the chlorine ion binds to copper atoms of the surface. Although, no Cl XAS signal is found at the $L_{1,2,3}$ edges, a Cl $2p$ signal could be detected with XPS.

Another explanation could be that the molecules with a dark center do not contain a metal ion at all. The purity of the molecular powder, obtained from Porphyrin Systems GbR, was nominally 98%. However, such non-complexed porphyrins are a typical contamination and might be enriched by the sublimation process. By means of low-temperature STM on this system, it was shown that both molecules with and without bright center dis-

[1] Due to the uncertainty concerning the presence of the chlorine ligand, I will refer to Fe octaethylporphyrins adsorbed on the surface as Fe OEP. However, the valance state of the Fe ion is also influenced by the interaction between the molecules and the surface and will be addressed in section 4.7.

play a Kondo resonance [140]. Thus, a magnetic center has to be present in both cases. In addition, the resulting effective Fe coverage of approximately 5‰ of a monolayer would have made it almost impossible to obtain a signal-to-noise ratio of 50 : 1 (in a 5 minute measurement) as presented in figure 4.9. Finally, the observed effect can be explained by different adsorption geometries that may result in an Fe position close or further away from the surface. However, a substantiated explanation cannot be given here but involves a systematic study by means of STM.

4.4 X-Ray Natural Linear Dichroism and Angle-Dependent X-Ray Magnetic Circular Dichroism of Paramagnetic Octaethylporphyrin Molecules

In this section, our investigations are presented regarding the electronic structure and the magnetic properties of oriented OEP molecules adsorbed onto bare and oxygen-covered Cu(100) single crystals. Angle-dependent measurements were carried out to study the anisotropy of charge and spin densities of the individual electronic levels of the metal center.

Figure 4.9 shows the Fe-$L_{2,3}$ edges of 0.4 ML of Fe OEP molecules adsorbed onto a Cu(100) single crystal. The spectra are measured at room temperature using linearly polarized X rays. The localized arrangement of the Fe 3*d* electrons in the electrostatic field of the porphyrin ligands is reflected in the fine structure most clearly seen at the L_3 edge. The splitting of the *d* electrons can be partly resolved within the resolution of the monochromator which was set to 200 meV. The individual resonances that constitute the absorption edge show distinct angle-dependent behavior when varying the incidence angle of the X rays by rotating the sample. At normal incidence, the $\vec{E}$ vector of the X rays probes the unoccupied charge density, *i.e.*, the hole density, in the surface plane of the sample according to equation 1.7. At grazing incidence, the $\vec{E}$ vector has a component perpendicular to the sample surface, probing the corresponding hole density. At 20° incidence angle, *i.e.*, 70° between the $\vec{E}$ vector and the surface, the component perpendicular to the sample plane is dominant. However, a fully perpendicularly aligned $\vec{E}$ vector cannot be realized since this corresponds to a measurement

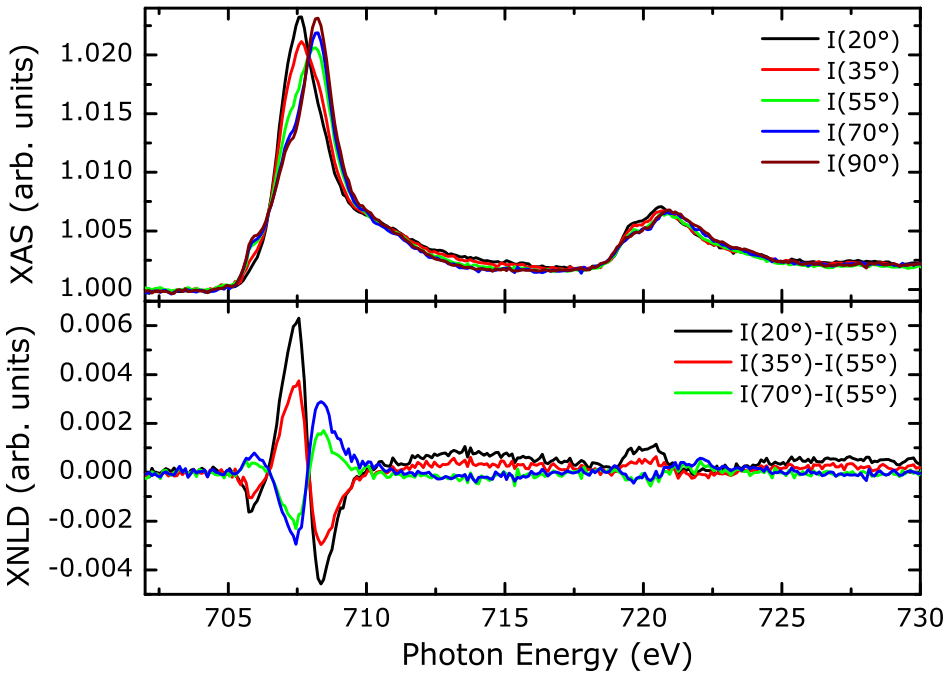

Figure 4.9: Angle-dependent XA spectra at the Fe-$L_{2,3}$ edges of 0.4 ML of Fe OEP on Cu(100) using linearly polarized X rays (upper panel). The lower panel shows the difference between the spectra and the one measured at 55°.

geometry with the X rays parallel to the sample surface. It is important to note that XAS does not probe the hole density in the direction of the $\vec{E}$ vector but its projection onto the x, y, and z axes. Thus, the spectra shown in figure 4.9 for different incidence angles are not independent, but undergo a gradual transition from an XA spectrum probing the hole density in the z direction to a one probing the hole density in the x-y plane. At 54.7°, *i.e.*, the magic angle for linear light, the in-plane and out-of-plane components of the $\vec{E}$ vector contribute equally to the resulting spectra. Such a spectra is equivalent to an isotropic spectra, which can be obtained by averaging over spectra along x, y, and z directions or a spectra of randomly oriented molecules as in the case of the polycrystalline bulk sample presented in section 4.2.

In the lower panel of figure 4.9, the difference between the Fe-$L_{2,3}$ spectra and the spectrum recorded at the magic angle is shown. It is obvious that all spectra display the same shape, differing only in magnitude and sign. Three main angle-dependent resonances are visible. The middle resonance

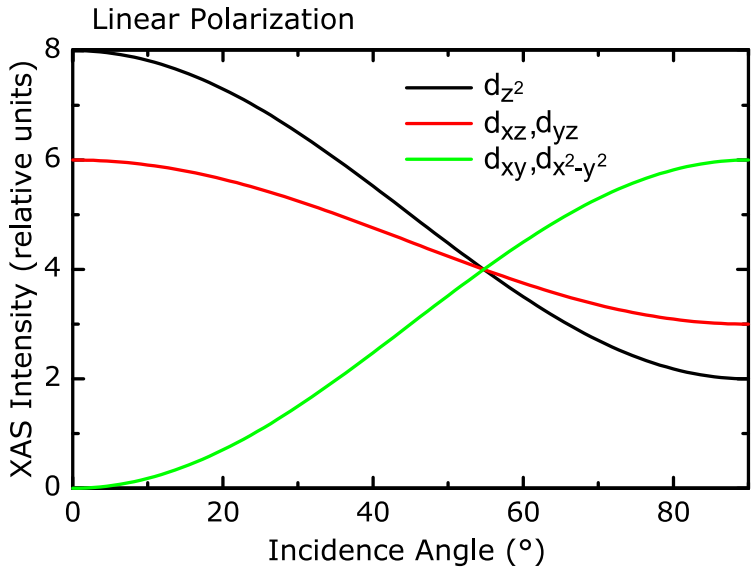

Figure 4.10: Expected angular dependence of relative XAS resonance intensity for the individual *d* orbitals with the quantization axis perpendicular to the sample surface when probed with linearly polarized X rays.

at 707.5 eV shows maximum intensity for 20° incidence angle corresponding to an out-of-plane hole density, whereas the pre-peak at 705.9 eV and the resonances at 708.4 eV display maximum intensity at normal incidence. The pre-peak seems to vanish when the $\vec{E}$ vector is approaching a perpendicular alignment to the surface, as is apparent in the upper panel.

Although the fine structure of the absorption edges arises due to multiplet splitting of the individual multi-electron 3*d* orbitals and is also subject to core-hole interaction, it is useful to consider this angular dependence in reference to the angular dependence of the individual 3*d* one-electron orbitals [18, 19]. This model can be applied because each basis set of atomic orbitals can be expressed as a linear combination of the one-electron 3*d* orbitals, keeping in mind that a resonance might have contributions from more than one orbital, and that one orbital might contribute to more than one resonance.

Figure 4.10 shows the expected angle-dependent evolution of the intensity of the individual *d* orbitals, according to table 1.2, assuming the quantization axis *z* with respect to the ligand field is perpendicular to the sample surface and that *x* and *y* axes are equivalent. These assumptions are fulfilled for the given case of flatly adsorbed porphyrin molecules exhibiting a lig-

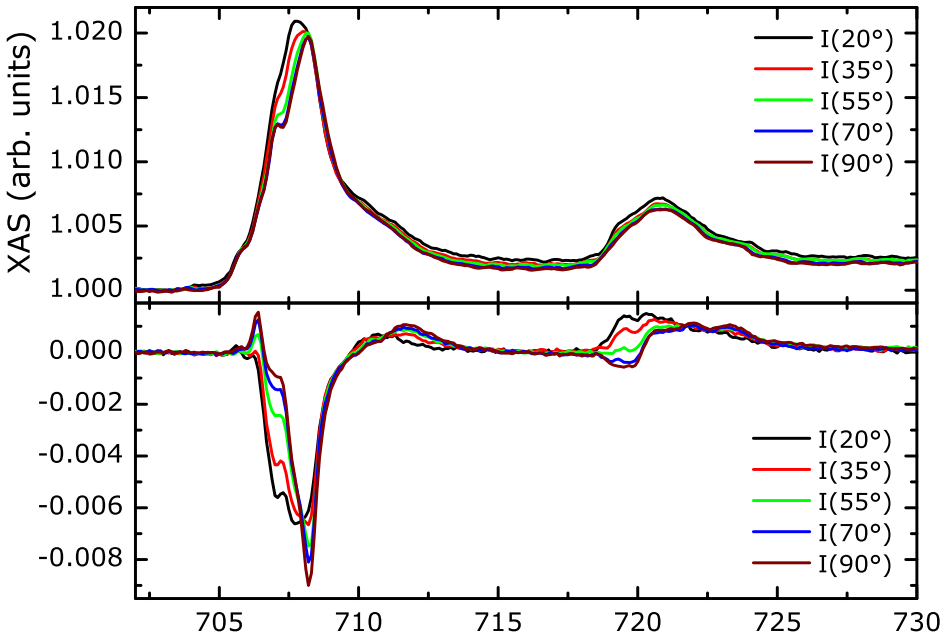

Figure 4.11: XAS (upper panel) and XMCD (lower panel) signals at the Fe-$L_{2,3}$ edges of 0.4 ML of Fe OEP on Cu(100) for incidence angles from 20° to 90° and the magnetic field aligned along the $\vec{k}$ vector of the X rays.

and field with tetragonal symmetry. Within this symmetry, the d_{xz} and d_{yz} orbitals are degenerate, forming the d_π orbital[2]. The angular dependence arises from the asymmetric charge distribution of the d orbitals and the inequivalency of the z axis with respect to the x and y axes. The latter can be illustrated, for example, by the d_{xz} orbital, behaving equivalently to the x and z directions but still possessing an angular dependence, since both x and y in-plane directions have to be averaged. The two in-plane d_{xy} and $d_{x^2\text{-}y^2}$ orbitals demonstrate the same dependence on the incidence angle, displaying maximum intensity for normal incidence. The d_{z^2} orbital exhibits the opposite behavior of the intensity, having the same amplitude but not vanishing for an $\vec{E}$ vector in-plane. As a consequence, the resonances seen at 708.4 eV in figure 4.9 can be ascribed to mainly d_{xy} and $d_{x^2\text{-}y^2}$ character, whereas the resonance at 707.5 eV possess d_{z^2} and d_π characteristics.

Besides their electronic properties, the magnetic properties of the

[2] Since all other d orbitals display the same intensity for $\vec{E}||\vec{x}$ and $\vec{E}||\vec{y}$, the x and y axes are equivalent independent of an preferred azimuthal orientation of the molecules.

molecules are also of interest. In order to investigate them, we employ the XMCD effect, based on the difference in absorption of left and right circularly polarized X rays, as discussed in section 1.4. Since the molecules are paramagnetic, we have to measure at low temperatures and apply a high magnetic field.

Figure 4.11 shows the Fe-$L_{2,3}$ edges for different X-ray incidence angles measured at a temperature of $T = 8$ K in an applied magnetic field of $B = 5$ T along the X-ray incidence directions. The upper panel shows the helicity-averaged spectra using left and right circularly polarized X rays. The lower panel shows the difference between the two helicities, *i.e.,* the XMCD spectra. Analogous to the spectra recorded with linearly polarized light (figure 4.9), the helicity-averaged spectra are sensitive to the unoccupied density of states. However, the angle-dependent variation is reduced, since one component of the $\vec{E}$ vector is always oriented along the surface plane, independent of the incidence angle. The full magnetic information is contained in the XMCD spectra, probing the unoccupied spin density at the Fe site.

A sizable XMCD signal is found for all measured incidence angles, evidencing the presence of an Fe magnetic moment. Four resonances can be identified in the XMCD and XAS signals, best visible for normal incidence. In contrast to the charge density, the spin density and so the XMCD signal scales with the magnetization of the molecules. Since the applied magnetic field and the temperature were not sufficient to magnetically saturate the molecules, their magnetization might change when varying the direction of the magnetic field due to a magnetic anisotropy of the Fe center.

The expected angle-dependent variation of the resonance intensities for the individual d orbitals is presented in figure 4.12 in reference to both the XAS (left panel) and XMCD (right panel) signals, according to table 1.3. In addition to the assumptions stated earlier, a magnetic field parallel to the X-ray $\vec{k}$-vector is assumed for the XMCD intensity differences. Furthermore, complete saturation of the magnetization along the field direction and no anisotropy of the spin and orbital moment are also assumed. The utilization of circularly polarized X rays results in a reduced angular contrast of the XAS intensity compared to figure 4.10. The XMCD contrast, however, is very high. The magic angle at which an isotropic spectrum is obtained is

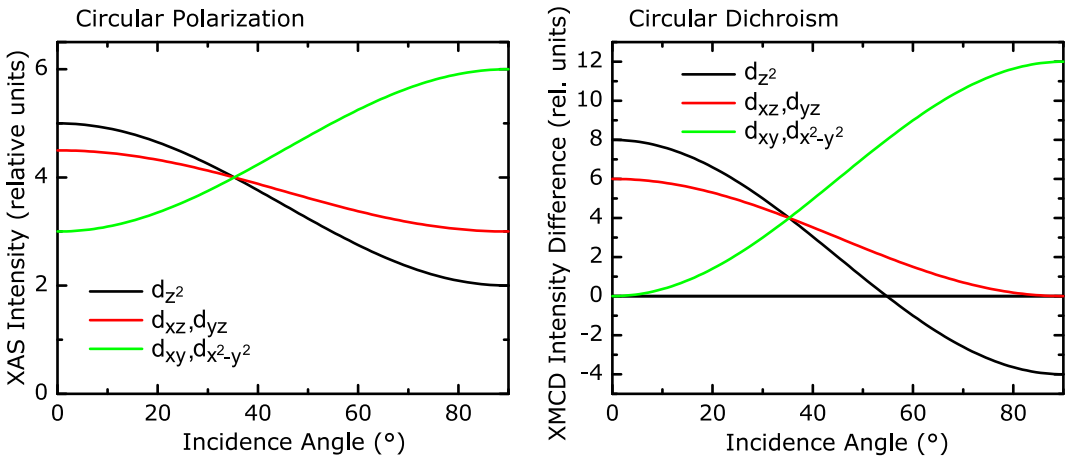

Figure 4.12: Expected XAS (left panel) and XMCD (right panel) signals against incidence angle for the individual d orbitals with the quantization axis perpendicular to the sample surface using circularly polarized X rays and the magnetic field aligned along their $\vec{k}$ vector.

now found at 35.3° incidence angle.[3] The angular dependence of the XMCD signal of the d orbitals shows interesting differences to the one of XAS. For small incidence angles, the behavior is similar to the XAS case: the in-plane d_{xy} and $d_{x^2-y^2}$ orbitals display zero dichroism, whereas the other orbitals show maximum dichroism. At normal incidence, the d_π orbital has zero dichroism. This means that even if the spin of this orbital is fully aligned, it will yield no XMCD signal. The XMCD signal of the d_{z^2} orbital even changes its sign at normal incidence. It is important to note that this is not in contradiction to the sum rules, that state that the integrated XMCD signal at the magic angle is proportionate to the magnetic moment of the d shell (section 1.4.1). The partly drastic deviations for the individual orbitals reflect the impact of the magnetic dipole operator T_α, *i.e.*, the anisotropy of the spin density. Since the spin magnetic moment is an isotropic quantity, the extra information from the spin-density is often bothersome. This is mainly because an isotropic XMCD is generally not easy to obtain, since it involves aligning the magnetic moment with the direction of the magic angle, or to average over three orthogonal measurements. Luckily the experimental set-

[3] In literature the magic angle is usually defined as 54.7° for both linear and circular polarization. For linear polarization, the angle is defined between the $\vec{E}$ vector and the surface normal, whereas for circular polarization it is defined between the $\vec{k}$ vector and the surface normal. This is taken into account here when referring solely to the incidence angle.

up provides the possibility to align the magnetic moment accordingly.

The strong angle-dependent variation of the XMCD facilitates the identification of the contributions of the individual d orbitals to the spectrum. The pre-peak at 706.3 eV, displaying opposite XMCD contrast at normal incidence, has to be of d_{z^2} character. The peak at 707.1 eV, which constitutes the middle of the XA spectra shown in figure 4.9 must be of d_π character, since it nearly vanishes in the XMCD signal at normal incidence and reappears at a 20° angle. At higher energies, the spectra are mainly of d_{xy} or $d_{x^2\text{-}y^2}$ character.

Since it was not possible to magnetically saturate the molecules, the spin and orbital magnetic moment cannot be determined from a sum-rule analysis of the obtained spectra. However, it is still possible to determine lower limits for these moments. For this purpose, the spin and orbital sum rules are evaluated for the spectra recorded at the magic angle (35.3° incidence angle) for which the contribution of the magnetic dipole operator to the spin sum rule cancels out. The number of d holes, given by the the oxidation state of the Fe centers, enters as an input parameter according to equations 1.11 and 1.12. On the surface the Fe valence state might be altered due to charge transfer processes. The charge density at the Fe site is reflected by the Fe-L_3 peak position, which can be used as a sensitive indicator of the oxidation state [40]. The L_3 peak position of Fe OEP on Cu(100) is red-shifted by about 1 eV with respect to the one of the Fe(III) OEP Cl bulk sample, shown in figure 4.2. This indicates that the oxidation state of the Fe center on the surface is reduced. If we assume an Fe 2^+ oxidation state we obtain four d holes $n_h = 4$. For the spin and orbital moment, a lower limit of $\mu_S > (1.01 \pm 0.15)\mu_B$ and $\mu_L^\alpha > (0.13 \pm 0.03)\mu_B$ is obtained, respectively. The ratio of orbital-to-spin moment $\mu_L^\alpha/\mu_S = (13 \pm 3)\%$ holds, even though the molecules were not magnetically saturated. The errors reflect the uncertainties concerning the experimental data, *e.g.*, the choice of the integration range for the L_3 and L_2 edges or the potential impact of small bendings in the spectra. By comparing the integrated XMCD signal at different angles, information about the magnetic anisotropy of the iron center can be obtained. But such evaluation is hampered by the angle-dependent contribution of T_α, which cannot easily be separated if the magnetic anisotropy is small.

In a subsequent experiment, we deposited Fe OEP molecules onto a pre-oxidized Cu(100) single crystal, which was prepared as described in

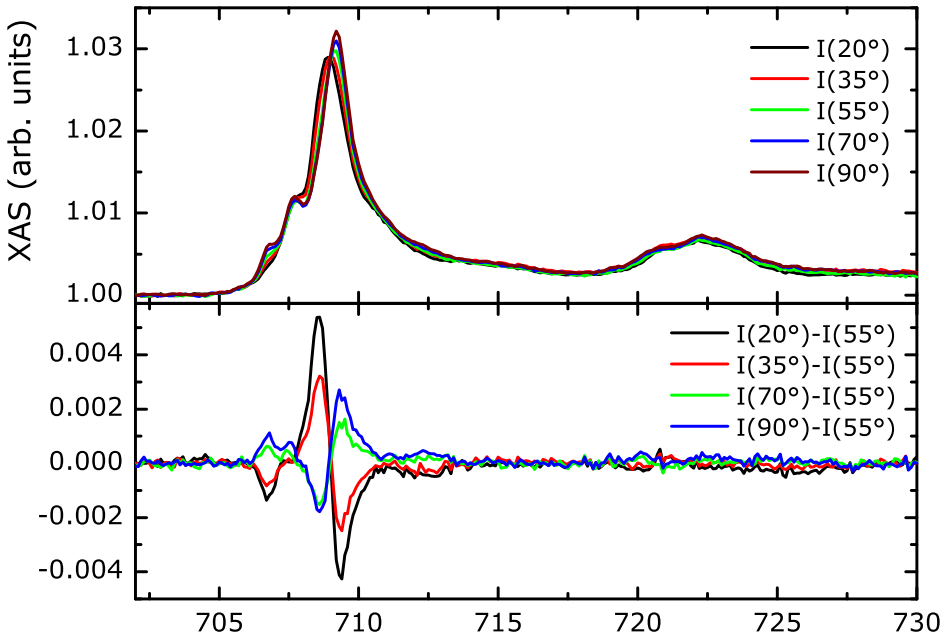

Figure 4.13: Upper panel: Angle-dependent XA spectra at the Fe-$L_{2,3}$ edges of 0.4 ML of Fe OEP on O/Cu(100) using linearly polarized X rays. Lower panel: Difference between the spectra and the one measured at 55°.

section 2.4. The surface is covered by half a monolayer of atomic oxygen forming a well-known $(\sqrt{2} \times 2\sqrt{2})$R45°, so-called missing row, reconstruction. We deposited 0.4 ML of Fe OEP molecules, after cooling the crystal down to room temperature.

In the upper panel of figure 4.13 the XA spectra at the Fe-$L_{2,3}$ edges are shown for incidence angles from 20° to 90°, using linearly polarized X rays. The lower panel depicts the difference between the corresponding spectra and the one obtained at the magic angle (54.7° incidence angle). Compared to the case of the bare Cu(100) substrate (*cf.* figure 4.9), the variation of the Fe spectra with the incidence angle is reduced. This means that the charge densities of the individual electronic levels of the Fe 3*d* electrons is more isotropic. A fully isotropic charge density is expected, in cubic symmetry, where the d_{xy}, d_{xz}, and d_{yz} (e_g) and the $d_{x^2\text{-}y^2}$, and d_{z^2} (t_{2g}) form degenerate subsets, each of isotropic charge density. In tetragonal symmetry, the d_{z^2} orbital is lowered in energy, due to the absence of the two ligands that mainly interact with its extended lobes along the z axis, and the charge distribution

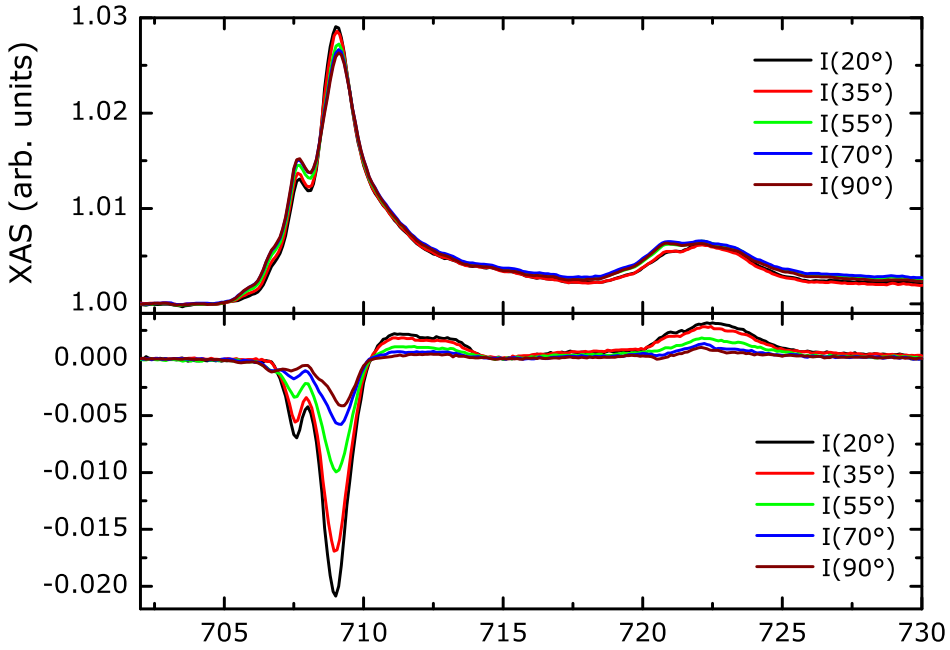

Figure 4.14: XAS (upper panel) and XMCD (lower panel) signals at the Fe-$L_{2,3}$ edges of 0.4 ML of Fe OEP on O/Cu(100) for incidence angles from 20° to 90° and the magnetic field aligned along the $\vec{k}$ vector of the X rays.

of the electronic states becomes anisotropic. If the d_{z^2} orbital is pushed up in energy due to the interaction with the atomic oxygen on the surface, the isotropic charge distribution can be partly restored.

Besides their smaller magnitude, the difference spectra in figure 4.13 are composed mainly of three resonances at the L_3 edge. Two resonances at 706.7 eV and 709.4 eV correspond to in-plane hole densities of d_{xy} and $d_{x^2\text{-}y^2}$ character, and one resonance at 708.6 eV of d_π or d_{z^2} character.

Figure 4.14 shows the Fe-$L_{2,3}$ XAS and XMCD signals which were measured at different X-ray incidence angles and at a temperature of $T = 8$ K in an applied magnetic field of $B = 5$ T along the X-ray incidence directions. The most prominent effect is a 5-fold decrease of the XMCD signal when comparing the spectrum at normal incidence to the one at 20°. This decrease can only be explained by the presence of a strong magnetic anisotropy, with the easy axis of the Fe magnetic moment oriented in-plane, as a result of an interaction of the iron centers and the oxygen atoms.

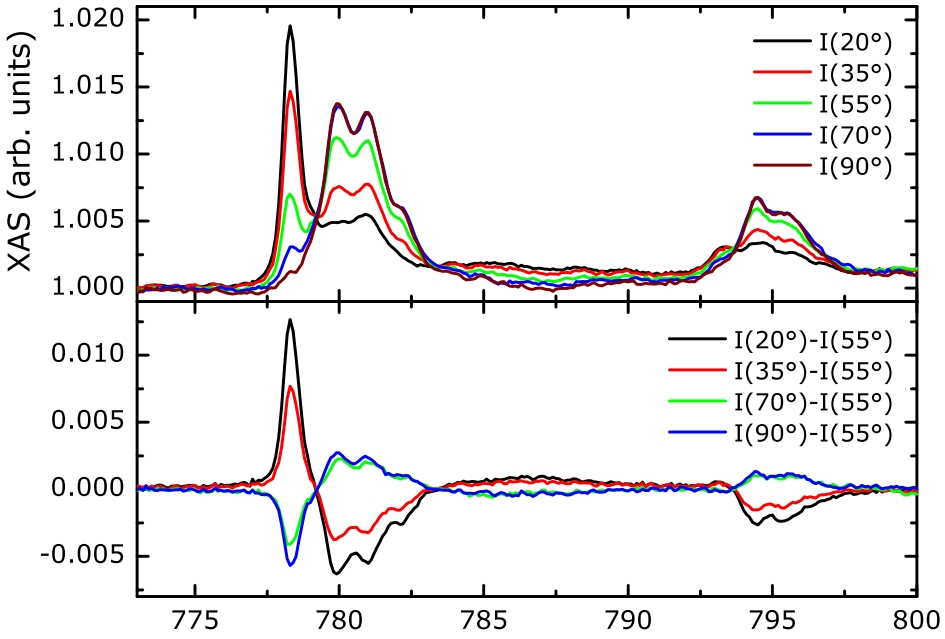

Figure 4.15: Upper panel: Angle-dependent XA spectra at the Co-$L_{2,3}$ edges of 0.4 ML of Co OEP on O/Cu(100) using linearly polarized X rays. Lower panel: Difference between the spectra and the one measured at 55°.

Since the shape of the XMCD spectra hardly changes with the incidence angle, one can conclude that the magnetic dipole operator has only minor contributions to the magnetic signal. Consequently, a lower limit for the spin and orbital moments can be deduced from a sum-rule analysis of the spectra taken at 20° X-ray incidence. For Fe OEP on O/Cu(100), the Fe-L_3 peak position coincides within 0.2 eV with that of the Fe(III) OEP Cl bulk sample, suggesting an Fe 3^+ oxidation state. This corresponds to five d holes $n_h = 5$. Values of $\mu_S > (2.70 \pm 0.32)\mu_B$ and $\mu_L^\alpha > (0.23 \pm 0.06)\mu_B$ are found for the lower limit of the spin and orbital moment per d hole, respectively. The ratio of orbital-to-spin moments is found to be $\mu_L^\alpha/\mu_S = (8 \pm 2)\%$, slightly lower as in the case of Fe OEP directly adsorbed onto Cu(100). The ratio slightly increases with an increasing incidence angles, but these changes are within the error. No pre-peak showing opposite dichroism is observed, consistent with the d_{z^2} orbital being moved up in energy.

A study of Fe OEP on Cu(100), O/Cu(100), and Au(111) with coverages in the regime of 1 ML and 2 ML can be found in reference [141].

In another experiment, we have deposited Co OEP molecules onto an O/Cu(100) substrate, prepared as described above. Figure 4.15 depicts the XAS signal at the Co-$L_{2,3}$ edges when the X-ray incidence angles are systematically varied. These spectra show pronounced angular dependence most visible in the difference spectra shown in the lower panel of figure 4.15. The low-energy resonance at 778.3 eV reflects an out-of-plane hole density. The three resonances at 779.9 eV, 781.0 eV, and 782.1 eV display the opposite angle-dependent behavior, which can be associated with in-plane hole density. This can be readily understood considering an Co^{2+} LS state, with electronic configuration $(d_{xy})^2(d_\pi)^4(d_{z^2})^1$, as it is also found for the bulk material and suggested by the shape of the XA spectra [101, 138, 139]. The out-of-plane hole density can then be ascribed to the singly occupied d_{z^2} orbital, whereas the in-plane hole density can be attributed to the fully unoccupied $d_{x^2\text{-}y^2}$ orbital. A comparison with the measurements of the Co OEP bulk sample, shown in figure 4.5, can be done for the spectrum recorded at the magic angle (54.7° incidence angle). This spectrum resembles the shape of the Co-L_3 edge of the Co OEP bulk sample displaying a slight broadening of the individual resonances, which can be ascribed to the electronic coupling of the Co ion and the substrate.

In figure 4.16 the magnetic measurements at $T = 8$ K and $B = 5$ T are presented for five different incidence angles. Consistent with the supposed LS configuration, the observed XMCD signal is very small. Astonishingly the XMCD signal for normal incidence predominantly presents an positive (negative) signal at the L_3 (L_2) edge. This suggests a strong contribution of the d_{z^2} orbital to the XMCD, since it is the only one that shows a reversal of the sign of its dichroism with varying incidence angles. An alternative explanation assuming a Co magnetic moment aligned antiparallel to the magnetic field is hard to imagine. The comparable high weight of the L_2 edge contribution suggests a high orbital moment. The evaluation of the sum rules for the spectra at the magic angle (35.3°) with $n_h = 3$, yields lower limits of the spin and orbital moment of $\mu_S > (0.28 \pm 0.04)\mu_B$ and $\mu_L^\alpha > (0.13 \pm 0.04)\mu_B$, respectively. An ratio of the orbital-to-spin moment of $\mu_L^\alpha/\mu_S = (46 \pm 14)\%$ is determined.

Experiments of Co OEP directly adsorbed onto Cu(100) revealed that the Co porphyrin was in a highly reactive state, making it difficult to measure since cooling down the sample already resulted in a sizable change of the Co-L_3 line shape, due to the adsorption of residual gas on the sample at

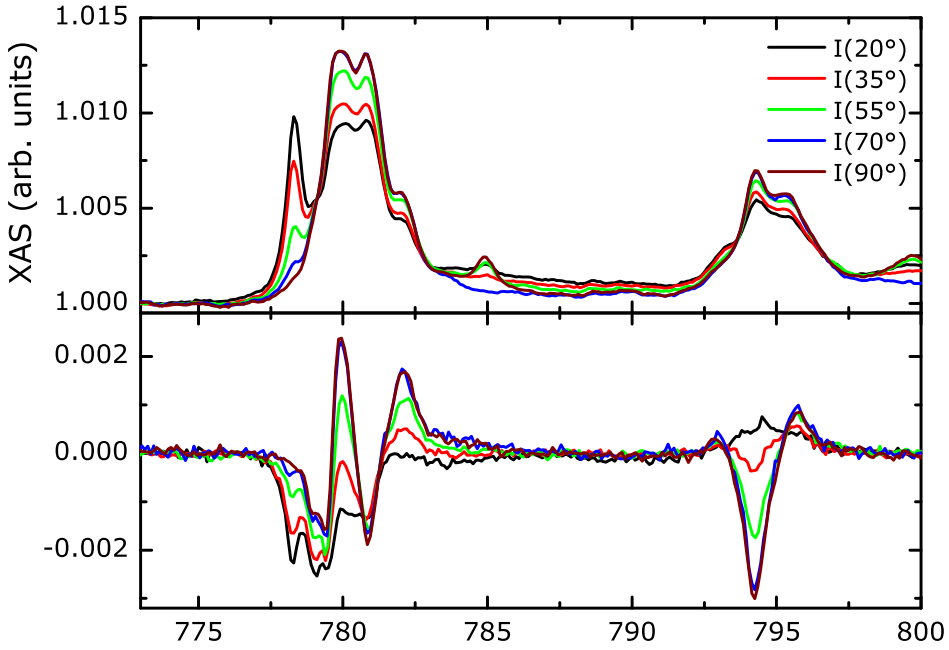

Figure 4.16: XAS (upper panel) and XMCD (lower panel) signals at the Co-$L_{2,3}$ edges of 0.4 ML of Co OEP on O/Cu(100) for incidence angles from 20° to 90° and the magnetic field align along the $\vec{k}$ vector of the X rays.

lower temperatures.

4.5 Substrate-Induced Magnetic Ordering

In the previous section it was shown that the magnetic moment of porphyrin molecules can be partly aligned by an external magnetic field at low temperatures. In view of future applications of porphyrin molecules on surfaces, it would be desirable to obtain an magnetic alignment at room temperature and without the need for a strong external magnet field. A strategy to achieve such alignment is to employ the exchange interaction to an FM substrate. In this section, systematic XAS and XMCD measurements of the electronic structure and the magnetism of Fe OEP molecules on Ni and Co substrates are presented.

Figure 4.17 shows the XAS and XMCD spectra at the Fe-$L_{2,3}$ edges of 1 ML Fe OEP on 5 ML Co/Cu(100) and 15 ML Ni/Cu(100) at room tem-

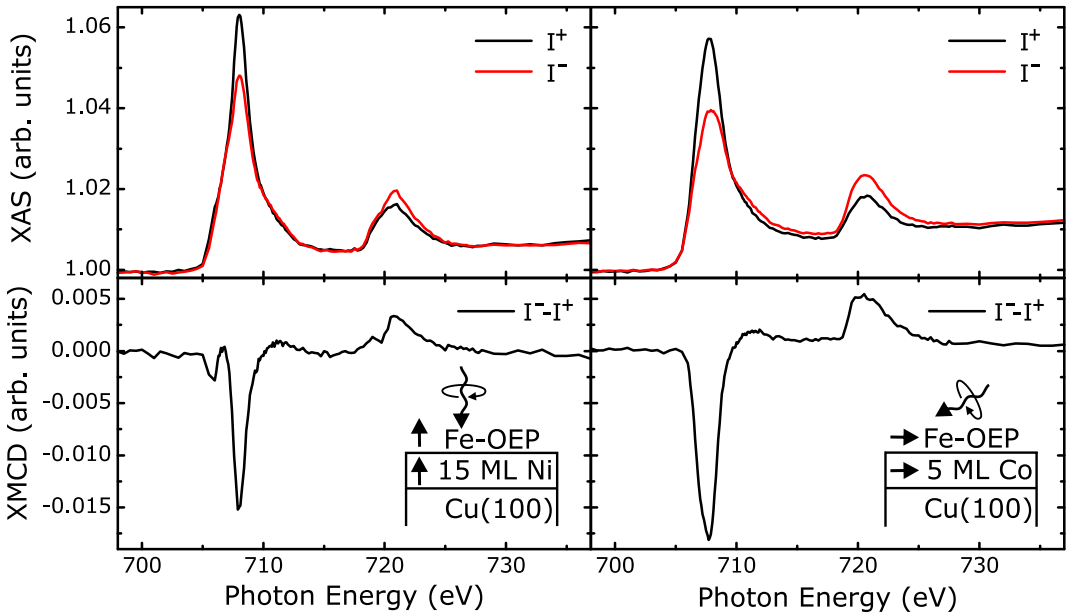

Figure 4.17: XAS and XMCD at the Fe-$L_{2,3}$ edges of 1 ML Fe OEP on out-of-plane magnetized 15 ML Ni/Cu(100) (left) and in-plane magnetized 5 ML Co/Cu(100) (right), using left and right circularly polarized X rays (top, black and red).

perature, in an applied magnetic field of 10 mT. By using these thicknesses of the FM films, the easy axis of magnetization can be tuned from in-plane (Co, [110] direction), to out-of-plane (Ni). The applied magnetic field is 50 times smaller than it was for the measurements discussed in the previous section. It will not affect the magnetic moments of the molecules at room temperature but only align the magnetization of the FM film. The measurements were carried out at normal ($\theta = 90°$) and at grazing ($\theta = 20°$) incidence, accordingly. The presence of an XMCD signal reveals that the Fe OEP molecules are magnetically aligned on both substrates. The sign of the Fe XMCD signals is the same as that for the Ni and Co layers, which demonstrates that the coupling of the molecules to the films is FM. This can be seen even more clearly from the element-specific hysteresis loops presented in figure 4.18 for Fe OEP on Ni, recorded at room temperature. The Fe- and Ni-L_3 XMCD signals at fixed photon energy, normalized to their saturation values are plotted as a function of the applied magnet field. It is clear that the two hysteresis loops coincide in coercive fields. Hence, the orientation of the Fe spin switches in the same way as the spins of the ferromagnetic film. This demonstrates the presence of a substantial FM coupling of the Fe

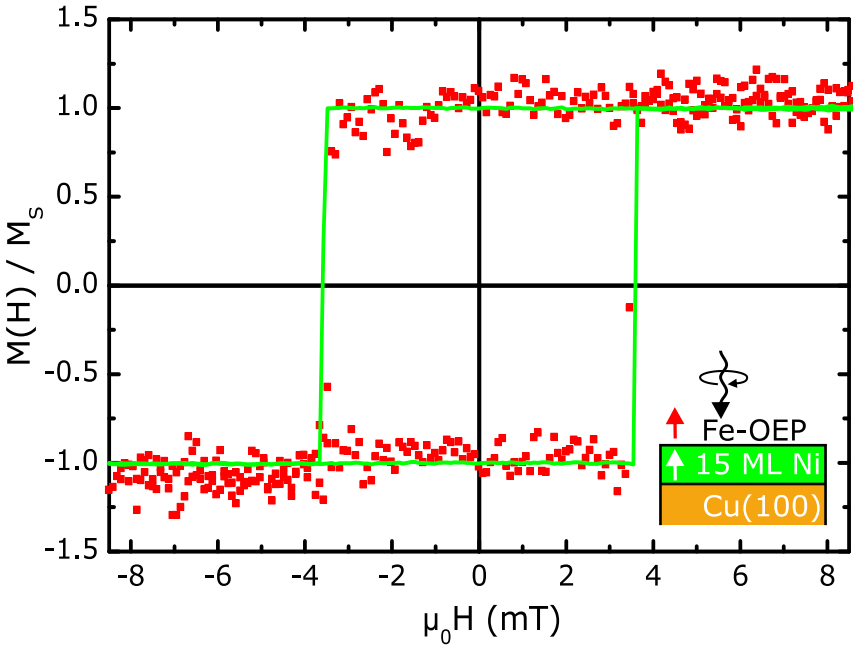

Figure 4.18: Element-specific hysteresis loops of the Fe atoms (squares) and Ni substrate (full line), obtained from the L_3 edge XMCD maxima of Fe OEP on Ni/Cu(100) at 300 K.

moments to the magnetic substrate.

The origin of the magnetic ordering is discussed in our recent work [142]. By performing *ab-initio* DFT+*U* calculations for an Fe porphin[4] molecule adsorbed on a Co substrate, it has been shown that the ordering is not due to a direct exchange interaction between the Fe centers of the molecules and the Co atoms of the substrate. Instead, a 90°-ferromagnetic superexchange interaction through the N ligands is found to be responsible for the coupling.

As discussed in section 4.4, the line shape of the XAS and XMCD spectra presented in figure 4.17 varies with the incidence angle, reflecting the anisotropy of charge and spin densities of the individual electronic levels. For Fe OEP adsorbed on Ni, the Fe-L_3 XMCD signal is composed of two well-separated, negative peaks at 705.8 eV and 708.0 eV. This shape is different compared to the XMCD spectra at 90° incidence angle of Fe OEP on Cu(100), aligned by an external field (figure 4.11). In that case, a pre-peak of

[4] Porphyrin molecule without functional groups, resulting in a lower computational effort.

opposite sign compared to the main XMCD peak was found. Consequently, the magnetic alignment induced by the two mechanisms acts differently on the individual 3*d* electronic levels. Differences in the electronic structure of the Fe center between Fe OEP adsorbed on Ni and on Cu substrates could be evoked as an alternative explanation. At 706.7 eV no dichroism is observed, whereas a sizable XAS signal is detected. Such a signature would be expected for a transition to the d_π orbital (*cf.* figure 4.12) or to a fully empty Fe 3*d* orbital. Since both spin-up and spin-down states would be unoccupied, no net XMCD signal can be observed. In contrast, the Fe-L_3 XMCD signal for Fe OEP adsorbed on Co recorded at 20° incidence angle displays a rather broad metallic-like line shape. This behavior is similar to the one of Fe OEP on Cu(100) (figure 4.11), where the Fe-L_3 XMCD signal at 20° incidence angle is much broader than the one at 90°.

In contrast to chemically inert substrates, like Au(111), porphyrin molecules might not be free to arrange themselves when deposited onto Co or Ni due to a stronger interaction with the substrate. When approaching a nominal coverage of one monomolecular layer, a heterogeneous adsorption of the molecules might result. Let us assume a random distribution of molecules adsorbing on the surface. If the molecules cannot move on the surface, a heterogeneous adsorption will occur once the space between the molecules on the surface is smaller than the area one molecule occupies. In view of our experiment, this would apparently lower the magnetic moments determined by a sum-rule analysis, since a fraction of the molecules would not be coupled to the magnetic substrate. To investigate this issue, XAS and XMCD measurements were performed for both Ni and Co substrates as a function of the coverage of the molecular layer.

The orientation of the molecules on the surface is investigated by coverage-dependent XAS measurements at the N-*K* edge. Figure 4.19 shows the N-*K* XAS spectra of Fe OEP layers with coverages corresponding to 0.4 ML, 0.6 ML, 1.0 ML, and 1.5 ML on Co (top) and on Ni (bottom) substrates, measured at 20° (grazing) and 90° (normal) incidence angles with linearly polarized X rays. The spectra are recorded from a consecutive deposition series. The XA spectra are normalized to the background signal in the pre-edge region stressing the thickness dependence of the XAS signals. A pronounced angular dependence of the N *K* XAS signals is observed, most clearly seen at the two π^* resonances at 399.0 eV and 401.2 eV. The angular dependence corresponds to an out-of-plane orientation of the N π^* orbitals

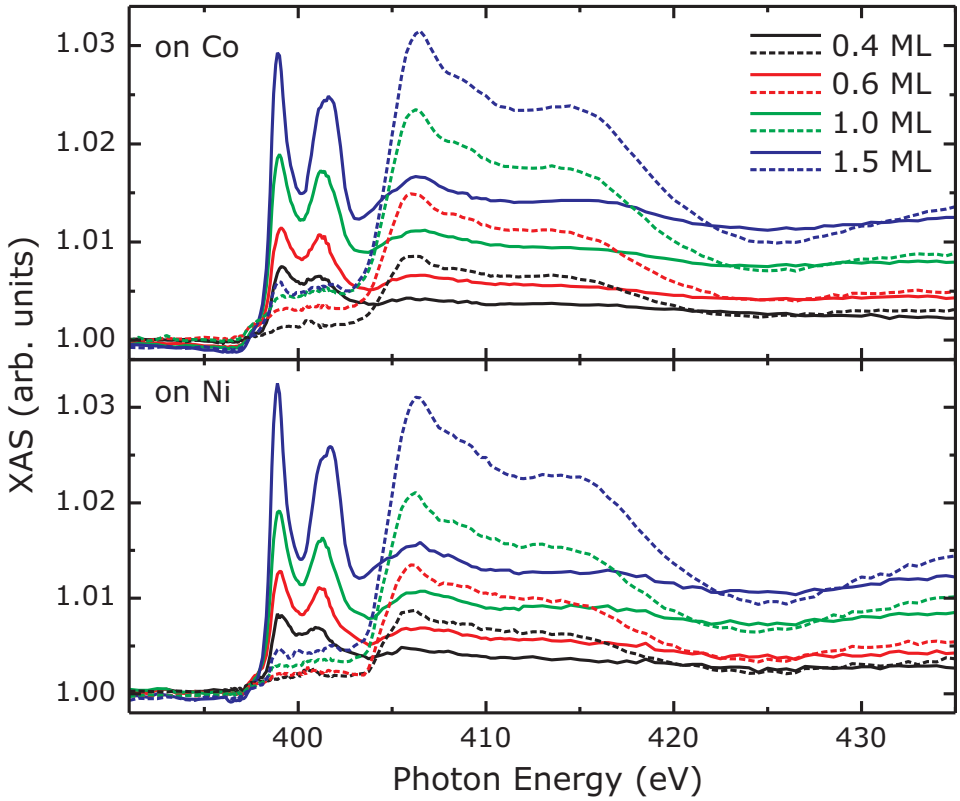

Figure 4.19: N-*K* XA spectra recorded at grazing (20°, solid lines) and normal (90°, dashed lines) incidence angles for different coverages of Fe porphyrin molecules on 5 ML Co/Cu(100) (upper panel) and on 15 ML Ni/Cu(100) (lower panel) at room temperature using linearly polarized X rays.

corresponding to a flat adsorption of the porphyrin macrocycle. The angular dependence is preserved also at higher coverages indicating that the second layer of porphyrin molecules adsorbs basically flat on the first layer. It is important to note that the shape of the spectral features at 399.0 eV and 401.2 eV is not the same for grazing and normal incidence. This implies that the intensity found for normal incidence does not belong to the same molecular orbital than the one for grazing. This can be understood considering that due to the interaction of the nitrogen atoms with the surface new orbitals are formed by hybridization of the N π orbitals with orbitals of the surface. Such strong interaction of the nitrogen atoms with the surface was found by DFT+*U* calculations mentioned earlier. Since the orientation of this newly formed bond is basically perpendicular to the surface, the angular dependence of the corresponding resonance is opposite to the one of the

N π^* orbitals. Therefore a quantitative analysis of the average tilt angle of the molecules according to equation 1.6 cannot be carried out.

The N-*K* edge is a sensitive indicator of whether the deposited molecules are intact. The N-*K* edge spectra exhibit similar fine structures than that observed for the bulk material of Fe OEP Cl, shown in figure 4.3. If the central 3*d* atom is missing, a third peak is expected at about 403.0 eV [143]. The absence of this feature indicates that the Fe atom is located in the molecule.

Figure 4.20 shows, from top to bottom, the helicity-averaged Fe-$L_{2,3}$ XAS and XMCD spectra of Fe OEP layers with coverages corresponding to 0.4 ML, 0.6 ML, 1.0 ML, and 1.5 ML on Co (panels a, b) and on Ni (panels c, d) magnetically saturated substrates. The spectra are measured at room temperature from the same deposition series as the N-*K* XA spectra. Again, the spectra are normalized to the pre-edge region to stress the thickness dependence of the white lines. Due to the in-plane and out-of-plane magnetic easy axes for Co and Ni, the respective spectra were measured at 20° (grazing) and 90° (normal) incidence angles, respectively, as indicated by the insets in panels b and d. The insets in panel a and c show the Fe-L_3 difference signal between two consecutive depositions. In that way, the XAS signal of the molecules that are adsorbed on top is separated from that of the previously deposited molecules.

In the case of the Co substrate, the Fe-$L_{2,3}$ white lines are relatively broad, resembling the analogous spectra for bulk metallic materials. For thicknesses smaller or of the order of 1 ML, the intensities increase with the coverage and no different lineshapes are observed. On the contrary, the L_3 signal for 1.5 ML displays a broader feature. The XAS difference spectrum between the spectrum for 1.5 ML and 1 ML shows two well-separated peaks at 706.7 eV and 708.4 eV that can by attributed to the Fe-L_3 XAS signal of the molecules in the second monolayer. The change of the lineshape can be explained by the different ligand fields around the Fe atom present in the first molecular layer, in direct contact to the substrate, and in the second layer. In the latter, only weaker intermolecular interactions can be envisaged on the bottom side of the molecule, while the top side faces vacuum. It is noteworthy that the shape of the Fe-L_3 XAS signal is different compared to those of the Fe OEP Cl bulk sample, shown in figure 4.2. This indicates that the electronic state of the Fe centers is not the one displayed in the bulk material. The XMCD signals, again, show a quasi-metallic shape. Up to

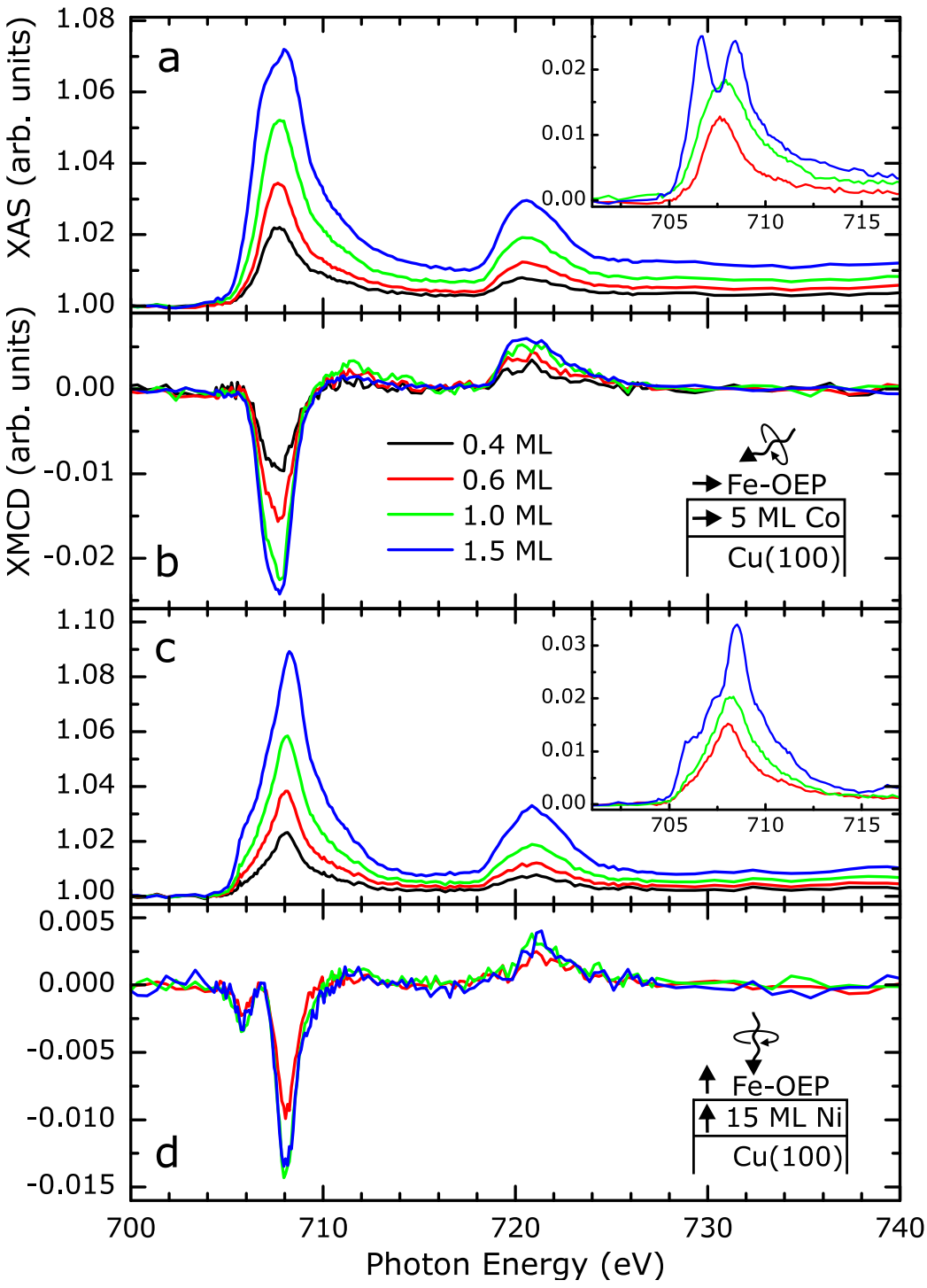

Figure 4.20: Fe-$L_{2,3}$ XAS and XMCD spectra recorded at room temperature for different coverages of Fe OEP on 5 ML Co/Cu(100) (a, b) and on 15 ML Ni/Cu(100) (c, d). The insets show the XAS difference at the L_3 edge between two successive depositions.

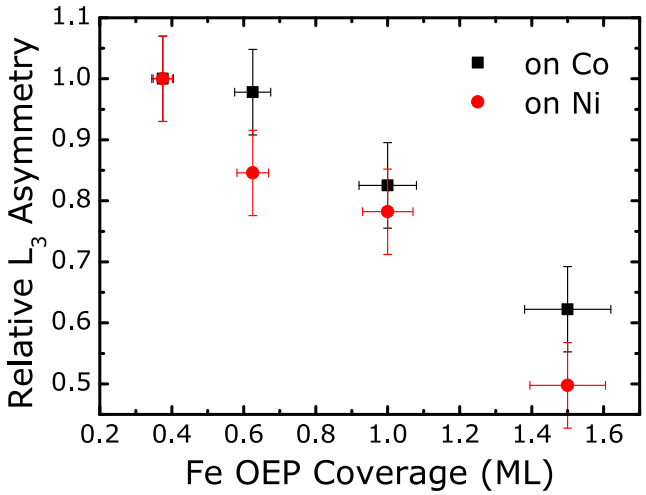

Figure 4.21: Fe OEP coverage dependence of the integrated intensities of Fe-L_3 XMCD normalized to the white line on 5 ML Co/Cu(100) (black) and 15 ML Ni/Cu(100) (red) substrates. The values obtained at the lowest coverage are normalized to unity in both cases.

1 ML, it increases with increasing thickness. For 1.5 ML the XMCD signal is almost the same as for 1 ML.

The Fe-$L_{2,3}$ XA spectra for the Ni substrate case (figure 4.20c) show a very different lineshape. Both edges display narrow peaks at 708.1 eV and 721 eV, each with two shoulders at lower and higher photon energies. No clear thickness dependence is observed in the lineshapes. However, from the difference spectrum between 1.5 ML and 1 ML three features at 706.0 eV, 707.2 eV, and 708.5 eV become apparent as Fe-L_3 XAS signal of the molecules in the second monolayer. The XMCD signal is characterized by a narrow peak at 708.1 eV preceded by a small feature at 705.8 eV; these features are reproduced in the L_2 edge.

The nature of the magnetic coupling of the Fe porphyrin molecules to the magnetic substrates can be understood more clearly from the analysis of the integrated intensities of the Fe-L_3 XMCD signal normalized to the white line, shown in figure 4.21 as a function of coverage on Co and on Ni. The values obtained at the lowest coverage are normalized to unity in both cases. It can be seen that the magnetic signal of the deposited Fe porphyrin molecules originates mostly from the first molecular layer only: on Co, the ratio remains constant (within the error bars) for 0.4 and 0.6 ML, and only decreases for films thicker than $\sim$1 ML. In the case of Ni, the XMCD/XAS

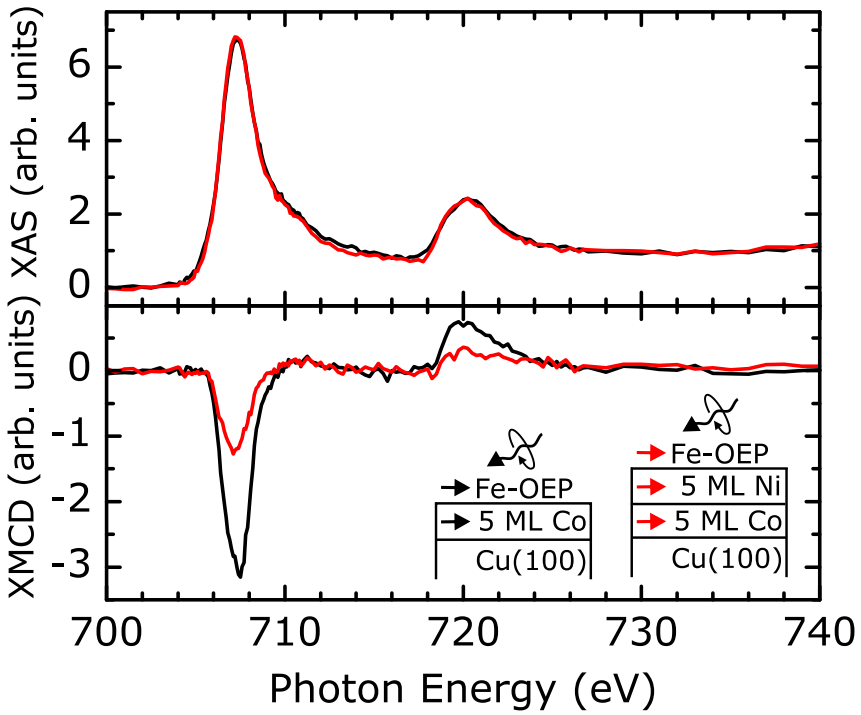

Figure 4.22: Fe-$L_{2,3}$ XAS and XMCD spectra of 0.8 ML Fe OEP molecules deposited on 5 ML Co/Cu(100) (black) and on 5 ML Ni/5 ML Co/Cu(100) (red) substrates. The spectra were recorded at 20° grazing incidence at room temperature.

ratio decreases monotonically with thickness, suggesting a higher percentage of heterogeneously adsorbed molecules.

The reason for the different lineshapes for the Co and Ni substrates is not a substrate-dependent hybridization mechanism, but is purely of geometrical origin: the different experimental geometries (grazing and normal incidence for Co and Ni, respectively) probe different unoccupied Fe-3*d* orbitals. This is readily proven by comparing the spectra taken on Co and on Ni for the same geometry. By preparing a 5 ML Ni film on a 5 ML Co film, the Ni magnetization is forced to the in-plane direction by the Co magnetization. As can be seen in figure 4.22, the Fe-$L_{2,3}$ XAS and XMCD spectra of 0.8 ML Fe OEP on Co and on Ni/Co, measured at grazing incidence, show exactly the same lineshape. However, the magnitude of the XMCD signal on Ni is reduced by approximately 60% compared to that on Co. This implies that the Fe magnetization is lower when coupled to a Ni substrate.

Besides an apparent reduction of the magnetization originating from

molecules that are not coupled magnetically to the substrate, the established magnetic exchange interaction might not be sufficient to fully align the magnetic moment of the molecules. This issue is addressed by temperature-dependent measurements of the Fe magnetization.

Figure 4.23 shows the Fe-$L_{2,3}$ XAS and XMCD signals recorded at 300 K and ∼80 K for 0.8 ML Fe porphyrin molecules on Co and Ni substrates. Whereas the XAS does not show any noticeable temperature dependence for the two cases, the XMCD amplitude does vary with T. Furthermore, any temperature-dependent change is fully reversible, as can be seen in figure 4.23d XMCD spectra when they were successively recorded at 300 K, 70 K and then again at 300 K. Besides scaled by a common factor, all spectral features found at 300 K, remain at low temperatures.

Since the magnetization of the substrate also changes with temperature, the relative change of the Fe-to-substrate magnetization has to be considered. The Curie temperatures of 5 ML Co and 15 ML Ni films are reported to be around 850 K [144] and 550 K [145], respectively. For the Ni film, the XMCD signal at room temperature is reduced by 15% compared to the signal at 70 K–the Co XMCD only reduces by 5%.

The Fe magnetization on Co follows that of the substrate and decreases by ∼10% when going from 85 K to 300 K. In contrast, the Fe XMCD on Ni shows a much larger reduction–of ∼50%–than that of the Ni magnetization upon changing the temperature from 70 K to 300 K.

The difference of the Fe XMCD signal of molecules deposited on Ni as compared to to the ones deposited on Co indicates that the magnetic coupling to Ni is lower than to Co. Furthermore, if the Fe ion detached from the molecule and adsorbed directly on the underlying film, it would be expected that the Fe magnetization directly follows the $M(T)$ curve of the film. This is not the case on Ni which is an additional indication that the Fe ion remains at the center of the porphyrin ring. The weaker coupling strength in the case of Fe OEP on Ni also supports the indirect coupling mechanism found by theory [142]. However, it should be noted that on the basis of the experimental technique it cannot be distinguished between a direct or indirect coupling mechanism.

Since a indirect magnetic coupling mechanism through the nitrogen atoms was found by theory, we have attempted to measure a magnetization at the N-K edge. In figure 4.24 the N-K XMCD is shown for 0.6 ML of

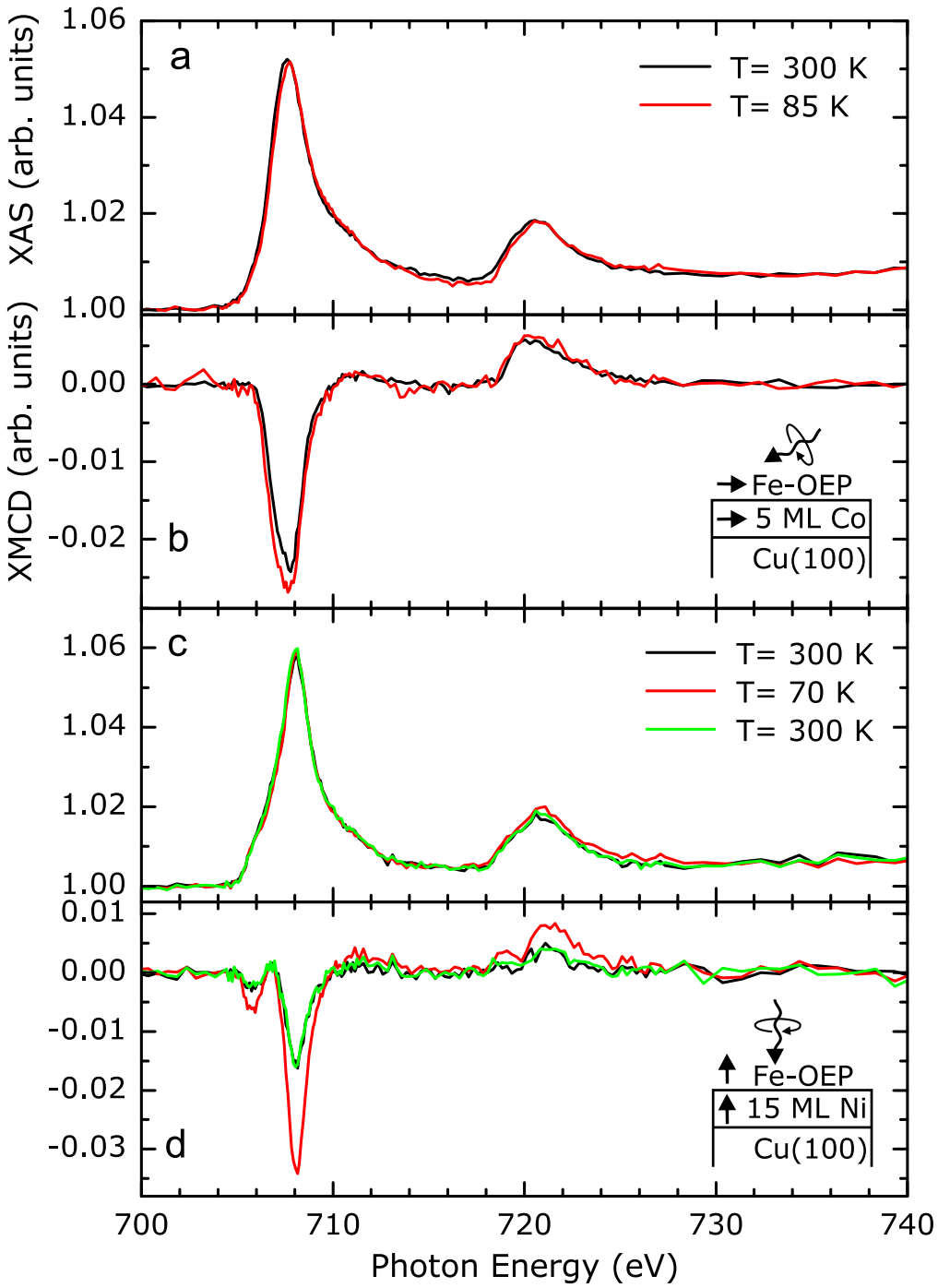

Figure 4.23: Fe-$L_{2,3}$ XAS and XMCD spectra for 0.8 ML Fe OEP molecules on Co (a, b) substrate recorded at 300 K and 85 K, and on Ni (c, d) at 300 K, 70 K, and 300 K by consecutive temperature-dependent measurements.

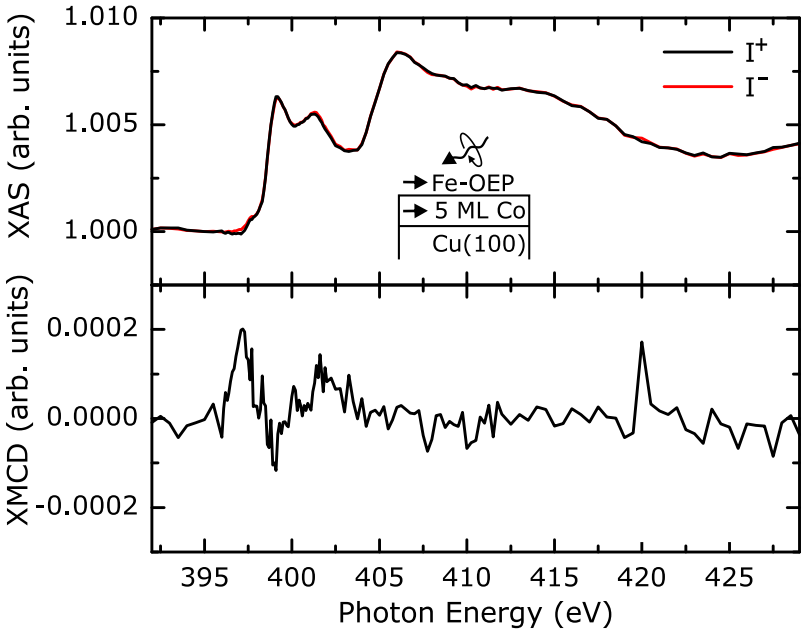

Figure 4.24: N-*K* XMCD spectra for 0.6 ML Fe OEP molecules on 5 ML Co/Cu(100) recorded at room temperature with left and right circularly polarized X rays (top, black and red).

Fe OEP on 5 ML Co/Cu(100). The spectra have been obtained by averaging 8 XMCD pairs. Despite the excellent signal-to-noise ratio, no magnetic signal at the nitrogen sites is found. The spurious XMCD signal at 397 eV originates from the Co-L_2 edge of the substrate probed with the second order of the monochromator. However, the absence of an N-*K* XMCD does not imply the absence of magnetization at the nitrogen sites since XMCD at the *K* edge is not sensible to spin moment but only to orbital moment [23].

4.6 Determination of the Coupling Energy

In this section, the coupling energy E_{ex} of the Fe magnetic moment μ^{Fe} to the substrate magnetic moments μ^{sub} will be estimated by measuring the temperature dependence of the Fe and substrate magnetization. Considering a paramagnet in an external magnetic field $\vec{H}$, the magnetic moments are aligned *via* the Zeeman energy. In an ensemble of molecules, the corresponding energy levels are populated according to Boltzmann's statistics, favoring an equal population of the levels at elevated temperatures. The dependence of the average magnetic moment on the temperature and the

magnetic field is given by the so-called Brillouin function $B_J(\alpha)$ [60]:

$$\begin{aligned}\langle \mu_z^{\mathrm{Fe}} \rangle =& \mu^{\mathrm{Fe}} B_J\left(\frac{H\mu^{\mathrm{Fe}}}{k_B T}\right),\\ B_J(\alpha) =& \frac{2J+1}{2J}\coth\left(\frac{2J+1}{2J}\alpha\right) - \frac{1}{2J}\coth\left(\frac{1}{2J}\alpha\right),\end{aligned}$$

where J is the total angular momentum determining the number of energy levels $(2J+1)$.

The magnetic coupling to the substrate can be introduced in the framework of a *mean field approach* [60] as an effective magnetic field H_{eff}. The way the temperature dependence of the substrate magnetization enters depends on the correlation of the thermal fluctuations of the adsorbate and substrate magnetic moments. If the fluctuations are not correlated, the adsorbate magnetic moment would experience a time-averaged magnetic moment of the substrate: $H_{\mathrm{eff}} = \gamma\langle \mu_z^{\mathrm{sub}} \rangle$ (model A). If the fluctuations are strongly correlated, the effective field would be proportional to the substrate magnetic moment $H_{\mathrm{eff}} = \gamma\mu^{\mathrm{sub}}$, and the time-average acts on the whole expression, *i.e.*, the reduction of the substrate magnetization at elevated temperatures enters as a prefactor to the Brillouin function (model B). The two models take the form:

$$\begin{aligned}\mathrm{A}: \langle \mu_z^{\mathrm{Fe}} \rangle &= \mu^{\mathrm{Fe}} B_J\left(\frac{\gamma \frac{\langle \mu_z^{\mathrm{sub}} \rangle}{\mu^{\mathrm{sub}}} \mu^{\mathrm{sub}} \mu^{\mathrm{Fe}}}{k_B T}\right),\\ \mathrm{B}: \langle \mu_z^{\mathrm{Fe}} \rangle &= \mu^{\mathrm{Fe}} \frac{\langle \mu_z^{\mathrm{sub}} \rangle}{\mu^{\mathrm{sub}}} B_J\left(\frac{\gamma \mu^{\mathrm{sub}} \mu^{\mathrm{Fe}}}{k_B T}\right).\end{aligned}$$

Within these models, the relative magnetization $\mu_r^i = \langle \mu_z^i \rangle / \mu^i$ can be fitted to the experimental data, obtaining the exchange energy $E_{\mathrm{ex}} = \gamma\mu^{\mathrm{sub}}\mu^{\mathrm{Fe}}$ as the fitting parameter:

$$\mathrm{A}: \mu_r^{\mathrm{Fe}} = B_J\left(\mu_r^{\mathrm{sub}} \frac{E_{\mathrm{ex}}}{k_B T}\right), \quad \mathrm{B}: \mu_r^{\mathrm{Fe}} = \mu_r^{\mathrm{sub}} B_J\left(\frac{E_{\mathrm{ex}}}{k_B T}\right). \tag{4.1}$$

In figure 4.25, the Fe and Ni XMCD signals at fixed photon energies, normalized to the extrapolated saturation values, are plotted *vs.* temperature for 0.6 ML of Fe OEP molecules on 15 ML Ni and 6 ML Ni on Cu(100), respectively. The easy magnetization axis of the latter sample is in-plane (along [110] direction), since the spin-reorientation transition for Ni films

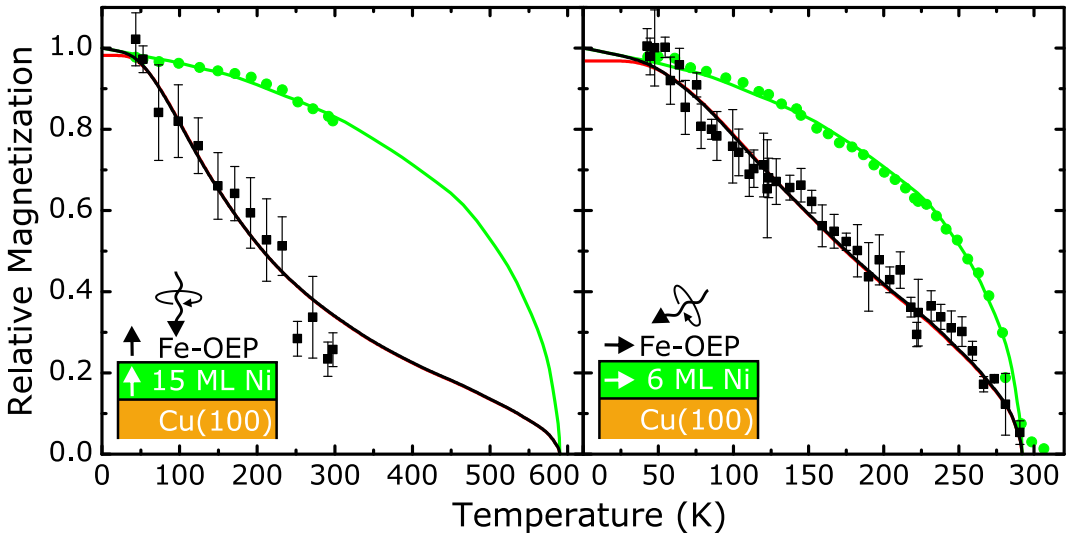

Figure 4.25: Temperature dependence of the relative magnetization of the Fe atoms (squares) and the Ni substrates (circles; green lines: empirical curve taken from reference [146]) for 0.6 ML Fe OEP on (left) 15 ML Ni/Cu(100), and (right) 6 ML Ni/Cu(100). The fit of the Brillouin-type models to the Fe magnetization is shown as red (model A) and black (model B) lines.

on Cu(100) occurs at approximately 11 ML [59, 62, 63][5]. The Curie temperature of the 6 ML Ni sample is only $T_C = 285$ K, according to the *finite-size law* [61]. The temperature-dependent magnetization of the substrate is approximated with an empirical curve (green lines) taken from reference [146] and inserted into the theoretical model as μ_r^{sub}. For both samples, the evolution of the Fe magnetization deviates drastically from that of the substrate.

The temperature dependences of the Fe magnetizations are reproduced by both models (A: red lines, B: black lines). These two models yield almost identical functional behavior, deviating only for temperatures below 50 K, where model A saturates earlier. Even for the 6 ML Ni sample, exhibiting a comparably strong variation of the Ni magnetization, the difference between the two models is small. This implies that experimentally we cannot discern which model is more appropriate. However, we can assume that the Fe–substrate coupling acts on a much faster timescale than the fluctuations, consistent with the second model.

[5] A shift of the spin-reorientation transition [59, 63] below 6 ML can be excluded here due to the presence of an in-plane Ni XMCD signal.

Fe OEP model	on 15 ML Ni A	on 15 ML Ni B	on 6 ML Ni A	on 6 ML Ni B
$J = 1$	16.9	17.0	16.9	17.9
$J = 1.5$	20.1	20.3	20.3	21.7
$J = 2$	22.1	22.4	22.5	24.2
$J = 2.5$	23.5	23.8	24.0	26.0

Table 4.1: Exchange energies in meV obtained from a fit of the two models (equation 4.1) to the temperature dependent Fe-L_3 XMCD signal of 0.6 ML Fe OEP on out-of-plane magnetized 15 ML Ni/Cu(100) and in-plane magnetized 6 ML Ni/Cu(100). The sensitivity of the determined exchange energies on the total angular moment is evaluated by comparing the results for different values of J.

In table 4.1 the exchange energies as obtained from the fit to the experimental data for different values of J are listed. For a divalent Fe oxidation state, as suggested by the XAS peak positions, with an intermediate spin state configuration of the d electrons, a spin moment of $S = 1$ would be expected. This results in a total angular moment of $J = 1$ if the orbital moment is quenched. A higher oxidation state of the Fe ion or an orbital moment that is not totally quenched would lead to an increase of the total angular moment. For $J = 1.5$, the resulting exchange energies show only a slight increase by 5% compared to $J = 1$. If a high-spin ground state is assumed, spin moments of $S = 2$ and $S = 2.5$ for divalent and trivalent Fe are expected, respectively. The resulting exchange energies rise by about 20% to 30%. The two models yield identical values of the exchange energy within 2% for all values of J.

For the curves shown in figure 4.25, a total angular momentum of $J = 1$ is assumed as it would be expected for an Fe^{2+} ion with intermediate spin-state ($S = 1$) and a quenched orbital moment, consistent with the results of the sum rules presented in table 4.2. Very similar values for the exchange energy of 17 meV and 18 meV (model B) are determined for out-of-plane and in-plane magnetized Ni substrates, respectively. This indicates that there is no significant dependency of the magnetic coupling on the magnetization axis.

The exchange energy on Co is estimated from the two temperature-

dependent XMCD signals shown in figure 4.23. For $J = 1$, a value of $E_{ex} = 70$ meV is found, implying that a much larger coupling is present between the Fe spin of the molecules on Co as compared to the Ni substrate. From the preceding case, it is already clear that this difference in coupling energies is not connected to the difference in the magnetization direction, but is predominantly an effect of the magnetic and/or electronic differences between the Ni and Co substrates. As a possible explanation for the reduced coupling energy in the Ni case, we can consider the 60% smaller magnetic moment of Ni surfaces as compared to the Co ones [147, 148]. However, the extent of this difference can be altered by the presence of the molecules adsorbed on the surfaces [149].

4.7 Tailoring of the Magnetic Coupling

In the previous section it was shown that the magnetic moment of Fe OEP molecules can be aligned by an underlying ferromagnetic substrate. Furthermore, different coupling energies were found on Ni and Co substrates. It is tempting to expand the possibilities of tailoring the magnetic coupling both in magnitude and sign by engineering the interface between the molecule and the ferromagnetic films. This section demonstrates how a tailoring of the magnetic coupling can be achieved by introducing half a monolayer of atomic oxygen in between Fe OEP molecules and FM Ni and Co films.

The Ni and Co films were epitaxially grown on a preoxidized Cu(100) single crystal, as discussed in section 2.4. The oxygen atoms act as a surfactant for the growth of the FM films, floating on top of the surface [24, 59]. This results in a well-characterized $c(2 \times 2)$ superstructure of 0.5 ML atomic oxygen on top of the ferromagnetic films. Successively, Fe OEP molecules were deposited onto the substrate held at room temperature.

Figure 4.26 shows the Fe-$L_{2,3}$ XAS and XMCD spectra for 0.6 ML Fe OEP on O/5 ML Co/Cu(100) (red lines, panel a), O/10 ML Ni/Cu(100) (red lines, panel b), 5 ML Co/Cu(100) (black lines, panel a), and 15 ML Ni/Cu(100) (black line, panel b), measured at normal (grazing) incidence for the Ni (Co) samples. All spectra were measured at $T = 40$ K except for the Co/Cu(100) sample, which were measured at room temperature. Due to the comparably strong coupling of the molecules on the Co surface,

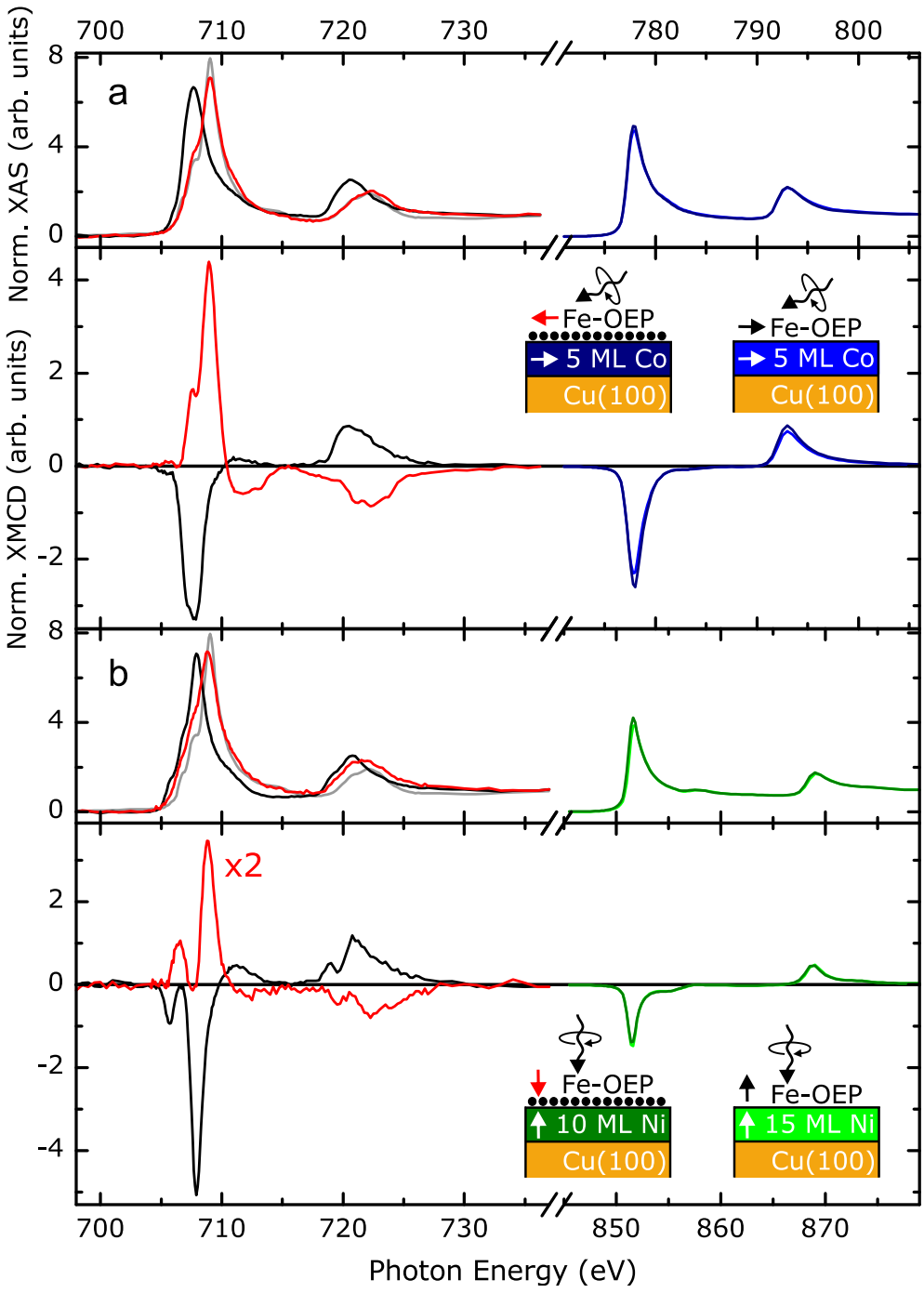

Figure 4.26: Fe-$L_{2,3}$ XAS and XMCD spectra of 0.6 ML Fe OEP on oxygen-covered (red lines) and bare (black lines) Co (panel a) and Ni (panel b) substrates. The corresponding Ni and Co spectra are shown on the right. All spectra were measured at $T = 40$ K except for the Co/Cu(100) sample, which were measured at room temperature. For comparison, the XAS data of Fe OEP Cl bulk is shown in gray.

only a minor increase of the XMCD is expected at low temperatures. On the oxygen-covered ferromagnetic films, an opposite sign of the Fe XMCD signals with respect to the substrate magnetizations is observed, evidencing an antiparallel alignment of the Fe spin with the substrate magnetization. By sweeping the external magnetic field, the Fe magnetization reverses at the same field as the substrate while maintaining the antiparallel alignment. This AFM coupling is found only in the presence of the oxygen layer. In contrast, the Fe XMCD on the bare ferromagnetic films shows the same sign as the XMCD of the Co and Ni substrate. The reversal of the magnetization direction can be understood considering that the magnetic coupling to the FM films is established by superexchange through the oxygen atoms. In this picture, one lobe of the oxygen p_z orbital hybridizes with substrate d orbitals and the other lobe with the d orbitals of the Fe center of the molecules. Since the p_z orbital is odd in z, the spins at the two lobes are opposite in sign.

In our recent work [150], DFT+U calculations of an Fe porphin molecule bond *via* an oxygen atom to a ferromagnetic stack of 3 ML Co are carried out to gain insight into the coupling mechanism. A self-consistent optimization of the molecular structure, including the O ligand binding to Fe and the Co surface, by complete relaxation of the interatomic forces was performed. It could be shown that indeed a superexchange interaction across the oxygen atom is responsible for the antiparallel alignment. Furthermore, the Fe–O and Co–O bond lengths were computed as 1.92 Å and 1.74 Å, respectively. The central Fe atom moves out of the macrocyclic plane by 0.29 Å owing to the O ligation, as typically seen for axial ligation of metalloporphyrins.

The effect of the adsorbed Fe OEP molecules on the oxygen atoms is depicted in figure 4.27. The O-K edge is shown for normal and grazing incidence before and after the adsorption of 0.6 ML of Fe OEP onto O/5 ML Co/Cu(100). A reduction of the oxygen π^* resonance at 530 eV upon the adsorption of the Fe porphyrin molecules is clearly observed. This indicates an increase of charge at the oxygen atoms as a result of an electronic interaction with the molecules.

The hybridization of the Fe d with the oxygen p orbitals not only changes the sign of the Fe magnetization, but also modifies the electronic properties of the metal center. This can be seen by comparing the Fe XAS of the two samples. The energy position of the Fe XAS peaks is an indicator for the Fe valence state [40]. Charge-transfer processes that may occur during the evaporation and adsorption of Fe OEP onto the O/metal sub-

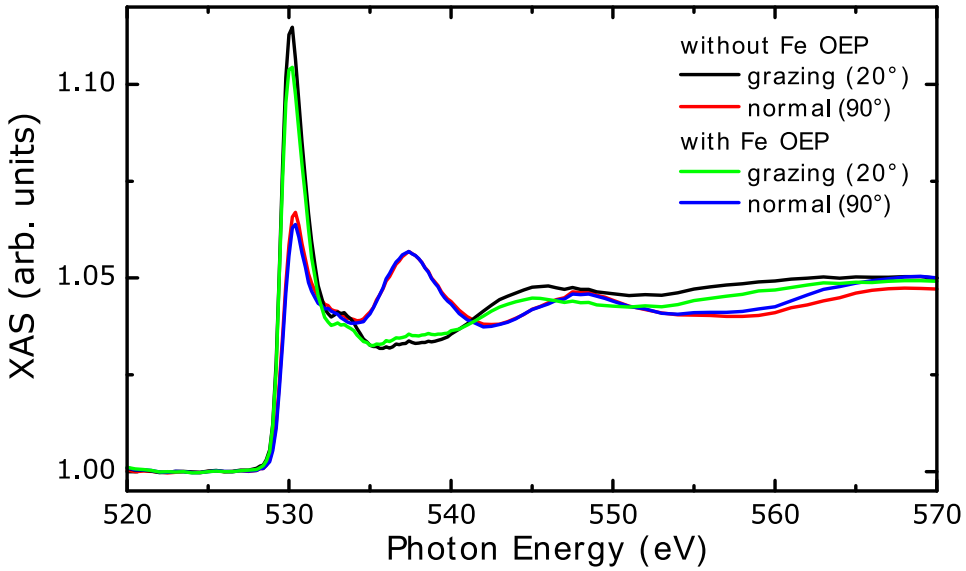

Figure 4.27: O-*K* XA spectra before (black and red) and after (green and blue) deposition of 0.6 ML Fe OEP on O/5 ML Co/Cu(100) measured with linearly polarized X rays at grazing (20°, black and green) and normal (90°, red and blue) incidence angles at room temperature.

strates would affect the Fe valence state. In the case of the surfactant-grown substrate (red lines in figure 4.26) the Fe-L_3 XAS peak positions coincide with those of an Fe(III) OEP Cl bulk sample (grey lines), implying a trivalent Fe ion. On the contrary, a red-shift of about 1 eV is visible on the bare metallic substrates, suggesting an increase in the number of 3*d* electrons at the Fe site. For Ni samples, the spectral shape of the Fe XMCD signals is very similar, besides the shift in energy. It is reasonable to assume that the Fe d_{z^2} orbital is strongly affected by the presence of the oxygen ligand and shifts towards higher energies. On O/Co, a much stronger XMCD signal is found as compared to O/Ni. Since both measurements were recorded at $T = 40$ K, a difference in the magnetic coupling strength cannot be the explanation. Due to the comparably broad Fe-L_3 edge, one might tend to attribute the reduction of the Fe XMCD signal on O/Ni to a heterogeneous adsorption of Fe OEP molecules, resulting in a mixture of antiferro- and ferromagnetically coupled porphyrin molecules with 3^+ and 2^+ oxidation states of the Fe, respectively. The ferromagnetically coupled Fe^{2+} centers would account for the Fe-L_3 XAS signal at lower photon energies and the antiferromagnetically coupled Fe^{3+} centers would constitute the part of the signal at higher photon energies. However, such a picture has to be aban-

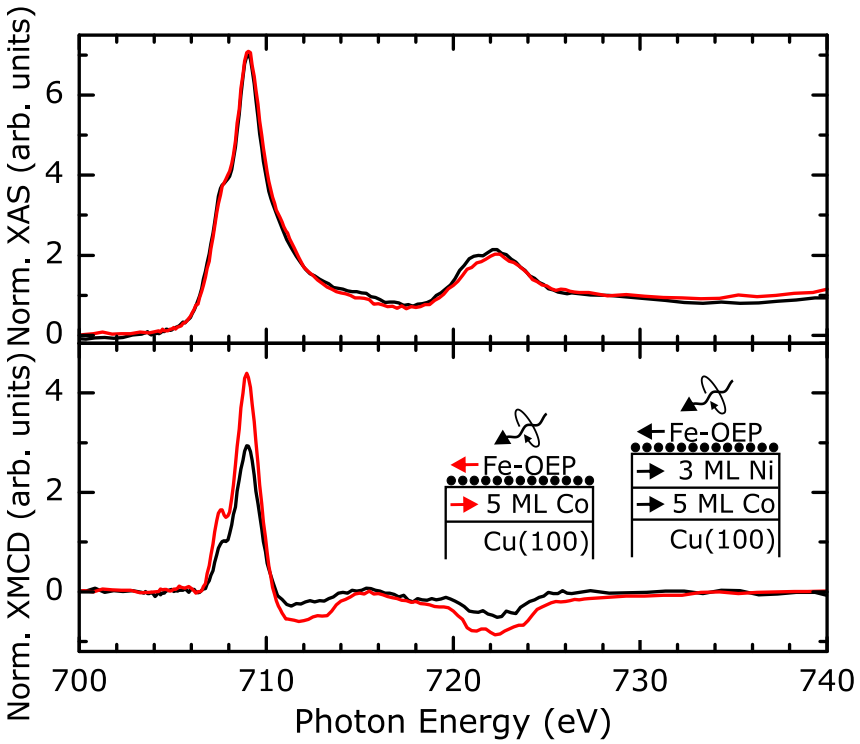

Figure 4.28: Fe-$L_{2,3}$ XAS (upper panel) and XMCD (lower panel) spectra of 0.6 ML Fe OEP on surfactant-grown O/3 ML Ni/5 ML Co/Cu(100) (black lines) at $T = 35$ K and O/5 ML Co/Cu(100) (red lines) at $T = 40$ K.

doned since the energetic distribution of the AFM Fe XMCD signal covers the whole L_3 peak region down to 705.5 eV.

In order to investigate the strong difference in size between the XMCD signals on O/Ni and on O/Co, 0.6 ML Fe OEP were deposited onto a surfactant-grown, in-plane magnetized, O/3 ML Ni/5 ML Co/Cu(100) bilayer. Figure 4.28 shows the Fe-$L_{2,3}$ XMCD spectrum, recorded at grazing incidence and $T = 35$ K, together with the corresponding spectrum on O/5 ML Co/Cu(100). Besides a reduction by ∼30%, analogous to the one described in figure 4.22, the Fe XMCD signal closely resembles the shape of the one on the O/Co surface. Hence, the strong deviation between the Fe XMCD signals of Fe OEP adsorbed onto oxygen-covered Ni and Co substrates is not a consequence of different properties of the surfaces, but reflects the asymmetry of the spin density at the Fe site, *i.e.*, the impact of the magnetic dipole operator $\langle T_\alpha \rangle$ after summing over all d orbitals. The anisotropy of the spin density is not compatible with an Fe^{3+} HS state since

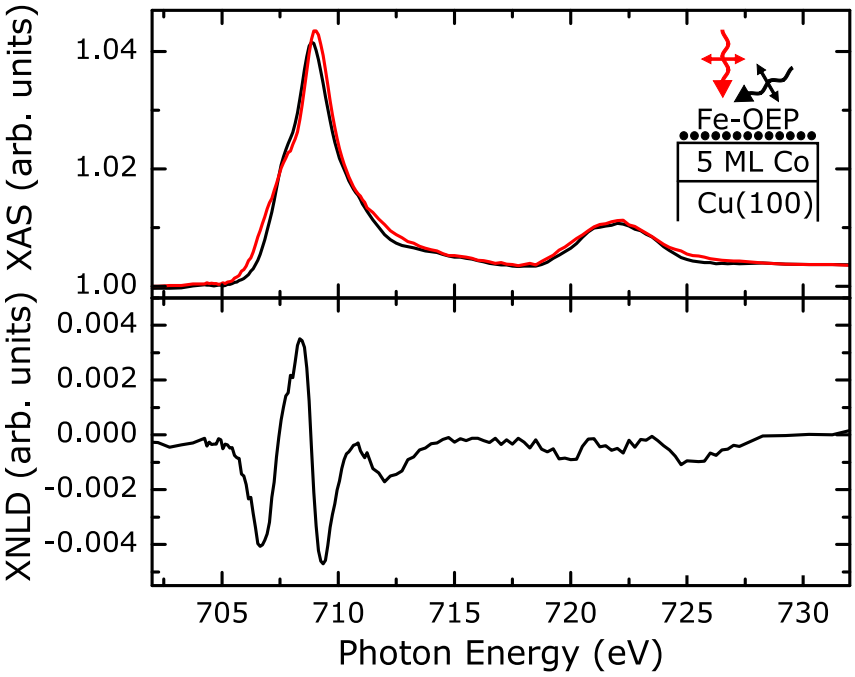

Figure 4.29: Fe-$L_{2,3}$ XA spectra (upper panel) of 0.6 ML Fe OEP on O/5 ML Co/Cu(100) recorded at grazing (black) and normal (red) incidence using linearly polarized X rays. The XLD intensity difference is shown in the lower panel. For comparison, the XAS data of Fe OEP Cl bulk is shown in gray.

in this case all *d* orbitals would be singly occupied, yielding an isotropic spin density in total.

In figure 4.29, the Fe-$L_{2,3}$ grazing (20°) and normal (90°) incidence XA spectra of 0.6 ML Fe OEP on O/Co/Cu(100) at room temperature are shown, together with the XNLD difference spectrum in lower panel. The lineshape hardly varies with the angle, indicative of an almost isotropic charge distribution of the individual 3*d* electronic levels, similar to the case of Fe OEP on O/Cu(100), presented in figure 4.13.

In order to estimate the coupling energy E_{ex} of the Fe magnetic moment to the O/Ni and O/Co substrates, the temperature dependence of the magnetizations of the FM films and of the Fe centers in the molecules were studied. In figure 4.30 the Fe, Ni, and Co XMCD signals at fixed photon energies, normalized to the extrapolated saturation values, are plotted *vs.* temperature. For both samples the evolution of the Fe magnetization deviates drastically from that of the substrate. For Fe OEP on O/Co, the Fe

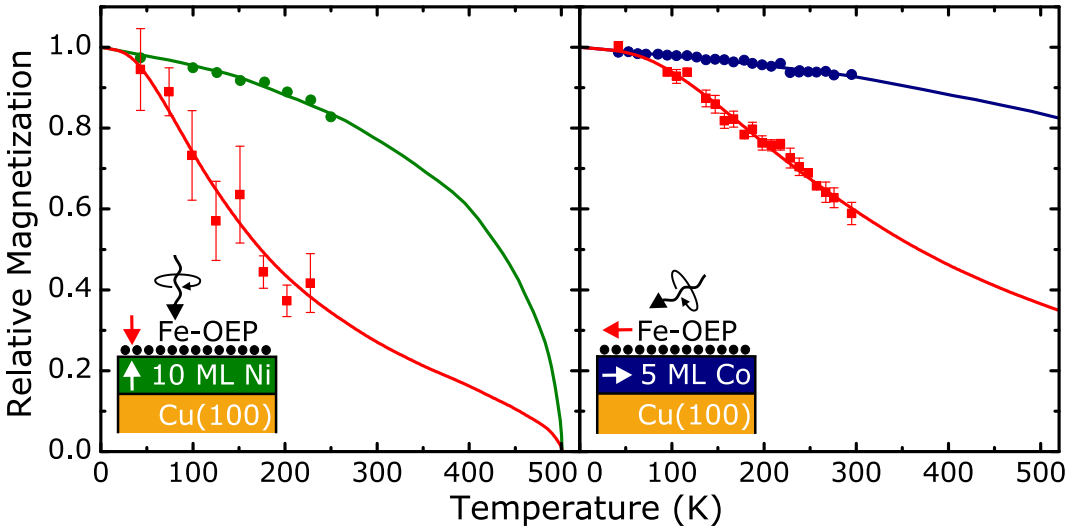

Figure 4.30: Temperature dependence of the relative magnetization of the Fe atoms (squares; red lines: fit of Brillouin-type model) and the Ni and Co substrates (circles; green and blue lines: empirical curve) for 0.6 ML Fe OEP on (left) O/10 ML Ni/Cu(100), and (right) O/5 ML Co/Cu(100).

magnetization is closer to the substrate temperature curve than for the Ni sample, indicating a stronger coupling energy.

The model derived in section 4.6 is fitted to the data. A trivalent Fe oxidation state and an intermediate spin state that result in a spin moment of $S = 3/2$ are assumed, consistent with Fe-L_3 XAS peak position and the strong impact of the magnetic dipole operator (*cf.* figures 4.26 and 4.28). For Fe OEP on O/Co, a coupling energy of 37 meV is obtained, being about half of that for the direct adsorption of the molecules on a Co substrate as derived in the previous section. In contrast, the value of 17 meV obtained for Fe OEP on O/Ni is identical to that on Ni/Cu(100). These values are of the same order of magnitude as in bulk transition-metal monoxides (*e.g.*, $E_{\mathrm{ex}}^{\mathrm{NiO}}$=17 meV/bond [151]). Assuming high-spin ground states, the resulting exchange energies are higher by about 20% to 30%.

In the following, the role of the Fe *d* and N *p* orbitals in the magnetic coupling to the metallic and to the surfactant-grown substrates will be discussed. For Fe OEP molecules directly adsorbed onto Co metallic films, DFT+U calculations revealed a ligand-mediated indirect coupling to the substrate across the nitrogen atoms [142]. In figure 4.31, the N-*K* XAS signals of 0.6 ML Fe OEP molecules on an oxygen-covered (panel a) and on a

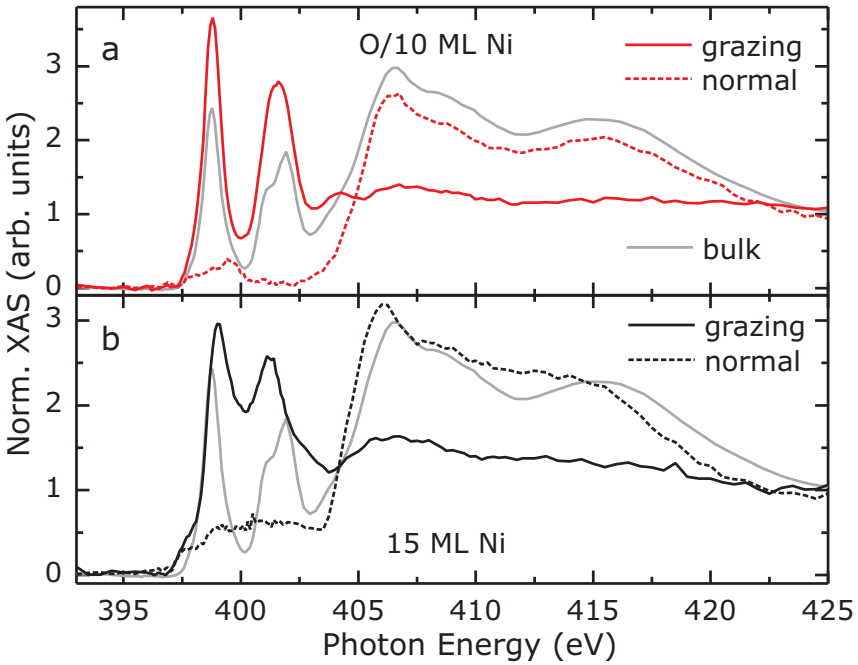

Figure 4.31: N-*K* edge XAS signals of 0.6 ML Fe OEP (a) on O/10 ML Ni/Cu(100) and (b) on 15 ML Ni/Cu(100) at grazing (full lines) and normal (dashed lines) X-ray incidence with 70° and 0° of the *E* vector to the surface, respectively. The gray lines show the N-*K* edge spectrum for a polycrystalline bulk sample.

bare Ni film (panel b) are compared. In both cases, the spectra at grazing X-ray incidence (full lines) are dominated by two π^* resonance peaks, whereas at higher energies σ^* resonance peaks appear at normal incidence (dashed lines). However, a smaller broadening and increased splitting of the N π^* resonances is observed for Fe OEP on O/Ni, as compared to the signals on the bare Ni substrate, which closely resembles the spectral shape of the Fe(III) OEP Cl bulk sample. This indicates an effective electronic decoupling of the N atoms from the substrate after introducing oxygen. Therefore, we expect an Fe–O–Co AFM superexchange coupling that will not involve the N atoms, in contrast to the case of the metallic substrate.

In table 4.2 the results of the sum-rule analysis, as described in section 1.4.1, of the spectra presented in figure 4.26 are shown. The integrals over the XAS and XMCD $L_{2,3}$ signals are evaluated from the same pair of spectra in order to avoid additional source of errors by using the spectra of separate measurements at different angles. Instead, the angle-dependent

Fe OEP	μ_S^{eff}/μ_B	μ_L^{α}/μ_B	$\mu_L^{\alpha}/\mu_S^{\text{eff}}$
on 15 ML Ni	2.66(40)	0.13(7)	0.05(2)
on 5 ML Co	2.58(26)	0.32(8)	0.12(3)
on 10 ML O/Ni	−1.13(23)	−0.12(6)	0.10(5)
on 5 ML O/Co	−3.46(35)	−0.18(5)	0.05(1)

Table 4.2: Effective spin moments, orbital moments, and ratio of orbital to effective spin moment derived from sum-rule analysis for 0.6 ML Fe OEP on bare and oxygen-covered Ni and Co substrates.

variation of the XAS integral is accounted for by the error bars. On the basis of the model discussed in section 4.6 and the exchange energies derived from the fit to the experimental data, the values of the orbital and effective spin polarization are extrapolated to $T = 0$ K to obtain the orbital moment and the effective spin moment from the expectation values of the corresponding operators by extrapolation. The number of d-holes is assumed to be $n_h = 4$ and $n_h = 5$ for Fe OEP on bare and oxygen-covered substrates, respectively, as suggested by the Fe-L_3 XAS peak positions. The effective spin moment μ_S^{eff}, the orbital moment μ_L^{α}, and the ratio of orbital to spin moment $\mu_L^{\alpha}/\mu_S^{\text{eff}}$ are shown for 0.6 ML Fe OEP on bare and oxygen-covered Ni and Co films. Without oxygen, similar values of the effective spin moment are found for Ni and Co substrates. Both values are closer to an intermediate spin state $S = 1$ ($\mu_S = 2\ \mu_B$) than to a high spin state $S = 2$ ($\mu_S = 4\ \mu_B$). With oxygen, the moment on Co is much higher than on Ni, reflecting the impact of the magnetic dipole operator for the different incidence directions, as discussed in connection with figure 4.28. For a HS state with $S = 2.5$ a spin moment of 5 μ_B would be expected, much higher than observed experimentally. From the remaining two possibilities the intermediate spin state ($S = 1.5$) seems to be more like than the LS state ($S = 0.5$). Values between 0.1 and 0.4 μ_B are found for the orbital moments in the corresponding directions.

CONCLUSIONS

A detailed study of two classes of transition metal complexes on surfaces has been presented. Spin-crossover (SCO) complexes, prepared as monomolecular layers, were investigated by X-ray absorption spectroscopy (XAS). The magnetic properties of quasi-planar Fe and Co octaethylporphyrin (OEP) molecules on surfaces were analyzed by means of X-ray magnetic circular dichroism (XMCD). The magnetic coupling of Fe OEP molecules to ferromagnetic (FM) substrates was investigated by systematic temperature- and thickness-dependent XMCD measurements.

Monomolecular layers of Fe(II) SCO complexes were prepared by *in-situ* sublimation onto Au(111) substrates and self-assembly on Au(111)/mica. The SCO transition of $Fe(phen)_2(NCS)_2$ and $Fe(phen)_2(NCSe)_2$ bulk samples was probed at the Fe-$L_{2,3}$ edges, reproducing the XAS signals characteristic of the Fe high-spin (HS) and low-spin (LS) states. A strong modification of the electronic structure of the N ligands is observed for $Fe(phen)_2(NCS)_2$, whereas for $Fe(phen)_2(NCSe)_2$ a much smaller influence is found. The evaporation process of $Fe(phen)_2(NCS)_2$ is accompanied by the production of phenanthroline fragments. The co-deposition results in a decoupling of the $Fe(phen)_2(NCS)_2$ molecules from the surface by the presence of phenanthroline molecules. For a mixed multilayer of $Fe(phen)_2(NCS)_2$ and phenanthroline on Au(111), a partly reversible SCO transition is evidenced. However, if the concentration of the phenanthroline molecules in the organic layer is reduced by desorption, the spin transition is partly suppressed. This behavior is explained by the formation of covalent bonds between the isothiocyanate ligands and the Au(111) surface, as indicated by the presence of an additional sulfur species in the S 2p XPS. For $Fe(phen)_2(NCSe)_2$ on Au(111), a HS state of the Fe ion is found at room and at low temperatures. Although the observation

of an SCO transition for $Fe(phen)_2(NCS)_2$ on Au(111) is a promising step towards the realization of surface-mounted molecular switches, the high reactivity of the thiocyanate ligands requires an efficient decoupling of the molecules and the surface or the utilization of highly inert substrates. Since XAS involves conducting samples, such substrates may be given by thin oxidic layers on metal single crystals or highly oriented pyrolytic graphite.

Mono- and multilayers of $Fe(bp)_2$ were deposited by sublimation onto Au(111). It is shown that the molecule stays intact, even when in direct contact with the Au(111) surface. Furthermore, the oxidation state of its Fe center is preserved. In the monolayer regime, the molecules show a preferential orientation with the rotational symmetry axis of the molecule parallel to the surface. By comparison of the Fe-$L_{2,3}$ XAS signal of $Fe(bp)_2$ to the corresponding bulk material, an Fe HS state is deduced. However, no change of the spin state is found when decreasing the temperature down to 18 K. This implies that the ligand field strength would need to be increased in order to achieve an SCO transition on the surface, which may be possible by chemical modification of the ligands. The case of a weakly interacting, sublimable complex is rather interesting, since it promises to combine robust electronic properties of the central ion with the possibility to tune the intermolecular and molecule–substrate interaction by co-deposition of additional molecules and choice of the substrate.

In contrast to sublimation of molecules in UHV conditions, wet-chemical deposition *via* covalent linkage of the molecules provides the possibility to use complexes that are only available as salts. Since no XAS measurements have been reported for the type of molecules investigated in this thesis, the Fe-$L_{2,3}$ spectral signatures of the HS and LS states are obtained from temperature-dependent XAS of a $Fe(bppm)_2(BF_4)_2$ bulk sample. A weak effect of the SCO transition on the electronic structure at the N sites is found. A self-assembled monolayer of $Fe(bppmc)_2$ was investigated by means of S 2*p* XPS. It is shown that the complex binds covalently to the Au(111) surface with both linker groups. A HS state of the Fe is found, which is preserved down to a temperature of 18 K. No F-*K* XAS signal could be detected whatsoever, implying the absence of BF_4 anions on the surface. This shows that the chemical reaction of the complexes with the surface induces modifications – the impact of these changes on the SCO phenomena must be considered.

Metalloporphyrins are known for their chemical stability allowing for

deposition onto surfaces by sublimation. The magnetic properties of the central ion are strongly influenced by the surface, due to the planar geometry of the complex. The angle-dependent electronic and magnetic properties of Fe and Co OEP molecules, adsorbed onto non-magnetic substrates, were studied by angle-dependent XAS and XMCD measurements. The magnetic moment of the central ion was aligned by an external magnetic field of $B = 5$ T at $T = 8$ K. The combined evaluation of the X-ray natural linear dichroism (XNLD) and the angle-dependent XMCD allows for the investigation of the anisotropy of charge and spin densities of the 3*d* electrons. For Fe OEP on Cu(100), a pronounced XNLD at the Fe-$L_{2,3}$ edges is observed, implying a strong anisotropy of the involved orbitals. The center of mass of the L_3 peak intensity is red-shifted by about 1 eV when varying the orientation of the $\vec{E}$ vector of the X rays from in to out-of the porphyrin plane. By means of the XMCD sum rules, a lower limit for the spin moment of 1 μ_B is obtained from a measurement at the magic angle. An orbital-to-spin magnetic moment ratio of 13% is found. For Fe OEP on a reconstructed $(\sqrt{2} \times 2\sqrt{2})$R45° O/Cu(100) surface, a much weaker XNLD is observed. The Fe center displays a trivalent oxidation state, most likely due to coordination of oxygen acting as a fifth ligand. A huge magnetic anisotropy is observed, resulting in a factor of five between the magnetic signal perpendicular and parallel to the porphyrin macrocycle. A lower limit for the spin moment of 2.7 μ_B is obtained. The ratio of the orbital-to-spin magnetic moment is evaluated to 8%. For Co OEP on O/Cu(100), a 2^+ oxidation state of the Co ion is found. The contributions of the d_{z^2} and $d_{x^2\text{-}y^2}$ orbitals to the spectrum are identified, resulting in an opposite angle-dependent behavior of the corresponding L_3 resonances. The impact of the d_{z^2} orbital is also reflected in the XMCD, where the effective spin moment reverses its sign when the incidence angle is varied. At the magic angle, a lower limit of 0.28 μ_B for the spin moment and a orbital-to-spin magnetic moment ratio of 46% are obtained.

Fe OEP molecules were deposited onto ferromagnetic Ni and Co substrates. In both cases, sizable XMCD signals are found at room temperature, evidencing a substantial magnetic coupling. The Fe magnetic moments and the magnetization of the substrate are aligned parallel. By choice of the substrate, the Fe magnetic moment can be oriented in-plane or out-of-plane. Furthermore, the orientation of the moment can be switched by a magnetization reversal of the ferromagnetic substrate. By a thickness-dependent analysis of the Fe XMCD signal, it is shown that only the molecules in close

proximity to the substrate are ferromagnetically coupled. By means of a temperature-dependent XMCD analysis of the Fe and substrate magnetizations, a much stronger magnetic coupling is found to the Co substrate than to Ni. The coupling energy is estimated by modeling the temperature-dependent Fe magnetization with a Brillouin function, accounting for the coupling to the substrate as an effective magnetic field. Magnetic coupling energies of 17 meV and 70 meV are found for Fe OEP molecules on in- and out-of-plane magnetized Ni and Co substrates, respectively. For Fe OEP on an in-plane magnetized 6 ML Ni/Cu(100) substrate, a coupling energy of 17 meV is determined, demonstrating that the coupling strength is independent on the orientation of the magnetic moment. Similar values of the Fe effective spin moment of 2.6 μ_B and 2.7 μ_B are found on in- and out-of-plane magnetized Co and Ni substrates, respectively. These values indicate an intermediate spin state $S = 1$ of the Fe ion.

Tailoring the magnetic coupling is achieved by half a monolayer of atomic oxygen placed between the Fe porphyrin molecules and the Ni or Co substrates. For the first time, an antiferromagnetic (AFM) coupling of Fe porphyrin molecules to FM substrates has been realized. This finding is deduced from the opposite Fe and substrate XMCD signals of a submonolayer of Fe OEP on O/Ni/Cu(100) and on O/Co/Cu(100). In contrast to the metallic substrates, an Fe 3^+ oxidation state is extracted by comparing the Fe-L_3 XAS signal to that of an Fe OEP Cl bulk sample. From the temperature dependence of the Fe and substrate magnetizations, magnetic coupling energies of 17 meV and 37 meV are found on oxygen-covered Ni and Co substrates, respectively. While the value on O/Co/Cu(100) is reduced with respect to the bare metallic substrate, the value on O/Ni/Cu(100) is identical to the one on Ni/Cu(100), suggesting an indirect coupling also for the case of the bare metal substrates. This is consistent with DFT+U calculations carried out on Fe porphin molecules on Co, identifying the coupling mechanism as a 90° super-exchange interaction through the nitrogen ligands [142]. The N-K XA spectra revealed that there is indeed a significant electronic interaction of the N atoms with the bare metal substrates, whereas, for the oxygen-covered substrates, the bulk properties of the nitrogen atoms remain preserved. In contrast to the bare metal substrates, very different values of the Fe effective spin moment of 3.5 μ_B and 1.1 μ_B are found on oxygen-covered, in- and out-of-plane magnetized Co and Ni substrates, respectively. The origin of this deviation is identified by the angle-dependent contributions of the magnetic dipole operator.

The realization of an AFM coupling of the metal-center spin of Fe porphyrin to the magnetization of the underlying substrate is a leap forward in manipulating the magnetic properties of molecules on surfaces. By tailoring the Fe spin antiparallel, it is then in opposition to the substrate, which dominates the magnetization of the system. This is an enormous advantage when considering the molecule as a spintronic device since it can be used to switch the alignment of the Fe spin from antiparallel to parallel by means of an external stimulus, *e.g.*, a local magnetic field or a spin-polarized current.

BIBLIOGRAPHY

[1] J. V. Barth, G. Costantini, and K. Kern: *Engineering atomic and molecular nanostructures at surfaces*. Nature **437**, 671 (2005), doi:10.1038/nature04166. 1

[2] S. Yoshimoto and K. Itaya: *Advances in supramolecularly assembled nanostructures of fullerenes and porphyrins at surfaces*. J. Porphyrins Phthalocyanines **11**, 313 (2007), doi:10.1142/S1088424607000369. 2

[3] M. Turner, O. P. H. Vaughan, G. Kyriakou, D. J. Watson, L. J. Scherer, G. J. E. Davidson, J. K. M. Sanders, and R. M. Lambert: *Deprotection, Tethering, and Activation of a Catalytically Active Metalloporphyrin to a Chemically Active Metal Surface: $[SAc]_4$P–Mn(III)Cl on Ag(100)*. J. Am. Chem. Soc. **131**, 1910 (2009), doi:10.1021/ja8076389. 2

[4] A. A. Dameron, J. R. Hampton, R. K. Smith, T. J. Mullen, S. D. Gillmor, and P. S. Weiss: *Microdisplacement Printing*. Nano Lett. **5**, 1834 (2005), doi:10.1021/nl050981j. 2

[5] N. Koch: *Organic Electronic Devices and Their Functional Interfaces*. ChemPhysChem **8**, 1438 (2007), doi:10.1002/cphc.200700177. 2

[6] S. Duhm, G. Heimel, I. Salzmann, H. Glowatzki, R. L. Johnson, A. Vollmer, J. P. Rabe, and N. Koch: *Orientation-dependent ionization energies and interface dipoles in ordered molecular assemblies*. Nat. Mater. **7**, 326 (2008), doi:10.1038/nmat2119. 2

[7] M. Mannini, F. Pineider, P. Sainctavit, C. Danieli, E. Otero, C. Sciancalepore, A. M. Talarico, M.-A. Arrio, A. Cornia, D. Gatteschi, and R. Sessoli: *Magnetic memory of a single-molecule quantum magnet wired to a gold surface*. Nat. Mater. **8**, 194 (2009), doi:10.1038/nmat2374. 2, 64

[8] P. Gambardella, S. Stepanow, A. Dmitriev, J. Honolka, F. M. F. de Groot, M. Lingenfelder, S. S. Gupta, D. D. Sarma, P. Bencok, S. Stanescu, S. Clair, S. Pons, N. Lin, A. P. Seitsonen, H. Brune, J. V. Barth, and K. Kern: *Supramolecular con-*

trol of the magnetic anisotropy in two-dimensional high-spin Fe arrays at a metal interface. Nat. Mater. **8**, 189 (2009), doi:10.1038/nmat2376. 2, 64

[9] N. Lin, S. Stepanow, M. Ruben, and J. V. Barth: *Surface-Confined Supramolecular Coordination Chemistry*. in: Topics in Current Chemistry, Springer Berlin/Heidelberg (2009), doi:10.1007/128_2008_150. 2

[10] J. V. Barth: *Fresh perspectives for surface coordination chemistry*. Surf. Sci. **603**, 1533 (2009), doi:10.1016/j.susc.2008.09.049. 2

[11] M. Gottfried and H. Marbach: *Surface-Confined Coordination Chemistry with Porphyrins and Phthalocyanines: Aspects of Formation, Electronic Structure, and Reactivity*. Z. Phys. Chem. **223**, 53 (2009), doi:10.1524/zpch.2009.6024. 2, 3

[12] F. Buchner, V. Schwald, K. Comanici, H.-P. Steinrück, and H. Marbach: *Microscopic Evidence of the Metalation of a Free-Base Porphyrin Monolayer with Iron*. ChemPhysChem **8**, 241 (2007), doi:10.1002/cphc.200600698. 3

[13] J. M. Gottfried, K. Flechtner, A. Kretschmann, T. Lukasczyk, and H.-P. Steinrück: *Direct Synthesis of a Metalloporphyrin Complex on a Surface*. J. Am. Chem. Soc. **128**, 5644 (2006), doi:10.1021/ja0610333. 3, 64

[14] K. Flechtner, A. Kretschmann, H.-P. Steinrück, and J. M. Gottfried: *NO-Induced Reversible Switching of the Electronic Interaction between a Porphyrin-Coordinated Cobalt Ion and a Silver Surface*. J. Am. Chem. Soc. **129**, 12110 (2007), doi:10.1021/ja0756725. 3

[15] A. Scheybal, T. Ramsvik, R. Bertschinger, M. Putero, F. Nolting, and T. A. Jung: *Induced magnetic ordering in a molecular monolayer*. Chem. Phys. Lett. **411**, 214 (2005), doi:10.1016/j.cplett.2005.06.017. 3, 64

[16] C. Iacovita, M. V. Rastei, B. W. Heinrich, T. Brumme, J. Kortus, L. Limot, and J. P. Bucher: *Visualizing the spin of individual cobalt-phthalocyanine molecules*. Phys. Rev. Lett. **101**, 116602 (2008), doi:10.1103/PhysRevLett.101.116602. 3, 64

[17] J. H. Hubbell: *Photon cross section compilation activity in the U. S. in the range 1 keV to 100 GeV*. J. Phys. Colloques **32**, C4-14 (1971), doi:10.1051/jphyscol:1971403. 6

[18] J. Stöhr and H. König: *Determination of Spin- and Orbital-Moment Anisotropies in Transition Metals by Angle-Dependent X-Ray Magnetic Circular Dichroism*. Phys. Rev. Lett. **75**, 3748 (1995), doi:10.1103/PhysRevLett.75.3748. 13, 75

[19] J. Stöhr: *X-ray magnetic circular dichroism spectroscopy of transition metal thin*

films. J. Electron Spectrosc. Relat. Phenom. **75**, 253 (1995), doi:10.1016/0368-2048(95)02537-5. 13, 17, 18, 19, 75

[20] J Stöhr and H. C. Siegmann: *Magnetism From Fundamentals to Nanoscale Dynamics*. Springer Berlin/Heidelberg (2006), doi:10.1007/978-3-540-30283-4. 13

[21] J. L. Erskine and E. A. Stern: *Calculation of the $M_{2,3}$ magneto-optical absorption spectrum of ferromagnetic nickel*. Phys. Rev. B **12**, 5016 (1975), doi:10.1103/PhysRevB.12.5016. 14

[22] G. Schütz, W. Wagner, W. Wilhelm, P. Kienle, R. Zeller, R. Frahm, and G. Materlik: *Absorption of circularly polarized x rays in iron*. Phys. Rev. Lett. **58**, 737 (1987), doi:10.1103/PhysRevLett.58.737. 14

[23] G. Y. Guo: *What does the K-edge x-ray magnetic circular dichroism spectrum tell us?*. J. Phys.: Condens. Matter **8**, L747 (1996), doi:10.1088/0953-8984/8/49/005. 15, 95

[24] C. Sorg, N. Ponpandian, M. Bernien, K. Baberschke, H. Wende, and R. Q. Wu: *Induced magnetism of oxygen in surfactant-grown Fe, Co, and Ni monolayers*. Phys. Rev. B **73**, 64409 (2006), doi:10.1103/PhysRevB.73.064409. 15, 41, 42, 99

[25] B. T. Thole, P. Carra, F. Sette, and G. van der Laan: *X-Ray Circular-Dichroism as a Probe of Orbital Magnetization*. Phys. Rev. Lett. **68**, 1943 (1992), doi:10.1103/PhysRevLett.68.1943. 15

[26] P. Carra, B. T. Thole, M. Altarelli, and X. D. Wang: *X-Ray Circular Dichroism and Local Magnetic Fields*. Phys. Rev. Lett. **70**, 694 (1993), doi:10.1103/PhysRevLett.70.694. 15

[27] C. T. Chen, Y. U. Idzerda, H.-J. Lin, N. V. Smith, G. Meigs, E. Chaban, G. H. Ho, E. Pellegrin, and F. Sette: *Experimental Confirmation of the X-Ray Magnetic Circular Dichroism Sum Rules for Iron and Cobalt*. Phys. Rev. Lett. **75**, 152 (1995), doi:10.1103/PhysRevLett.75.152. 15, 17

[28] H. Ebert, J. Stöhr, S. S. P. Parkin, M. Samant, and A. Nilsson: *L-edge x-ray absorption in fcc and bcc Cu metal: Comparison of experimental and first-principles theoretical results*. Phys. Rev. B **53**, 16067 (1996), doi:10.1103/PhysRevB.53.16067. 17

[29] A. Scherz, H. Wende, K. Baberschke, J. Minár, D. Benea, and H. Ebert: *Relation between $L_{2,3}$ XMCD and the magnetic ground-state properties for the early 3d element V*. Phys. Rev. B **66**, 184401 (2002), doi:10.1103/PhysRevB.66.184401. 18

[30] M. O. Krause: *Atomic radiative and radiationless yields for K and L shells*. J. Phys. Chem. Ref. Data **8**, 307 (1979), doi:10.1063/1.555594. 21

[31] J Stöhr: *NEXAFS Spectroscopy*. Springer Berlin/Heidelberg (1992). 22

[32] R. Nakajima, J. Stöhr, and Y. U. Idzerda: *Electron-yield saturation effects in L-edge x-ray magnetic circular dichroism spectra of Fe, Co, and Ni*. Phys. Rev. B **59**, 6421 (1999), doi:10.1103/PhysRevB.59.6421. 23

[33] W. Gudat and C. Kunz: *Close Similarity between Photoelectric Yield and Photoabsorption Spectra in the Soft-X-Ray Range*. Phys. Rev. Lett. **29**, 169 (1972), doi:10.1103/PhysRevLett.29.169. 24

[34] M.-S. Liao, J. D. Watts, and M.-J. Huang: *Electronic Structure of Some Substituted Iron(II) Porphyrins. Are They Intermediate or High Spin?*. J. Phys. Chem. A **111**, 5927 (2007), doi:10.1021/jp070734z. 28

[35] M.-S. Liao, J. D. Watts, and M.-J. Huang: *Fe^{II} in Different Macrocycles: Electronic Structures and Properties*. J. Phys. Chem. A **109**, 7988 (2005), doi:10.1021/jp0581476. 28

[36] M.-S. Liao and S. Scheiner: *Electronic structure and bonding in metal porphyrins, metal=Fe, Co, Ni, Cu, Zn*. J. Chem. Phys. **117**, 205 (2002), doi:10.1063/1.1480872. 28, 69

[37] M.-S. Liao and S. Scheiner: *Electronic structure and bonding in unligated and ligated Fe^{II} porphyrins*. J. Chem. Phys. **116**, 3635 (2002), doi:10.1063/1.1447902. 28

[38] R. K. Hocking, E. C. Wasinger, F. M. F. de Groot, K. O. Hodgson, B. Hedman, and E. I. Solomon: *Fe L-edge XAS studies of $K_4[Fe(CN)_6]$ and $K_3[Fe(CN)_6]$: A direct probe of back-bonding*. J. Am. Chem. Soc. **128**, 10442 (2006), doi:10.1021/ja061802i. 28

[39] G. Frenking: *Understanding the nature of the bonding in transition metal complexes: from Dewar's molecular orbital model to an energy partitioning analysis of the metal-ligand bond*. J. Organomet. Chem. **635**, 9 (2001), doi:10.1016/S0022-328X(01)01154-8. 28

[40] A. S. Vinogradov, A. B. Preobrajenski, S. A. Krasnikov, T. Chassé, R. Szargan, A. Knop-Gericke, R. Schlögl, and P. Bressler: *X-Ray Absorption Evidence for the Back-Donation in Iron Cyanide Complexes*. Surf. Rev. Lett. **9**, 359 (2002), doi:10.1142/S0218625X02002270. 28, 79, 101

[41] R. K. Hocking, E. C. Wasinger, Y.-L. Yan, F. M. F. deGroot, F. A. Walker, K. O. Hodgson, B. Hedman, and E. I. Solomon: *Fe L-Edge X-ray Absorption Spectroscopy of Low-Spin Heme Relative to Non-heme Fe Complexes: Delocalization of Fe d-Electrons into the Porphyrin Ligand*. J. Am. Chem. Soc. **129**, 113 (2007), doi:10.1021/ja065627h. 28

[42] R. K. Hocking, S. D. George, Z. Gross, F. A. Walker, K. O. Hodgson, B. Hedman, and E. I. Solomon: *Fe L- and K-edge XAS of Low-Spin Ferric Corrole: Bonding and Reactivity Relative to Low-Spin Ferric Porphyrin*. Inorg. Chem. **48**, 1678 (2009), doi:10.1021/ic802248t. 28

[43] J. J. Yeh and I. Lindau: *Atomic subshell photoionization cross sections and asymmetry parameters: $1 \leq Z \leq 103$*. At. Data Nucl. Data Tables **32**, 1 (1985), doi:10.1016/0092-640X(85)90016-6. 30

[44] C. Sorg: *Magnetic Properties of 3d and 4f Ferromagnets Studied by X-Ray Absorption Spectroscopy*. Ph. D. thesis, Freie Universität Berlin, (2005). 37

[45] M. Bernien: *Spinfluktuationen in gekoppelten, magnetischen Schichten: eine temperaturabhängige Röntgenzirkulardichroismus-Studie*. Diploma thesis, Freie Universität Berlin (2004). 37

[46] M. A. MacDonald, F. Schaefers, R. Pohl, I. B. Poole, A. Gaupp, and F. M. Quinn: *A W:B_4C multilayer phase retarder for broadband polarization analysis of soft x-ray radiation*. Rev. Sci. Instrum. **79**, 025108 (2008), doi:10.1063/1.2841803. 39

[47] K. Heister, M. Zharnikov, M. Grunze, L. S. O. Johansson, and A. Ulman: *Characterization of X-ray Induced Damage in Alkanethiolate Monolayers by High-Resolution Photoelectron Spectroscopy*. Langmuir **17**, 8 (2001), doi:10.1021/la001101d. 40

[48] M. Zharnikov, W. Geyer, A. Gölzhäuser, S. Frey, and M. Grunze: *Modification of alkanethiolate monolayers on Au-substrate by low energy electron irradiation: Alkyl chains and the S/Au interface*. Phys. Chem. Chem. Phys. **1**, 3163 (1999), doi:10.1039/a902013f. 40

[49] S. Voss, M. Fonin, L. Burova, M. Burgert, Y. Dedkov, A. Preobrajenski, E. Goering, U. Groth, A. Kaul, and U. Ruediger: *Investigation of the stability of Mn_{12} single molecule magnets*. Appl. Phys. A: Mater. Sci. Process. **94**, 491 (2009), doi:10.1007/s00339-008-4911-6. 40

[50] P. Feulner, T. Niedermayer, K. Eberle, R. Schneider, D. Menzel, A. Baumer, E. Schmich, A. Shaporenko, Y. Tai, and M. Zharnikov: *Strong Temperature Dependence of Irradiation Effects in Organic Layers*. Phys. Rev. Lett. **93**, 178302 (2004), doi:10.1103/PhysRevLett.93.178302. 40

[51] M. Zharnikov and M. Grunze: *Modification of thiol-derived self-assembling monolayers by electron and x-ray irradiation: Scientific and lithographic aspects*. J. Vac. Sci. Technol. B **20**, 1793 (2002), doi:10.1116/1.1514665. 40

[52] S. Frey, H.-T. Rong, K. Heister, Y.-J. Yang, M. Buck, and M. Zharnikov: *Response of Biphenyl-Substituted Alkanethiol Self-Assembled Monolayers to Electron*

Irradiation: Damage Suppression and Odd–Even Effects. Langmuir **18**, 3142 (2002), doi:10.1021/la011288o. 40

[53] H. Henneken, F. Scholze, and G. Ulm: *Lack of proportionality of total electron yield and soft x-ray absorption coefficient*. J. Appl. Phys. **87**, 257 (2000), doi:10.1063/1.371854. 40

[54] B. Barbiellini and P. M. Platzman: *The healing mechanism for excited molecules near metallic surfaces*. New J. Phys. **8**, 8 (2006), doi:10.1088/1367-2630/8/2/020. 40

[55] H. L. Meyerheim, D. Sander, R. Popescu, W. Pan, I. Popa, and J. Kirschner: *Surfactant-Mediated Growth Revisited*. Phys. Rev. Lett. **99**, 116101 (2007), doi:10.1103/PhysRevLett.99.116101. 42

[56] X.-D. Liu, T. Iimori, K. Nakatsuji, and F. Komori: *Comment on "Surfactant-Mediated Growth Revisited"*. Phys. Rev. Lett. **100**, 089601 (2008), doi:10.1103/PhysRevLett.100.089601. 42

[57] H. L. Meyerheim, D. Sander, R. Popescu, W. Pan, I. Popa, and J. Kirschner: *Reply on "Surfactant-Mediated Growth Revisited"*. Phys. Rev. Lett. **100**, 089602 (2008), doi:10.1103/PhysRevLett.100.089602. 42

[58] X. Liu, T Iimori, K Nakatsuji, and F Komori: *Invasive growth of Co on $(\sqrt{2} \times 2\sqrt{2})R45°$ reconstructed O/Cu(001)*. Appl. Phys. Lett. **88**, 133102 (2006), doi:10.1063/1.2189190. 42

[59] R. Nünthel, T. Gleitsmann, P. Poulopoulos, A. Scherz, J. Lindner, E. Kosubek, C. Litwinski, Z. Li, H. Wende, K. Baberschke, S. Stolbov, and T. S. Rahman: *Epitaxial growth of Ni on Cu(001) with the assistance of O-surfactant and its magnetism compared to Ni/Cu(001)*. Surf. Sci. **531**, 53 (2003), doi:10.1016/S0039-6028(03)00438-2. 42, 43, 97, 99

[60] C. Kittel: *Einführung in die Festkörperphysik*. R. Oldenbourg Verlag (1999). 43, 96

[61] H. E. Stanley: *Introduction to Phase Transitions and Critical Phenomena*. Oxford: Clarendon Press (1971). 43, 97

[62] Jisang Hong, R. Q. Wu, J. Lindner, E. Kosubek, and K. Baberschke: *Manipulation of Spin Reorientation Transition by Oxygen Surfactant Growth: A Combined Theoretical and Experimental Approach*. Phys. Rev. Lett. **92**, 147202 (2004), doi:10.1103/PhysRevLett.92.147202. 43, 97

[63] D. Sander, W. Pan, S. Ouazi, J. Kirschner, W. Meyer, M. Krause, S. Müller, L. Hammer, and K. Heinz: *Reversible H-Induced Switching of the Magnetic*

Easy Axis in Ni/Cu(001) Thin Films. Phys. Rev. Lett. **93**, 247203 (2004), doi:10.1103/PhysRevLett.93.247203. 43, 97

[64] V. Ksenofontov, G. Levchenko, H. Spiering, P. Gütlich, J.-F. Létard, Y. Bouhedja, and O. Kahn: *Spin crossover behavior under pressure of Fe(PM-L)$_2$(NCS)$_2$ compounds with substituted 2'-pyridylmethylene 4-anilino ligands*. Chem. Phys. Lett. **294**, 545 (1998), doi:10.1016/S0009-2614(98)00901-4. 45

[65] M. Hostettler, K. W. Törnroos, D. Chernyshov, B. Vangdal, and H.-B. Bürgi: *Challenges in Engineering Spin Crossover: Structures and Magnetic Properties of Six Alcohol Solvates of Iron(II) Tris(2-picolylamine) Dichloride*. Angew. Chem. Int. Ed. **43**, 4589 (2004), doi:10.1002/anie.200460736. 45

[66] L. Cambi and L. Szegö: *Über die magnetische Susceptibilität der komplexen Verbindungen*. Ber. Deutsch. Chem. Ges. **64**, 2591 (1931), doi:10.1002/cber.19310641002. 45

[67] L. Cambi and L. Malatesta: *Magnetismus und Polymorphie innerer Komplexsalze: Eisensalze der Dithiocarbamidsäuren*. Ber. Deutsch. Chem. Ges. **70**, 2067 (1937), doi:10.1002/cber.19370701006. 45

[68] J. A. Real, A. B. Gaspar, V. Niel, and M. C. Muñoz: *Communication between iron(II) building blocks in cooperative spin transition phenomena*. Coord. Chem. Rev. **236**, 121 (2003), doi:10.1016/S0010-8545(02)00220-5. 46

[69] K. S. Murray and C. J. Kepert: *Cooperativity in Spin Crossover Systems: Memory, Magnetism and Microporosity*. in: Spin Crossover in Transition Metal Compounds I, Springer Berlin/Heidelberg (2004), doi:10.1007/b40394-9. 46

[70] S. Decurtins, P. Gütlich, C. P. Köhler, H. Spiering, and A. Hauser: *Light-induced excited spin state trapping in a transition-metal complex: The hexa-1-propyltetrazole-iron (II) tetrafluoroborate spin-crossover system*. Chem. Phys. Lett. **105**, 1 (1984), doi:10.1016/0009-2614(84)80403-0. 46

[71] S. Decurtins, P. Gütlich, K. M. Hasselbach, A. Hauser, and H. Spiering: *Light-induced excited-spin-state trapping in iron(II) spin-crossover systems. Optical spectroscopic and magnetic susceptibility study*. Inorg. Chem. **24**, 2174 (1985), doi:10.1021/ic00208a013. 46

[72] J.-F. Létard, Ph. Guionneau, O. Nguyen, J. S. Costa, S. Marcén, G. Chastanet, M. Marchivie, and L. Goux-Capes: *A Guideline to the Design of Molecular-Based Materials with Long-Lived Photomagnetic Lifetimes*. Chem. Eur. J. **11**, 4582 (2005), doi:10.1002/chem.200500112. 46

[73] V. Ksenofontov, H. Spiering, S. Reiman, Y. Garcia, A. B. Gaspar, N. Moliner, J. A. Real, and P. Gütlich: *Direct monitoring of spin state in dinuclear iron(II)*

coordination compounds. Chem. Phys. Lett. **348**, 381 (2001), doi:10.1016/S0009-2614(01)01114-9. 46

[74] A. B. Gaspar, V. Ksenofontov, J. A. Real, and Ph. Gütlich: *Coexistence of spin-crossover and antiferromagnetic coupling phenomena in the novel dinuclear Fe(II) complex [Fe(dpa)(NCS)$_2$]$_2$bpym*. Chem. Phys. Lett. **373**, 385 (2003), doi:10.1016/S0009-2614(03)00560-8. 46

[75] C. Carbonera, J. S. Costa, V. A. Money, J. Elhaïk, J. A. K. Howard, M. A. Halcrow, and J.-F. Létard: *Photomagnetic properties of iron(ii) spin crossover complexes of 2,6-dipyrazolylpyridine and 2,6-dipyrazolylpyrazine ligands*. Dalton Trans., 3058 (2006), doi:10.1039/b601366j. 46, 59

[76] A. Bhattacharjee, J. Kusz, V. Ksenofontov, K. H. Sugiyarto, H. A. Goodwin, and P. Gütlich: *X-ray powder diffraction and LIESST-effect of the spin transition material [Fe(bpp)$_2$](NCS)$_2$ · 2H$_2$O*. Chem. Phys. Lett. **431**, 72 (2006), doi:10.1016/j.cplett.2006.09.052. 46

[77] M. Marchivie, P. Guionneau, J. A. K. Howard, G. Chastanet, J.-F. Létard, A. E. Goeta, and D. Chasseau: *Structural Characterization of a Photoinduced Molecular Switch*. J. Am. Chem. Soc. **124**, 194 (2002), doi:10.1021/ja016980k. 46, 47

[78] E. J. MacLean, C. M. McGrath, Ch. J. O'Connor, C. Sangregorio, J. M. W. Seddon, E. Sinn, F. E. Sowrey, S. J. Teat, A. E. Terry, G. B. M. Vaughan, and N. A. Young: *Structural Study of the Thermal and Photochemical Spin States in the Spin Crossover Complex [Fe(phen)$_2$(NCSe)$_2$]*. Chem. Eur. J. **9**, 5314 (2003), doi:10.1002/chem.200304865. 46, 47, 49

[79] Ch. Cartier dit Moulin, P. Rudolf, A. M. Flank, and C. T. Chen: *Spin transition evidenced by soft x-ray absorption spectroscopy*. J. Phys. Chem. **96**, 6196 (1992), doi:10.1021/j100194a021. 46, 48

[80] D. Collison, C. D. Garner, C. M. McGrath, J. F. W. Mosselmans, M. D. Roper, J. M. W. Seddon, E. Sinn, and N. A. Young: *Soft X-ray induced excited spin state trapping and soft X-ray photochemistry at the iron $L_{2,3}$ edge in [Fe(phen)$_2$(NCS)$_2$)] and [Fe(phen)$_2$(NCSe)$_2$] (phen = 1,10-phenanthroline)*. Dalton Trans., 4371 (1997), doi:10.1039/a703728g. 46, 47, 48

[81] J.-J. Lee, H.-s. Sheu, C.-R. Lee, J.-M. Chen, J.-F. Lee, C.-C. Wang, C.-H. Huang, and Y. Wang: *X-ray Absorption Spectroscopic Studies on Light-Induced Excited Spin State Trapping of an Fe(II) Complex*. J. Am. Chem. Soc. **122**, 5742 (2000), doi:10.1021/ja9943290. 46, 48

[82] L. X. Chen, Z. Wang, J. K. Burdett, P. A. Montano, and J. R. Norris: *X-ray Ab-*

sorption Studies on Electronic Spin State Transitions of Fe(II) Complexes in Different Media. J. Phys. Chem. **99**, 7958 (1995), doi:10.1021/j100020a018. 46

[83] R. Boča, M. Vrbová, R. Werner, and W. Haase: *Spin crossover in iron(II) tris(2-(2-pyridyl)benzimidazole) complex monitored by the variable temperature EXAFS*. Chem. Phys. Lett. **328**, 188. (2000), doi:10.1016/S0009-2614(00)00902-7. 46

[84] O. Kahn and C. J. Martinez: *Spin-Transition Polymers: From Molecular Materials Toward Memory Devices*. Science **279**, 44. (1998), doi:10.1126/science.279.5347.44. 46

[85] W. Xu, M. Dong, S. Vazquez-Campos, H. Gersen, E. Lagsgaard, I. Stensgaard, M. Crego-Calama, D. N. Reinhoudt, T. R. Linderoth, and F. Besenbacher: *Enhanced Stability of Large Molecules Vacuum-Sublimated onto Au(111) Achieved by Incorporation of Coordinated Au-Atoms*. J. Am. Chem. Soc. **129**, 10624 (2007), doi:10.1021/ja0725448. 46

[86] S. Rauschenbach, F. L. Stadler, E. Lunedei, N. Malinowski, S. Koltsov, G. Costantini, and K. Kern: *Electrospray Ion Beam Deposition of Clusters and Biomolecules*. Small **2**, 540 (2006), doi:10.1002/smll.200500479. 46

[87] S. Rauschenbach: *Electrospray Ion Beam Deposition and Mass Spectroscopy of Nonvolatile Molecules and Nanomaterials*. Ph. D. thesis, École Polytechnique Fédérale de Lausane, (2007), doi:10.5075/epfl-thesis-3958. 46

[88] L. Grill, I. Stass, K.-H. Rieder, and F. Moresco: *Preparation of self-ordered molecular layers by pulse injection*. Surf. Sci. **600**, L143 (2006), doi:10.1016/j.susc.2006.03.040. 46

[89] H. Tanaka and T. Kawai: *Scanning tunneling microscopy imaging and manipulation of DNA oligomer adsorbed on Cu(111) surfaces by a pulse injection method*. J. Vac. Sci. Technol. B **15**, 602 (1997), doi:10.1116/1.589299. 46

[90] M. Matsuda and H. Tajima: *Thin Film of a Spin Crossover Complex [Fe(dpp)$_2$](BF$_4$)$_2$*. Chem. Lett. **36**, 700 (2007), doi:10.1246/cl.2007.700. 46

[91] G. E. Poirier: *Characterization of Organosulfur Molecular Monolayers on Au(111) using Scanning Tunneling Microscopy*. Chem. Rev. **97**, 1117 (1997), doi:10.1021/cr960074m. 47, 54, 58

[92] J. C. Love, L. A. Estroff, J. K. Kriebel, R. G. Nuzzo, and G. M. Whitesides: *Self-Assembled Monolayers of Thiolates on Metals as a Form of Nanotechnology*. Chem. Rev. **105**, 1103 (2005), doi:10.1021/cr0300789. 47, 54, 58

[93] P. Cyganik, M. Buck, T. Strunskus, A. Shaporenko, J. D. E. T. Wilton-Ely, M. Zharnikov, and C. Wöll: *Competition as a Design Concept: Polymorphism in*

Self-Assembled Monolayers of Biphenyl-Based Thiols. J. Am. Chem. Soc. **128**, 13868 (2006), doi:10.1021/ja0640647. 47, 54, 58

[94] T. M. Willey, J. D. Fabbri, J. R. I. Lee, P. R. Schreiner, A. A. Fokin, B. A. Tkachenko, N. A. Fokina, J. E. P. Dahl, R. M. K. Carlson, A. L. Vance, W. Yang, L. J. Terminello, T. van Buuren, and N. A. Melosh: *Near-Edge X-ray Absorption Fine Structure Spectroscopy of Diamondoid Thiol Monolayers on Gold*. J. Am. Chem. Soc. **130**, 10536 (2008), doi:10.1021/ja711131e. 47, 54, 58

[95] J. F. Létard, O. Nguyen, H. Soyer, C. Mingotaud, P. Delhaes, and O. Kahn: *First Evidence of the LIESST Effect in a Langmuir–Blodgett Film*. Inorg. Chem. **38**, 3020 (1999), doi:10.1021/ic990259m. 47

[96] Y. Bodenthin, G. Schwarz, Z. Tomkowicz, M. Lommel, Th. Geue, W. Haase, H. Möhwald, U. Pietsch, and D. G. Kurth: *Spin-crossover phenomena in extended multi-component metallo-supramolecular assemblies*. Coord. Chem. Rev. **253**, 2414 (2009), doi:10.1016/j.ccr.2008.10.019. 47

[97] E. König and K. Madeja: *Unusual Magnetic Behaviour of Some Iron(II)-Bis- (1,10-phenanthroline) Complexes*. Chem. Comm. **3**, 61 (1966), doi:10.1039/C19660000061. 47

[98] E. W. Müller, H. Spiering, and P. Gütlich: *Spin transition in [Fe(phen)$_2$(NCS)$_2$] and [Fe(bipy)$_2$(NCS)$_2$]: Hysteresis and effect of crystal quality*. Chem. Phys. Lett. **93**, 567 (1982), doi:10.1016/0009-2614(82)83731-7. 47

[99] V. Briois, Ch. Cartier dit Moulin, Ph. Sainctavit, Ch. Brouder, and A.-M. Flank: *Full Multiple Scattering and Crystal Field Multiplet Calculations Performed on the Spin Transition FeII(phen)$_2$(NCS)$_2$ Complex at the Iron K and L$_{2,3}$ X-ray Absorption Edges*. J. Am. Chem. Soc. **117**, 1019 (1995), doi:10.1021/ja00108a018. 49

[100] B. T. Thole and G. van der Laan: *Branching ratio in x-ray absorption spectroscopy*. Phys. Rev. B **38**, 3158 (1988), doi:10.1103/PhysRevB.38.3158. 49

[101] G. van der Laan and I. W. Kirkman: *The 2p absorption spectra of 3d transition metal compounds in tetrahedral and octahedral symmetry*. J. Phys.: Condens. Matter **4**, 4189 (1992), doi:10.1088/0953-8984/4/16/019. 49, 69, 83

[102] E. König: *Nature and dynamics of the spin-state interconversion in metal complexes*. in: Complex Chemistry, Springer Berlin/Heidelberg (1991), doi:10.1007/3-540-53499-7. 49

[103] C. Kolczewski, R. Püttner, M. Martins, A. S. Schlachter, G. Snell, M. M. Sant'Anna, K. Hermann, and G. Kaindl: *Spectroscopic analysis of small organic molecules: A comprehensive near-edge x-ray-absorption fine-structure*

study of C_6-ring-containing molecules. J. Chem. Phys. **124**, 034302 (2006), doi:10.1063/1.2139674. 50, 69

[104] M. Piantek, G. Schulze, M. Koch, K. J. Franke, F. Leyssner, A. Krüger, C. Navío, J. Miguel, M. Bernien, M. Wolf, W. Kuch, P. Tegeder, and J. I. Pascual: *Reversing the Thermal Stability of a Molecular Switch on a GoldSurface: Ring-Opening Reaction of Nitrospiropyran*. J. Am. Chem. Soc. **131**, 12729 (2009), doi:10.1021/ja901238p. 50, 69

[105] L. C. Mayor, A. Saywell, G. Magnano, C. J. Satterley, J. Schnadt, and J. N. O'Shea: *Adsorption of a Ru(II) dye complex on the Au(111) surface: Photoemission and scanning tunneling microscopy*. J. Chem. Phys. **130**, 164704 (2009), doi:10.1063/1.3122685. 53

[106] G. Liu, A. Klein, A. Thissen, and W. Jaegermann: *Electronic properties and interface characterization of phthalocyanine and Ru-polypyridine dyes on TiO_2 surface*. Surf. Sci. **539**, 37 (2003), doi:10.1016/S0039-6028(03)00721-0. 53

[107] R. M. Abrudan: *Growth, Structure and Magnetic Properties of Single Crystalline Fe/CoO/Ag(001) Bilayers*. Ph. D. thesis, Freie Universität Berlin, (2007). 54

[108] R. Shantyr: *Scanning tunneling microscopy/scanning tunneling spectroscopy on growth, atomic and electronic structure of Co oxide and Mn oxide films on Ag(001)*. Ph. D. thesis, Martin-Luther-Universität Halle-Wittenberg, (2004). 54

[109] J. Repp, S. Fölsch, G. Meyer, and K.-H. Rieder: *Ionic Films on Vicinal Metal Surfaces: Enhanced Binding due to Charge Modulation*. Phys. Rev. Lett. **86**, 252 (2001), doi:10.1103/PhysRevLett.86.252. 54

[110] A. Riemann, S. Fölsch, and K.-H. Rieder: *Epitaxial growth of alkali halides on stepped metal surfaces*. Phys. Rev. B **72**, 125423 (2005), doi:10.1103/PhysRevB.72.125423. 54

[111] S. Zöphel: *Der Aufbau eines Tieftemperatur-Rastertunnelmikroskops und Strukturuntersuchungen auf vicinalen Kupferoberflächen*. Ph. D. thesis, Freie Universität Berlin, (2000). 54

[112] D. Ball: *Röntgenspektroskopie an Spin-Crossover-Molekülen auf Metalloberflächen*. Diploma thesis, Freie Universität Berlin (2008). 55

[113] K. Student: *Monoanionische terdentate Stickstoffliganden und ihre Eisenkomplexe*. Diploma thesis, Technische Universität Berlin (2008). 55

[114] M. A. Halcrow: *The spin-states and spin-transitions of mononuclear iron(II) complexes of nitrogen-donor ligands*. Polyhedron **26**, 3523 (2007), doi:10.1016/j.poly.2007.03.033. 59

[115] J. Elhaïk, V. A. Money, S. A. Barrett, C. A. Kilner, I. R. Evans, and M. A. Halcrow: *The spin-states and spin-crossover behaviour of iron(II) complexes of 2,6-dipyrazol-1-ylpyrazine derivatives*. Dalton Trans., 2053 (2003), doi:10.1039/b210368k. 59

[116] J. M. Holland, J. A. McAllister, C. A. Kilner, M. Thornton-Pett, A. J. Bridgeman, and M. A. Halcrow: *Stereochemical effects on the spin-state transition shown by salts of $[FeL_2]^{2+}$ [L = 2,6-di(pyrazol-1-yl)pyridine]*. Dalton Trans., 548 (2002), doi:10.1039/b108468m. 59

[117] R. Chandrasekar, F. Schramm, O. Fuhr, and M. Ruben: *An Iron(II) Spin-Transition Compound with Thiol Anchoring Groups*. Eur. J. Inorg. Chem. **2008**, 2649 (2008), doi:10.1002/ejic.200800212. 59

[118] M. Haryono: *Spin-schaltbare Eisen(II)-Komplexe für die Verankerung auf Oberflächen*. Ph. D. thesis, Technische Universität Berlin, (2008). 59

[119] K. Heister, M. Zharnikov, M. Grunze, and L. S. O. Johansson: *Adsorption of Alkanethiols and Biphenylthiols on Au and Ag Substrates: A High-Resolution X-ray Photoelectron Spectroscopy Study*. J. Phys. Chem. B **105**, 4058 (2001), doi:10.1021/jp010127q. 60

[120] D. G. Castner, K. Hinds, and D. W. Grainger: *X-ray Photoelectron Spectroscopy Sulfur 2p Study of Organic Thiol and Disulfide Binding Interactions with Gold Surfaces*. Langmuir **12**, 5083 (1996), doi:10.1021/la960465w. 60

[121] C. Shen, M. Haryono, A. Grohmann, M. Buck, T. Weidner, N. Ballav, and M. Zharnikov: *Self-Assembled Monolayers of a Bis(pyrazol-1-yl)pyridine-Substituted Thiol on Au(111)*. Langmuir **24**, 12883 (2008), doi:10.1021/la8019974. 60

[122] A. Shaporenko, A. Terfort, M. Grunze, and M. Zharnikov: *A detailed analysis of the photoemission spectra of basic thioaromatic monolayers on noble metal substrates*. J. Electron Spectrosc. Relat. Phenom. **151**, 45 (2006), doi:10.1016/j.elspec.2005.10.008. 60

[123] Y. W. Yang and L. J. Fan: *High-Resolution XPS Study of Decanethiol on Au(111): Single Sulfur–Gold Bonding Interaction*. Langmuir **18**, 1157 (2002), doi:10.1021/la010591m. 60

[124] T. A. Jung, R. R. Schlittler, and J. K. Gimzewski: *Conformational identification of individual adsorbed molecules with the STM*. Nature **386**, 696 (1997), doi:10.1038/386696a0. 64

[125] W. Auwärter, A. Weber-Bargioni, A. Riemann, A. Schiffrin, O. Gröning, R. Fasel, and J. V. Barth: *Self-assembly and conformation of tetrapyridyl-porphyrin*

molecules on Ag(111). J. Chem. Phys. **124**, 194708 (2006), doi:10.1063/1.2194541. 64

[126] L. Ramoino, M. von Arx, S. Schintke, A. Baratoff, H.-J. Güntherodt, and T.A. Jung: *Layer-selective epitaxial self-assembly of porphyrins on ultrathin insulators*. Chem. Phys. Lett. **417**, 22 (2006), doi:10.1016/j.cplett.2005.10.006. 64

[127] F. Buchner, K. Comanici, N. Jux, H.-P. Steinrück, and H. Marbach: *Polymorphism of Porphyrin Molecules on Ag(111) and How to Weave a Rigid Monolayer*. J. Phys. Chem. C **111**, 13531 (2007), doi:10.1021/jp074448z. 64, 66

[128] A. Scarfato, S.-H. Chang, S. Kuck, J. Brede, G. Hoffmann, and R. Wiesendanger: *Scanning tunneling microscope study of iron(II) phthalocyanine growth on metals and insulating surfaces*. Surf. Sci. **602**, 677 (2008), doi:10.1016/j.susc.2007.11.011. 64

[129] L. Gao, Q. Liu, Y. Y. Zhang, N. Jiang, H. G. Zhang, Z. H. Cheng, W. F. Qiu, S. X. Du, Y. Q. Liu, W. A. Hofer, and H.-J. Gao: *Constructing an Array of Anchored Single-Molecule Rotors on Gold Surfaces*. Phys. Rev. Lett. **101**, 197209 (2008), doi:10.1103/PhysRevLett.101.197209. 64

[130] L. Grill, M. Dyer, L. Lafferentz, M. Persson, M. V. Peters, and S. Hecht: *Nanoarchitectures by covalent assembly of molecular building blocks*. Nat. Nano. **2**, 687 (2007), doi:10.1038/nnano.2007.346. 64

[131] F. Buchner, K. Flechtner, Y. Bai, E. Zillner, I. Kellner, H.-P. Steinrück, H. Marbach, and J. M. Gottfried: *Coordination of Iron Atoms by Tetraphenylporphyrin Monolayers and Multilayers on Ag(111) and Formation of Iron-Tetraphenylporphyrin*. J. Phys. Chem. C **112**, 15458 (2008), doi:10.1021/jp8052955. 64

[132] W. Auwärter, A. Weber-Bargioni, S. Brink, A. Riemann, A. Schiffrin, M. Ruben, and J. V. Barth: *Controlled Metalation of Self-Assembled Porphyrin Nanoarrays in Two Dimensions*. ChemPhysChem **8**, 250 (2007), doi:10.1002/cphc.200600675. 64

[133] A. Kretschmann, M.-M. Walz, K. Flechtner, H.-P. Steinrück, and J. M. Gottfried: *Tetraphenylporphyrin picks up zinc atoms from a silver surface*. ChemComm, 568 (2007), doi:10.1039/b614427f. 64

[134] A. Weber-Bargioni, J. Reichert, A. P. Seitsonen, W. Auwärter, A. Schiffrin, and J. V. Barth: *Interaction of Cerium Atoms with Surface-Anchored Porphyrin Molecules*. J. Phys. Chem. C **112**, 3453 (2008), doi:10.1021/jp076961i. 64

[135] A. Weber-Bargioni, W. Auwärter, F. Klappenberger, J. Reichert, S. Lefrançois, T. Strunskus, Ch. Wöll, A. Schiffrin, Y. Pennec, and J. V. Barth: *Visu-*

alizing the Frontier Orbitals of a Conformationally Adapted Metalloporphyrin. ChemPhysChem **9**, 89 (2008), doi:10.1002/cphc.200700600. 66

[136] F. Klappenberger, A. Weber-Bargioni, W. Auwärter, M. Marschall, A. Schiffrin, and J. V. Barth: *Temperature dependence of conformation, chemical state, and metal-directed assembly of tetrapyridyl-porphyrin on Cu(111)*. J. Chem. Phys. **129**, 214702 (2008), doi:10.1063/1.3021291. 66

[137] K. M. Kadish, K. M. Smith, and R. Guilard (Eds.): *The Porphyrin Handbook*. Vol. 5, Academic Press (1999). 67, 69

[138] G. van der Laan and B. T. Thole: *Strong magnetic x-ray dichroism in 2p absorption spectra of 3d transition-metal ions*. Phys. Rev. B **43**, 13401 (1991), doi:10.1103/PhysRevB.43.13401. 69, 83

[139] F. M. F. de Groot, J. C. Fuggle, B. T. Thole, and G. A. Sawatzky: *2p x-ray absorption of 3d transition-metal compounds: An atomic multiplet description including the crystal field*. Phys. Rev. B **42**, 5459 (1990), doi:10.1103/PhysRevB.42.5459. 69, 83

[140] D. Wegner, private communication. 73

[141] D. Bovenschen: *Röntgenabsorptionsuntersuchungen an Eisenporphyrinen*. Diploma thesis, Universität Duisburg-Essen (2009). 82

[142] H. Wende, M. Bernien, J. Luo, C. Sorg, N. Ponpandian, J. Kurde, J. Miguel, M. Piantek, X. Xu, P. Eckhold, W. Kuch, K. Baberschke, P. M. Panchmatia, B. Sanyal, P. M. Oppeneer, and O. Eriksson: *Substrate-induced magnetic ordering and switching of iron porphyrin molecules*. Nat. Mater. **6**, 516 (2007), doi:10.1038/nmat1932. 86, 93, 105, 112

[143] S. Narioka, H. Ishii, Y. Ouchi, T. Yokoyama, T. Ohta, and K. Seki: *XANES Spectroscopic Studies of Evaporated Porphyrin Films: Molecular Orientation and Electronic Structure*. J. Phys. Chem. **99**, 1332 (1995), doi:10.1021/j100004a038. 89

[144] P. Bruno: in: Magnetic Thin Films, Multilayers and Surfaces, (1992). 93

[145] K. Baberschke: *The magnetism of nickel monolayers*. Appl. Phys. A: Mater. Sci. Process. **62**, 417 (1996), doi:10.1007/bf01567112. 93

[146] A. Scherz, C. Sorg, M. Bernien, N. Ponpandian, K. Baberschke, H. Wende, and P. J. Jensen: *Importance of giant spin fluctuations in two-dimensional magnetic trilayers*. Phys. Rev. B **72**, 054447 (2005), doi:10.1103/PhysRevB.72.054447. 97

[147] A. Ney, A. Scherz, P. Poulopoulos, K. Lenz, H. Wende, K. Baberschke, F. Wilhelm, and N. B. Brookes: *Clarification of contesting results for*

the total magnetic moment of Ni/Cu(001). Phys. Rev. B **65**, 024411 (2001), doi:10.1103/PhysRevB.65.024411. 99

[148] A. Ney, K. Lenz, P. Poulopoulos, and K. Baberschke: *Absolute magnetometry on ultrathin 3d-metal films by UHV-SQUID*. J. Magn. Magn. Mater. **240**, 343 (2002), doi:10.1016/S0304-8853(01)00794-6. 99

[149] T. Yokoyama, K. Amemiya, M. Miyachi, Y. Yonamoto, D. Matsumura, and T. Ohta: *K-edge magnetic circular dichroism of O in CO/Ni/Cu(001): Dependence on substrate magnetic anisotropy and its interpretation*. Phys. Rev. B **62**, 14191 (2000), doi:10.1103/PhysRevB.62.14191. 99

[150] M. Bernien, J. Miguel, C. Weis, Md. E. Ali, J. Kurde, B. Krumme, P. M. Panchmatia, B. Sanyal, M. Piantek, P. Srivastava, K. Baberschke, P. M. Oppeneer, O. Eriksson, W. Kuch, and H. Wende: *Tailoring the Nature of Magnetic Coupling of Fe-Porphyrin Molecules to Ferromagnetic Substrates*. Phys. Rev. Lett. **102**, 047202 (2009), doi:10.1103/PhysRevLett.102.047202. 101

[151] M. S. Seehra and T. M. Giebultowicz: *Magnetic structures of fcc systems with nearest-neighbor and next-nearest-neighbor exchange interactions*. Phys. Rev. B **38**, 11898 (1988), doi:10.1103/PhysRevB.38.11898. 105

List of Acronyms

AEY	Auger electron yield
AFM	antiferromagnetic
AO	atomic orbital
BESSY	Helmholtz-Zentrum Berlin für Materialien und Energie (formerly Berliner Elektronenspeicherring-Gesellschaft für Synchrotronstrahlung mbH)
bp	2,5-bis(2-pyridyl)pyrrole
bpp	2,6-bis(pyrazol-1-yl)pyridine
bppm	2,6-bis(1H-pyrazol-1-yl)-4-(hydroxymethyl)pyridine
bppmc	2,6-bis(1H-pyrazol-1-yl)pyridine-4-(N-(2-mercaptoethyl) carboxamide
CCD	charge-coupled device
CFT	crystal field theory
CMA	cylindrical mirror analyzer
DFT	density functional theory
ESRF	European Synchrotron Radiation Facility
EXAFS	extended X-ray absorption fine structure
FM	ferromagnetic
HMA	hemispherical mirror analyzer
HS	high spin
LEED	low-energy electron diffraction
LFT	ligand field theory
LIESST	light-induced excited spin-state trapping
LS	low spin
MEED	medium energy electron diffraction
ML	monolayer
MO	molecular orbital

NEXAFS	near-edge X-ray absorption fine structure
OEP	2,3,7,8,12,13,17,18-octaethylporphyrin
PEY	partial electron yield
phen	1,10-phenanthroline
SAM	self-assembled monolayer
STM	scanning tunneling microscope
SRT	spin-reorientation transition
TEY	total electron yield
TPP	meso-tetraphenylporphyrin
TtMP	5,10,15,20-tetrakis(2,4,6-trimethylphenyl)porphyrin
UHV	ultra high vacuum
XA	X-ray absorption
XAS	X-ray absorption spectroscopy
XMCD	X-ray magnetic circular dichroism
XNLD	X-ray natural linear dichroism
XPS	X-ray photoelectron spectroscopy

LIST OF PUBLICATIONS

2009

M. Bernien, J. Miguel, C. Weis, Md. E. Ali, J. Kurde, B. Krumme, P. M. Panchmatia, B. Sanyal, M. Piantek, P. Srivastava, K. Baberschke, P. M. Oppeneer, O. Eriksson, W. Kuch, and H. Wende: *Tailoring the Nature of Magnetic Coupling of Fe-Porphyrin Molecules to Ferromagnetic Substrates*. Phys. Rev. Lett. **102**, 047202, doi:10.1103/PhysRevLett.102.047202.

J. Miguel, R. Abrudan, M. Bernien, M. Piantek, C. Tieg, J. Kirschner, and W. Kuch: *Magnetic domain coupling study in single-crystalline Fe/CoO bilayers*. J. Phys.: Condens. Matter **21**, 185004, doi:10.1103/PhysRevB.65.140408.

M. Piantek, G. Schulze, M. Koch, K. J. Franke, F. Leyssner, A. Krüger, C. Navío, J. Miguel, M. Bernien, M. Wolf, W. Kuch, P. Tegeder, and J. I. Pascual: *Reversing the Thermal Stability of a Molecular Switch on a GoldSurface: Ring-Opening Reaction of Nitrospiropyran*. J. Am. Chem. Soc. **131**, 12729, doi:10.1021/ja901238p.

2008

M. Piantek, J. Miguel, M. Bernien, C. Navío, A. Krüger, B. Priewisch, K. Rück-Braun, and W. Kuch: *Adsorption of carboxymethylester-azobenzene on copper and gold single crystal surfaces*. Appl. Phys. A **93**, 261, doi:10.1007/s00339-008-4825-3.

Y. Luo, M. Piantek, J. Miguel, M. Bernien, W. Kuch, and R. Haag: *In-situ formation and detailed analysis of imine bonds for the construction of conjugated aromatic monolayers on Au(111)*. Appl. Phys. A **93**, 293, doi:10.1007/s00339-008-4824-4.

J. Miguel, M. Bernien, D. Bayer, J. Sánchez-Barriga, F. Kronast, M. Aeschlimann, H. A. Dürr, and W. Kuch: *A new sample holder for laser-excited pump-probe magnetic measurements on a Focus photoelectron emission microscope*. Rev. Sci. Instrum. **79**, 033702, doi:10.1063/1.2884709.

R. Abrudan, J. Miguel, M. Bernien, C. Tieg, M. Piantek, J. Kirschner, and W. Kuch: *Structural and magnetic properties of epitaxial Fe/CoO bilayers on Ag(001)*. Phys. Rev. B **77**, 014411, doi:10.1103/PhysRevB.77.014411.

2007

H. Wende, M. Bernien, J. Luo, C. Sorg, N. Ponpandian, J. Kurde, J. Miguel, M. Piantek, X. Xu, P. Eckhold, W. Kuch, K. Baberschke, P. M. Panchmatia, B. Sanyal, P. M. Oppeneer, and O. Eriksson: *Substrate-induced magnetic ordering and switching of iron porphyrin molecules*. Nat. Mater. **6**, 516, doi:10.1038/nmat1932.

M. Bernien, X. Xu, J. Miguel, M. Piantek, Ph. Eckhold, J. Luo, J. Kurde, W. Kuch, K. Baberschke, H. Wende, and P. Srivastava: *Fe-porphyrin monolayers on ferromagnetic substrates: Electronic structure and magnetic coupling strength*. Phys. Rev. B **76**, 214406, doi:10.1103/PhysRevB.76.214406.

2006

C. Sorg, N. Ponpandian, M. Bernien, K. Baberschke, H. Wende, and R. Q. Wu: *Induced magnetism of oxygen in surfactant-grown Fe, Co, and Ni monolayers*. Phys. Rev. B **73**, 64409, doi:10.1103/PhysRevB.73.064409.

2005

A. Scherz, C. Sorg, M. Bernien, N. Ponpandian, K. Baberschke, H. Wende, and P. J. Jensen: *Importance of giant spin fluctuations in two-dimensional magnetic trilayers*. Phys. Rev. B **72**, 054447, doi:10.1103/PhysRevB.72.054447.

P. J. Jensen, C. Sorg, A. Scherz, M. Bernien, K. Baberschke, and H. Wende: *Comment on "Magnetic Phase Transition in Co/Cu/Ni/Cu(100) and Co/Fe/Ni/Cu(100)"*. Phys. Rev. Lett. **94**, 039703, doi:10.1103/PhysRevLett.94.039703.

ACKNOWLEDGMENTS

First and foremost, I want to thank *Prof. Dr. Wolfgang Kuch*, who has successfully supervised this work. His competence, knowledge, and his ability to discuss physical problems down to the very details were for me precious. I am very thankful to him for opening an opportunity for me to work in his group and for giving me the freedom to realize many of the experiments I was dreaming up.

I want to thank *Prof. Dr. Heiko Wende* for promoting the porphyrin project right from the beginning, for continuing the project after he became professor at the University Duisburg-Essen, and for establishing the fruitful collaboration with the theory group in Uppsala. In this context, I also would like to thank *Prof. Dr. Klaus Baberschke* for his help initializing the project.

I thank *Prof. Dr. Martin Weinelt* for his willingness to co-assess this thesis.

I am deeply indebted to *Dr. Jorge Miguel* for his help during all stages of this work. I learned a lot from his scientific experience. Thank you for all the experiments we did together, for working until death, taking a shower, and then doing another shift, for being always there to discuss about physics and to solve problems concerning the experiment and many more, for being a true friend.

Marten Piantek, the third musketeer. The three of us together fought our way through many beamtimes, carrying out repairs of the equipment on the fly, and fighting the noise in the spectra. You are somebody to count on. I enjoyed our discussion about physics and other stuff.

David Ball, for contributing to the studies on SCO complexes during his diploma thesis.

Working at a synchrotron is always a matter of team work. Many people are needed to set up the chamber, operate the beamline, prepare the samples, and carry out the measurements. I especially want to thank: *Dr. Radu Abrudan, Dr. Carolin Antoniak, Dietger Bovenschen, Philipp Eckhold, Alexander Krüger, Bernhard Krumme, Julia Kurde, Dr. Ponpandian Nagamony, Dr. Cristina Navío, Dr. Jun Luo, Prof. Dr. Pankaj Srivastava, Dr. Claudia Weis, Dr. Xiaoying Xu*.

For technical support during the beamtimes at BESSY II, I want to thank *Dr. Willy Mahler*, *Helmut Pfau*, *Dr. Friedmar Senf*, and *Birgitt Zada*.

Dr. Carsten Tieg, for his assistance during the XMCD measurements at ESRF. *Adrian D. Ward Cherrier*, for his full support during the STM measurements at ESRF.

I thank the whole AG Kuch for the excellent atmosphere.

Furthermore, I would like to thank:

Dr. Kilian Lenz, for answers on many difficult questions.

Prof. Dr. Olle Eriksson, *Prof. Dr. Peter Oppeneer*, and the theoretical physicists from the group at Uppsala University (Sweden), for the fruitful collaboration.

Dr. Marco Haryono and *Katja Student* from the group of *Prof. Dr. Andreas Grohmann*, for synthesizing $Fe(bppmc)_2(BF_4)_2$ and $Fe(bp)_2$, respectively.

Prof. Dr. Franz Renz and *Dr. Michael Klein*, for providing $Fe(phen)_2(NCS)_2$ and $Fe(phen)_2(NCSe)_2$.

Uwe Lipowski for all his CAD drawings.

Detlef Müller, he and his team from the mechanical workshop do a fabulous job, realizing complicated designs and finding solutions for various non-standard problems.

Daniel Brete, for many discussions about physics.

Mareike and *Hannes Bernien*, and *Hanno Boller*, for supporting me in various occasions.

My parents *Maria* and *Dr. Jürgen Bernien*, for being always there for me.

Monica, for her support and love.